AD_____

Award Number: W81XWH-04-1-0461

TITLE: Time-Resolved and Spectroscopic Three-Dimensional Optical Breast
Tomography

PRINCIPAL INVESTIGATOR: Swapan K. Gayan

CONTRACTING ORGANIZATION: City College of New York
New York, NY 10031

REPORT DATE: March 2009

TYPE OF REPORT: Final

PREPARED FOR: U.S. Army Medical Research and Materiel Command
Fort Detrick, Maryland 21702-5012

DISTRIBUTION STATEMENT: Approved for Public Release;
Distribution Unlimited

The views, opinions and/or findings contained in this report are those of the author(s) and
should not be construed as an official Department of the Army position, policy or decision
unless so designated by other documentation.

REPORT DOCUMENTATION PAGE

Form Approved
OMB No. 0704-0188

Public reporting burden for this collection of information is estimated to average 1 hour per response, including the time for reviewing instructions, searching existing data sources, gathering and maintaining the data needed, and completing and reviewing this collection of information. Send comments regarding this burden estimate or any other aspect of this collection of information, including suggestions for reducing this burden to Department of Defense, Washington Headquarters Services, Directorate for Information Operations and Reports (0704-0188), 1215 Jefferson Davis Highway, Suite 1204, Arlington, VA 22202-4302. Respondents should be aware that notwithstanding any other provision of law, no person shall be subject to any penalty for failing to comply with a collection of information if it does not display a currently valid OMB control number. **PLEASE DO NOT RETURN YOUR FORM TO THE ABOVE ADDRESS.**

1. REPORT DATE (DD-MM-YYYY) 31-MAR-2009	2. REPORT TYPE Final	3. DATES COVERED (From - To) 01 APR 2004 - 28 FEB 2009

4. TITLE AND SUBTITLE Time-resolved and spectroscopic three-dimensional optical breast tomography	5a. CONTRACT NUMBER W81XWH-04-1-0461
	5b. GRANT NUMBER W81XWH-04-1-0461
	5c. PROGRAM ELEMENT NUMBER

6. AUTHOR(S) Swapan K. Gayen Email: gayen@sci.ccny.cuny.edu	5d. PROJECT NUMBER
	5e. TASK NUMBER
	5f. WORK UNIT NUMBER

7. PERFORMING ORGANIZATION NAME(S) AND ADDRESS(ES) City College of New York 160 Convent Avenue New York, NY 10031	8. PERFORMING ORGANIZATION REPORT NUMBER

9. SPONSORING / MONITORING AGENCY NAME(S) AND ADDRESS(ES) Department of the Army US Army Medical Research and Materiel Command 504 Scott Street Fort Detrick, MD 21702-5012	10. SPONSOR/MONITOR'S ACRONYM(S) USAMRMC
	11. SPONSOR/MONITOR'S REPORT NUMBER(S)

12. DISTRIBUTION / AVAILABILITY STATEMENT

Approved for public release; Distribution unlimited

13. SUPPLEMENTARY NOTES

14. ABSTRACT

The goal of the research project, "Time-Resolved and Spectroscopic Three-Dimensional Optical Breast Tomography," was to develop a safe and affordable breast cancer detection modality that uses noninvasive near-infrared (NIR) light for imaging and diagnosing tumors in human breast with high resolution and specificity. In order to realize that goal three different approaches were developed. These are *Optical Tomography using Independent Component Analysis* (OPTICA), *Round Trip Matrix* (RTM) *approach, and Center of Intensity Time Gated Imaging* (CITGI). OPTICA is the most developed of these approaches. It has been demonstrated that OPTICA can detect, obtain the three-dimensional location information and cross-section images of small absorbing, scattering, and fluorescent targets in model media, and tumor(s) in realistic model breast with considerable accuracy. Further accomplishments include development of a forward model for determining the backscattered polarized light intensity distribution, and initial development of a technique to determine scattering coefficient (μ_s), absorption coefficient (μ_a), and anisotropy factor (g) of breast tissue specimens. Besides detection and localization of tumors in breast, these results may have potential applications in optical biopsy, and lumpectomy. The graduate student supported by the project received his Ph. D., adding another scientist to the ongoing fight against breast cancer.

15. SUBJECT TERMS
Breast cancer, near-infrared imaging, fluorescence imaging, target localization, optical tomography using independent component analysis (OPTICA), polarization sensitive imaging

16. SECURITY CLASSIFICATION OF:			17. LIMITATION OF ABSTRACT	18. NUMBER OF PAGES	19a. NAME OF RESPONSIBLE PERSON R. R. Alfano
a. REPORT Unclassified	b. ABSTRACT Unclassified	c. THIS PAGE Unclassified	Unclassified	93	19b. TELEPHONE NUMBER (include area code) (212) 650-5531

Standard Form 298 (Rev. 8-98)
Prescribed by ANSI Std. Z39.18

Table of Contents

4. INTRODUCTION

The goal of the res earch, "Time-Resolved and S pectroscopic Three-Dimensional Optical Breas t Tomography," was to develop a safe and affordab le breast cancer detecti on modality that uses noninvasive near-infrared (NIR) li ght for im aging and diagnosing tum ors in hum an breast with high resolution and specificity. The project involv ed developing (a) experim ental approach for probing the specim en using NIR li ght and collecting two-dim ensional (2-D) im ages, and (b) image recon struction and target loc alization a lgorithms that m ake use o f the expe rimental data for generating three-dimensional (3-D) tomographic images.

 Considerable progress in both of these areas was m ade during the period of performance of thi s project. The perform ance period, with no-cost extensions, spanned from May 1, 2004 to March 31, 2009. The project had a late start owing to the time it took for the Research P rotocol to be approved (USAMRMC finalized the approval on December 21, 2004).

5. BODY

The tasks performed and the progress made in the project may be broadly grouped as follows:

- Development of experimental arrangements;
- Development of the *optical tomographic imaging using independent component analysis* (OPTICA) method;
- Extension of OPTICA to image and absorptive, scattering, and fluorescent targets within highly scattering turbid media, and obtain cross section images of the target;
- Development of a tomographic image reconstruction approach using the "*round-trip matrix*" (RTM) approach;
- Development of a forward model for *scattered light intensity distribution in the backscattering geometry*;
- Development of an approach for determination of light absorption and scattering characteristics and anisotropy factor of a highly scattering medium using backscattered circular polarized light;
- Detection and localization of *targets in model turbid media*, and tumors in '*realistic model breast*' assembled using *ex vivo* normal and cancerous breast tissues using the formalisms developed in this project;
- Development of a *near-infrared center of intensity time gated imaging* approach; and
- Polarization sensitive imaging.

We provide an overview of our accomplishments in these areas, and refer to previous *annual reports* and *appended publications* for detailed description where applicable. While the publications were presented with the relevant annual reports, we append those in this final report for completeness and ready reference.

5.1. Development of Experimental Arrangements

Three com plementary experim ental arrangem ents were set up and/or adapted [Technical Objective (**TO**) 1, **Task 1**] and performance tested to carry out the project tasks. These include a *time-resolved transillumination imaging arrangement*, a *spectroscopic imaging arrangement*, and a *multi-source illumination and multi-detector signal acquisition arrangement*.

5.1.1. *Time-resolved transillumination imaging arrangement*: The experim ental arrangement for *time-resolved imaging* m ade use of approxim ately 120-fs duration, 1-kHz repetition-rate, 800-nm light pulses form a Ti-sapphire laser and amplifier system for probing the sample, and an ultrafast gated intensified camera system (UGICS) for recording 2-*D* images. The UGICS is a com pact gated im age intensifier unit fiber-optically coupled to a charged-coupled device (CCD) cam era. It p rovides an electronic gate pulse w hose full-width-at-half- maximum duration can be adjusted to a minimum of 80-ps, and the position of the time gate could be varied over a 20 ns range with a step size of 25 ps (or s ome integral multiple of it). The signal recorded by the UGICS at a part icular gate position, t_i is a two-dimensional (2- *D*) im age, that is, a 2 -*D* intensity distribution $I(x, y, t_i)$ formed by the con volution of the transmitted light pulse with the gate pulse centered on the gate position.

5.1.2. NIR spectroscopic imaging arrangement: The *NIR spectroscopic imaging arrangement* used the 1200-1325 nm out put of a m ode-locked Cr $^{4+}$:forsterite laser and regenerative am plifier s ystem to illum inate th e sam ple. A Fourier sp ace gate selected out a fraction of the less scattered im age-bearing photons. A camera lens co llected and directed th ese photons to the sensing element of a 320x240 pixels InGaAs NIR area camera. The resulting 2-*D* images for different wavelengths in the 1225 – 1300 nm range are recorded and displayed on a personal computer, and stored fo r further analysis and processi ng. The arrangem ent was useful for thin *ex vivo* breast tissue sam ples, but for thicker 'realistic b reast models' the arrangement described in Section 5.1.3 below was used.

5.1.3. Multi-source illumination and multi-detector signal acquisition arrangement: The *multi-source illumination and multi-detector signal acquisition arrangement* used both the output of the Ti:sapphire laser system mentioned above, as well as, the continuous wave (CW) 784 nm radiation from a diode laser delivered by a 200- μm optical fiber for sample illumination. Multiple so urce illum ination was realized in p ractice by s tep scann ing the sam ple along the horizontal (*x*) and vertical (*y*) dire ctions ac ross the la ser beam . A cam era lens c ollected the diffusely tra nsmitted light on th e opposite face of the sample and p rojected it on to the sen sing element of a cooled charged couple device (CCD) camera (for steady-state measurements), or the UGICS system discussed above (for tim e-resolved measurements). Each illuminated pixel of the CCD camera (or, the U GICS system) could be rega rded as a detector. For illumination of every scanned point on the input surf ace of the sam ple, th e CCD cam era (or, the UGICS system) records the diffusely transmitted intensity pattern on the output surface.

These experim ental arrangem ents were first presented in A nnual Report 1 covering the period of May1, 2004 through April 30, 2006. The publications detail the experim ental arrangements and pres ent values of different experim ental param eters pertaining to the spec ific sample(s) under investigation.

5.2. Optical Tomographic Imaging using Independent Component Analysis (OPTICA)

A crowning accom plishment of the project is the development of a novel target detection an d localization approach,called OPTICA[1-2] that enables 3-D localization of target(s) em bedded in a highly scattering turbid m edium with high level of accuracy [**TO 3, Task 1, Task 2; TO 4, Tasks 6-8**]. The approac h makes use of transmitted li ght signal collected by m ultiple detec tors following multiple-source illumination of the turbid medium containing the targe ts, as outlined in the experim ental arrangement of Section 5.1.3. The resulting m ultiple angular views provide robust data that is analyzed usin g the independent com ponent analysis[3] (ICA) of inf ormation

theory to determine the locations of targets relative to the medium boundaries with millimeter accuracy.

In a series of coordinated analytical, numerical, and experimental efforts we have developed OPTICA, tested it on targets embedded in model media, tumors inside model breast assembled using *ex vivo* human breast tissues, and extended it to absorptive, scattering, and fluorescent targets. The milestones in the development and efficacy testing process of OPTICA are highlighted as:

- First, we developed the theoretical formalism for OPTICA and tested it using simulated data (**TO 3, Task 6**). The accomplishments were reported in Annual Report 1 for this project,[4] and detailed in Reference 1, which appears as *Appendix 1* in this Final Report. The study using simulated data demonstrated the potential of OPTICA to provide three-dimensional (3-*D*) position information with high accuracy.

- Second, the efficacy of the OPTICA approach was tested when it was to obtain the 3-D locations of 4 small targets in the breast phantom obtained from Professor Hebden's Group at University College London (UCL),[5] [**TO1, Task 1; TO3, Task 6 and Task 7**]. The properties of this sample are detailed in Reference 5. It simulates the average optical properties of a human breast, and the 4 tumor-simulating targets differ from the background in their optical scattering coefficients. The OPTICA formalism was able to locate all 4 targets including the weakest one having a scattering coefficient of only 1.1 times that of the intervening media (and was considered to be "rather unlikely to be found"[5] within mm accuracy. The results were published[2], reported in Annual Report 1, and appear as *Appendix 2* of this final report.

- Third, the performance of OPTICA approach was tested on absorptive and fluorescent targets embedded in model media of Intralipid10% suspension in water (concentration adjusted to mimic the average scattering coefficient, absorption coefficient, and anisotropy factor of human breast tissue, and thickness chosen such that the ratio of thickness to the transport mean free path (50:1) for the sample resemble that of average female human breast when compressed for taking mammograms) [**TO3, Task 6 and Task 7**]. The results were presented in Annual Report 1, and the relevant publications[6,7] are appended in this Final Report (*Appendix 3*, and *Appendix 4*).

- Fourth, the OPTICA formalism was further extended[8] to provide cross sectional image of the target(s), in addition to the 3-*D* location information. In this extension of OPTICA, the size and shape of the *j*-th target within the sample is estimated from a back-projection of the signal due to the target from the detection plane onto the target plane. Independent component analysis (ICA) provides an estimate of the contribution $U_{mj}(\mathbf{r}_d, \mathbf{r}_j, \omega)$ of the *j*-th target to the overall signal $U_m(\mathbf{r}_d, \mathbf{r}_j, \omega)$ due to all the targets, where $\mathbf{r}_d$ and $\mathbf{r}_j$, are the positions of the detector plane and the *j*-th target respectively. The mathematical formalism for obtaining the cross sectional image is summarized in Eq. (4) and Eq. (5) of Reference 8 (*Appendix 5*), which also provides examples of the application of the formalism to realistic breast model **[TO 4, Task 9].** The extension of the formalism to generate size and shape information provides inverse image reconstruction ability (*TO 3*) and its application to targets inside realistic human breast models (*TO4, Task 9*) is a crucial step towards *in vivo* breast imaging. These results were presented in the Annual Report 2 [Reference 9].

- OPTICA also provides a cross-s ectional image of the target within the turbid m edium. OPTICA may be used for detection, locali zation and i maging of absorptive, scattering and fluorescent targets. The details of the a pproach were published and are a ttached to this document as *Appendices* 1,2,4,5.

- As detailed in a Section 5.6, OPTICA was used to detect and locate tum ors in realistic breast models.

5.3. Optical Tomography using 'round-trip matrix' (RTM)

We developed a new num erical algorithm [**TO 3, Task 6**] called RTM for obtaining tomographic im ages of targe ts in tu rbid m edium, and tested it using sim ulated data.[4,10] In th is approach, the transport of light from multiple s ources th rough the turb id m edium to an array of detectors is represented by a res ponse matrix that can be construc ted from experim ental data. T he 'round-trip m atrix' is constructe d b y m ultiplying the respo nse m atrix by its tran spose for CW (adjoint m atrix f or f requency-modulated and short-pu lse) illum ination. The RTM provide s a mathematical description of transport of light from the sources through th e turbid m edium with embedded objects to the array of detectors and back, and is similar to the time-reversal matrix used in the general area of array processing for acoustic and radar imaging. The vector subspace method along with Green's function calculated from an appropriate forward model is then used to detect the targets. In test runs using simulated data,[10] the approach was able to locate 6 targets at different locations within a turb id medium of thickne ss $50 l_t$ (l_t = trans port mean free path of the m edium). The work was published[10], reported in the First Annual Report [Reference 4], and appended in this final report as *Appendix* 6). While the simulated data used slab geometry, the approach can be used for other sample geometries and to different forward models.

5.4. Development of a forward model for scattered light intensity distribution in the backscattering geometry

While the approaches mentioned in Section 5.2 and S ection 5.3 use experim ental data in transillumination geometry, an approach based on backscattering geometry will be advantageous for targets closer to the input plane, and for obtaining depth location. We developed an analytical cumulant solution of both the tim e-dependent scalar radiative transfer equation (SRTE), and the vector radiative transfer equation (VR TE) in an inf inite u niform m edium.[11,12] The solution o f SRTE is suitable for describing scattered photon density distribution for an arbitrary phase function as long as it is a function of the scat tering angle. The num erical results of light propagation from the analytical solution are in a good agreem ent with that of M onte Carlo simulation.[13]

However, the SRTE cannot account for the polari zation of the inciden t and scattered light beams. Polariza tion is a n im portant param eter a nd its evolution as a polarized beam of light interacts with a sca ttering m edium with e mbedded targets can provide useful im aging information. To capitalize on the advantages that pol arization has to offer, we used the analytical solution of the VRTE t o study the backscattering of circularly polarized light pulses from an infinite uniform scattering m edium as a function of the helicity of the incident light and size of scatterers in the medium **[TO3, Task 6]**. The formalism considers a polarized short pulse of light incident on the scattering m edium, uses the anal ytical cum ulant so lution of the VRTE with the phase m atrix obtained f rom the Mie theory to calcula te the tem poral prof ile of scatte red polarized p hotons for any position and any angle of detection. The details of the for malism,

results, and comparison with experimental results were published[14], presented in Annual Report 2 [Reference 9], and appended as *Appendix 7*.

The results show that circu larly polarized light of the sam e helicity dom inates the backscattered signal wh en scatterer size is la rger than th e wavelength of light. For the sm aller particle size, light of opposite helicity m akes the dom inant contribution to th e backscattered signal, as shown in Figure 1 in *Appendix 7*. The conclusion is in good agreem ent with experimental results, as displayed in Fig. 6 of *Appendix 7*. The characteris tic change of circular polarization of backscattering light with size of scatterers may provide a new m ethod to directly determine m icroscopic size of scatterers, which m ay be useful f or h ighlighting tum ors f rom normal tissues.

5.5. Determination of light absorption, scattering characteristics and anisotropy factor

We are developing a technique to determine scattering coefficient (μ_s), absorption coefficient (μ_a), and anisotropy factor (g) of breast tissue specim ens usi ng backscattering of light of different wavelengths **[TO 2, Task 4]**. The approach involves illumination of the surface of the specimen with circularly polarized light at an oblique angle of incidence ($\sim 70^0$) and measurement of the backscattered co -polarized and cross-po larized light. From the backscattered diffuse reflectance data the abs orption coeff icient (μ_a), and the reduced scattering coefficient ($\mu_s^{'}$) are determined at different wavelengths. The wave length dependence of the reduced scattering coefficient, $\mu_s^{'}$ is used to extract th e fractal dim ension (D_f) of the specim en. The depolarized diffuse reflection data and these three param eters are then used to extract the anisotropy factor (g). The g-factor provides a u seful probe of the size of the scatterers and serves as a fingerp rint for discrim inating between norm al and cancerous tissues. The approach m ay prove useful in lumpectomy, where the surgeon looks for the margins of the tumor with high accuracy.

Details of the experimental method and approach to extract key parameters are presented[15] in *Appendix 8*, and were reported in Annual Report 2. [Reference 9]

5.6. Detection, localization, and cross section imaging of tumors in model cancerous breast using OPTICA

A m ajor thrust of the project was to carry out m easurements on *ex vivo* breast tissue specimens, and on m odel breasts formed using norm al and cancerous *ex vivo* breast tissues **[TO 1, Task 2; TO 2, Task 4; and TO 4, Task 9]**. The results of tim e-resolved experiments using experimental arrangem ent described in Sec tion 5.1.1, and spectroscopic m easurements using experimental arrangement described in S ection 5.1.2 on thin (thickness 5 mm – 10 mm) *ex vivo* human breast tissues further confirm ed our earlie r observ ations that (a) im ages recorded with earlier arriving light highlight cancerous ti ssues, whi le t hose r ecorded w ith later arriving light highlight normal tissues; (b) spec troscopic measurements using light nea r-resonant with adipose absorption around 1207 nm can distinguish adipose tissues from fibro-glandular tissues.[16]

Particular emphasis was placed on testing the efficacy of the OPTICA formalism to detect, locate, and im age a tumor inside a cancerous breast. The results were presented in Annual Report 2,[9] and Annual Report 3,[17] and published elsewhere.[18,19] We will provide a brief overview of a measurem ent on a realisti c can cerous breas t m odel and leave the details to an appended reprint (*Appendix 9*). The model breast was a 70 mm X 55 mm X 33 mm slab composed of tw o pieces of *ex vivo* human breast tissues provided to us by National Disease Research Interch ange

under an Internal Review Board approval at the City College of New York. The larger piece was normal tissue that included mainly adipose tissue and streaks of fibro-glandular tissues. The existence of the fibro-glandular tissues was not known prior to making the measurements. The second piece was mainly a tumor (infiltrating ductal carcinoma) with a small amount of normal tissues in the margins with an overall approximate dimension of 8 mm X 5 mm X 3 mm. An incision was made in the mid-plane (along the *z*-axis, which was the shorter dimension of the tissue) of the normal piece and some amount of normal tissue was removed from the central region making a small pouch. The tumor piece was then inserted into the pouch and the incision was closed by moderate compression of the composite consisting of the normal tissue and the tumor along *x-y-z* directions. The breast tissue slab was contained inside a transparent plastic box. One of the sides of the box could be moved to uniformly compress the tissue along the *z*-axis and hold it in position. The resulting specimen, a 70 mm X 55 mm X 33 mm slab, was treated as one entity in the subsequent imaging experiment. The position of the tumor within the slab was known since it was placed in position as discussed above. One of the tests of the efficacy of this imaging approach was to see how well the known position is assessed.

The experimental arrangement (described in Section 5.1.3 and shown schematically in Fig. 1(a) of *Appendix 9*) used a 200-μm optical fiber to deliver a 784-nm, 300 mW continuous-wave beam from a diode laser for sample illumination. The beam was collimated to a 1-mm spot onto the entrance face (the 'source plane') of the slab sample. Multiple source illumination was realized in practice by step scanning the slab sample across the laser beam in a 22X16 *x-y* array of grid points with a step size of 2.0 mm using a computer controlled translation stage. The signal from the opposite face of the sample (the 'detection plane') was collected by a camera lens and projected onto the sensing element of a cooled 16-bit, 1024 X 1024-pixel charged couple device (CCD) camera. Although the scanned area is 42 mm X 30 mm on the source plane, the imaged area of the detection plane was much larger, covering the entire 70 mm X 55 mm area of the model breast. Each illuminated pixel of the CCD camera could be regarded as a detector.

For illumination of each scanned point, the CCD camera recorded an image. A typical raw image is shown in Fig. 1(c) of *Appendix 9*. Each raw image was then cropped to select out the information-rich region, and binned to enhance the signal-to-noise ratio. All the binned images corresponding to illumination of the grid points in sequence were then stacked, and used as input for independent component analysis. After optical measurements, the sample was transferred to our collaborators at the New York Eye and Ear Infirmary for pathological study and correlation **[TO2, Task 5]**.

The key results of the experiment are as follows.

(a) OPTICA identified three different structures (Fig. 2, *Appendix 9*) as three independent components based on the differences in optical properties. These include the tumor whose presence and position was known from the sample preparation process. We ascribed the other two structures to fibro-glandular tissues, as the normal component of the breast tissue specimen was mainly adipose tissue. Comparison with the pathology results further confirmed the identity of the tumor and the fibro-glandular tissues.

(b) The location of the tumor was determined to within ~1 mm in all three dimensions. The locations of the fibro-glandular tissues were also estimated. The locations of the components are given in Table I of *Appendix 9*.

(c) The FWHM of the tum or is estim ated to be ~ 10.3 mm and 7.4 mm   along the x and y directions, respectively (details in Fig. 3, *Appendix 9*).

These results demonstrate that OPTICA is suited for *in vivo* study using volunteers.

5.7. Development of near-infrared center of intensity time gated imaging approach

A major thrust of the project was to develop opti cal imaging approaches that are simple and easy to im plement **[TO3, TO4]**. W e explored the   development of a new   near-infrared optical imaging approach for locating a target em bedded in a turbid medium. The approach is based on the prem ise that a targe t (that is, an optica l inhomogeneity) within the tu rbid medium alters th e propagation of light through the medium   . Conse quently, the spatial distribution of the output light intensity (SDOLI) is different with an embe   dded target than that without it. The target localization is based on   an analysis of the spatial va riation of the tran smitted ligh t inten sity distribution for illum ination at different pos itions on the sample boundary. The b asic principle, experimental arrangement, and preliminary results are presented in *Appendix 10* ("*Detection of a target in a highly scattering turbid medium using near-infrared center of intensity time gated imaging*"), in the form of a manuscript to be submitted for publication.

The   experimental   arrangement   for   realizing the ap proach in p ractice is sim ilar to tha t described in Section 5.1.3, and shown in Fig. 2 of   *Appendix 10*. The s cattering medium was a suspension of Intra lipid-10% in wa ter, with an estim ated reduced scattering coefficient, $\mu_s'\sim$ 1.168 mm^{-1} (transport length 0.86 mm) and an absorption coefficient of 0.0021 mm^{-1} at 800 nm. The Intralipid-10% suspension was held in   a 240 mm x 160 mm x 65   mm rectangular glass container. The target was a 10 mm x 10 mm x 3 mm neutral density filter (absorption coefficient 0.23 mm^{-1} at 800 nm). Another sample was a   5   mm x 5 mm x 5 mm piece of porcine liver (target) placed inside a 150 mm   x 90 mm x 50 mm slab of porcine tissue held in a rectangular plastic cell.

The samples were illuminated by 800 nm, 200 ps, 1 kHz repetition rate pulses from   a Ti:sapphire laser and re generative amplifier system. The average beam power was 150 mW and the beam spot size was approxim ately 2 mm. The laser beam was incident along the z-axis into one of the 2 40 mm x 160 mm flat f aces of the container. Th e 2-*D* intensity distribution of light emergent from the opp osite end f ace of the c ell was reco rded by an u ltrafast ga ted inten sified camera system (UGICS). The UGICS provides an electronic time gate whos e full width at half maximum (FWHM) duration can be set as short as 80 ps. The gate position could be varied over a 20 ns range with a m inimum step size of 25 ps . The sa mple cell was mounted on a translation stage for lateral scanning. The input beam and the UGICS were not scanned.

The approach was able to detect the target   in both the cases. As shown in Fig. 5 of *Appendix 10,* the approach provided a two-dim ensional im age of the porcine liv er em bedded within the porcine tissue.
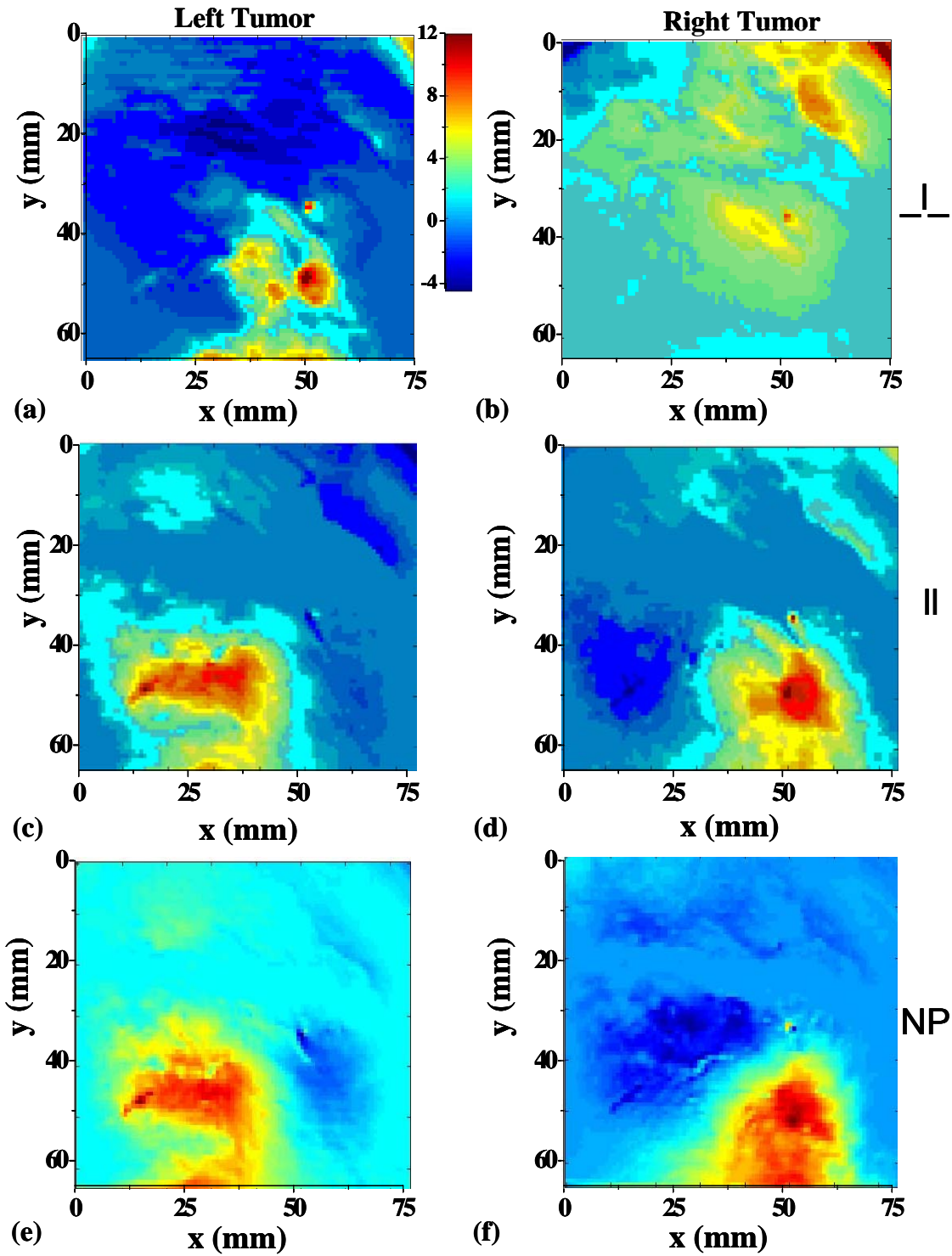
5.8. Polarization-gated Imaging

The use of polarization-gated im aging provides better im age resolution and contrast in direct imaging for optica lly th in sam ples.[20,21] W e wanted to explo re if any addition al adv antages a re observed if polarization gated im aging is used along with OPTI CA to obtain the location and cross section images of tumors in a model breas t. The work was an approved extension of TO 4, and was carried out instead of TO5.

The m odel breast was sim ilar to that desc ribed in Section 5.6, and the experim ental arrangement described there was modified to enable polarization-gated imaging. The sample was illuminated with 800-nm circularly polarized light. Transillumination images were recorded with light having the same helicity as the incident light, and with light orthogonal to the incident light. The OPTICA for malism described earlier was used to obtain targe t lo cation, and cross section images. The results were com pared with that ob tained us ing linear ly polarized ligh t for sample illumination, and record ing of im ages with the total transm itted light without any p olarization discrimination.

The OPTICA generated im ages are shown in Fi g. 1 in the following page. Fig. 1(a) and Fig 1(b) show the OPTICA generate d cross sectio n im ages of the lef t tu mor piece a nd the righ t tumor piece, respec tively, when the trans illumination im aging m easurements were carried out using light orthogonal to the incide nt circularly polarized light. As can be seen from the figures, the c ross se ction im ages are not well d eveloped. Fig. 1(c) and Fig. 1(d) show the OPTICA generated cross section im ages of t he left tu mor piece and the righ t tu mor piece, respectively , when the tr ansillumination imaging measurements were c arried out using light of same helicity as the incident circularly polarized light. Fig. 1(e) and Fig 1(f) are corresponding cross section images when linearly polarized light is used for target illumination and images are recorded with total transmitted ligh t without any p olarization discrim ination. Th e positions of th e two targets obtained from Fig. 1(c) and Fig. 1(d), and Fig. 1(e) and Fig. 1(f) are identical. However, Fig. 1(c) and Fig. 1(d) appear to be m ore com pact than Fig. 1(e) and Fig. 1(f). It m ay represent an advantage of polarization-sensi tive im aging, or m ay be a cons equence of lower light level recorded when polarization d iscrimination is applied. More work will be need ed to clarify if polarization-gated imaging offers any substantial advantage when imaging through thick tissues.

Polarization-sensitive Imaging

Left Tumor

Right Tumor

(a) **(b)** **(c)** **(d)** **(e)** **(f)**

Fig. 1 Polarization gated OPTICA imaging of tumors in a model breast described in the text.

6. KEY RESEARCH ACCOMPLISHMENTS

The key research accomplishments are expounded below.

- Developed three different approaches for det ection and imaging of targets in a tu rbid medium, such as, tum ors in the breast. These are *Optical Tomography using Independent Component Analysis* (OPTICA), *Round Trip Matrix* (RTM) *approach, and Center of Intensity Time Gated Imaging* (C ITGI). OPTICA is the m ost developed of these approaches.

- Demonstrated the efficacy of OPTICA in detecting, locating, and cross section im aging of scattering, absorptive, and fluorescent targets in turbid media. Key results include:

    (i)   Detection and localization of 4 sm all scattering targets in a breast phantom (UCL sample, Reference 5), the weakest one ha ving a scattering coefficient of only 1.1 times that o f the in tervening media (and was considered to be "r ather unlikely to be found"[5] within mm accuracy (detailed in *Appendix 2*);

    (ii) Detection of two absorptive targets in a breast tissue-simulating model medium of thickness 50 times the transport mean free path (l_t) (detailed in *Appendix 4*);

    (iii) Detection o f a 4- mm diam eter fluores cent sphe re in a br east tissue- simulating model medium of thickness 50 tim es the tr ansport mean free path (l_t) (detailed in *Appendix 4*).

    (iv) Detection, localization and cross section imaging of small tumors in model breasts assembled using *ex vivo* breast tis sues with m illimeter accu racy. (*Appendix 9, Appendix 5*)

    (v)   Detection, 3-D localization, and cross sect ion im aging of a fluorescent target in breast tissue specimens and model medium. (*Appendix 8*).

- Developed a forward model for determ ining th e backs cattered pola rized ligh t intens ity distribution (*Appendix 7*).

- Developed a technique to determ ine scattering coefficient (μ_s), abso rption coefficient (μ_a), and anisotropy factor (g) of breas t tissue specim ens that h as potential applic ation in optic al biopsy, that is, for determining if the tissue specimen is normal or cancerous (*Appendix 4*).

7. REPORTABLE OUTCOMES

7.1. Journal Articles

1. M. Xu, M. Alrubaiee, S. K. Gayen and R. R. Alfano, "Three-dimensional optical imaging of objects in a turbid m edium using inde pendent com ponent analys is: theo ry a nd simulation," *J. Biomed. Opt.* **10**, 051705 (2005).

2. M. Alrubaiee, M. Xu, S. K. Gayen, M. Brito, and R. R. Alfa no, "Three-dim ensional optical tom ographic im aging of objects in tissue-simulating turbid m edium using independent component analysis," *Appl. Phys. Lett.* **87**, 191112 (2005).

3. M. Alrubaiee, M. Xu, S. K. Gayen, and R. R. Alfano, "Three-dim ensional localization and cross section reconstructi on of fluorescent targets in *ex vivo* breast tissue using independent component analysis," *Appl. Phys. Lett.* **89**, 133902 (2006).

4. W. Cai, Xiaohui Ni, S. K. Gayen, and R. R. Alfano, "Analytical cumulant solution of the vector radiative transfer equati on investigates backscattering of circularly polarized light from turbid media," *Phys. Rev. E* **74**, 056605 (2006).

5. M. Xu, M. Alrubaiee, S . K. Gayen and R. R. Alfano, "Optical diffuse im aging of a n *ex vivo* m odel cancerous hum an breast using independent component analysis," *IEEE J. Select. Topics Quantum Electron.* **14**, 43 (2008).

7.2. Conference Proceedings Articles and Book Chapters

6. W. Cai, M. Alrubaiee, S. K. Gayen, M. Xu, and R. R. Alfano, "Three-dimensional optical tomography of objects in turbid m edia usi ng the 'round-trip m atrix," in Optical Tomography and Spectroscopy of Tissue VI, edited by Britton Chance, Robert R. Alfano, Bruce J. Tromberg, Mamoru Ta mura, Eva M. Sevick-Muraca, Proceedings of SPIE, Vol. 5693 (SPIE, Bellingham, WA, 2005), pp. 4-9.

7. M. Alrubaiee, M. Xu, S. K. Gayen, and R. R. Alfano, "Fluorescence optical tomography using independent component analysis to detect small objects in turbid media," in Optical Tomography and Spectroscopy of Tissue VI, edited by Britton Chance, Robert R. Alfano, Bruce J. Tromberg, Mamoru Tam ura, Eva M. Sevick-Muraca, Proceedings of SPIE Vol. 5693 (SPIE, Bellingham, WA, 2005), pp. 221-224.

8. M. Xu, M. Alrubaiee, S. K. Gayen, and R. R. Alfano, "Optical tomography using independent com ponent analysis to detect absorptive, scattering, or fluorescent inhomogeneities in turbid media," in *Optical Tomography and Spectroscopy of Tissue VI,* edited by B ritton Chance, Robert R. Alfano, Bruce J. T romberg, Mamoru Tam ura, Eva M. Sevick-Muraca, Proceedings of SPIE Vol. 5693 (SPIE, Bellingham , WA, 2005), pp. 528 – 535.

9. M. Xu, M. Alrubaiee, S. K. Gaye n, and R. R. Alfano, " Optical high resolution cross section imaging of a hum an breast model usin g independent com ponent analysis in CW and time domain." *Proceedings of SPIE,* Vol.6434, 643416 (2007).

10. M. Xu, M. Alrubaiee, S. K. Gayen, and R. R. Alfano, "Determination of light absorption, scattering and anisotropy factor of a highl y scattering m edium using backscattered circular polarized light." *Proceedings of SPIE* Vol. 6435, 64350J (2007).

7.3. Presentations

1. M. Xu, M. Alrubaiee, W. Cai, S. K. Ga yen, and R. R. Al fano, "Toward optical im aging of s mall tumors in breasts using cum ulant forward m odel and Independent Com ponent Analysis," Paper P14-19 pres ented at the Era of Hope, De partment of Defense Breast Cancer Research Program Meeting, June 8-11, 2005, Philadelphia, PA.

2. M. Alrubaiee, M. Xu, S. K. Gayen, and R. R. Alfano, "Optical tomography using Independent Component Analysis for breast can cer detection," Paper P 64-2 presented at the Era of Hope, Departm ent of De fense Breast Cancer Research Program Meeting, June 8-11, 2005, Philadelphia, PA.

3. M. Alrubaiee, M. Xu, S. K. Gayen, and R. R. Alfano, "Three-dimensional localization of scattering targets in turbid media using Independent Component Analysis," Paper CThJ3 presented at the Conference on Lasers a nd Electro-Optics (CLEO), May 22-27, 2005, Baltimore, Maryland.

4. M. Xu, M. Alrubaiee, S. K. Gayen, and R. R. Alfano, "Fluorescence optical im aging in turbid m edia using Independent C omponent Analysis," Paper CFJ1 pres ented at th e Conference on Lasers and Electro-Op tics (CLEO), May 22-27, 2005, Baltimore, Maryland.

5. W. Cai, M. Alrubaiee, S. K. Gayen, M. Xu, and R. R. Alfano, "Three-dimensional optical tomography of objects in turbid media using the 'round-trip m atrix." Paper 5693-02 presented at the Optical Tom ography and Spectroscopy of Tissue VII Conference of SPIE's BiOS 2005/ Photonics West, January 22-27, 2005, San Jose, California.

6. M. Alrubaiee, M. Xu, S. K. Gayen, and R. R. Alfano, "Fluorescence optical tom ography using independent component analysis to detect sm all objects in turbid m edia." Paper 5693-39 presented at the Optical Tom ography and Spectroscopy of Tissue VII Conference of SPIE's BiOS 2005/ Photoni cs W est, January 22-27, 2005, San Jose, California.

6. M. Xu, M. Alrubaiee, S. K. Gayen, and R. R. Alfano, "Optical tomography using independent com ponent analysis to detect absorptive, scattering, or fluorescent inhomogeneities in turbid m edia." Paper 5693-02 presented at the Optical Tom ography and Spectroscopy of Tissue VII Conference of SPIE's BiOS 2005/ Photonics West, January 22-27, 2005, San Jose, California.

7. M. Xu, M. Alrubaiee, S. K. Gayen and R. R. Alfano, "Optical high resolution cross section im aging of human breast using indepe ndent com ponent analys is." Presented at the 5th *Inter-Institute Workshop on Optical Diagnostic Imaging from Bench to Bedside at the National Institutes of Health*, 25-27 September 2006, Bethesda, Maryland, USA**.**

8. M. Xu, M. Alrubaiee, S. K. Gaye n, and R. R. Alfano, " Optical high resolution cross section imaging of a hum an breast model usin g independent com ponent analysis in CW and tim e domain." Paper 6934-42 presente d at Conference 6934: Optical Tom ography and Spectroscopy of Ti ssue VII of SPIE's Bi OS 2007/ Photonics W est, January 20-25, 2007, San Jose, California.

10. M. Xu, M. Alrubaiee, S. K. Gayen, and R. R. Alfano, "Determ ination of light absorption, scattering and anisotropy factor of a highl y scattering m edium using backscattered circular polarized light." Paper 6935-18 presented at Conference 6435: Optical Interactions with Tissue and Cells X VIII of SPIE's BiOS 2007/ Photon ics West, January 20-25, 2007, San Jose, California.

11. M. Alrubaiee, S. K. Gayen, and R. R. Alfano, "Near-infrared tim e-resolved and spectroscopic imaging for breast cancer detection." Poster P42-17 presented at the *Era of Hope*, Departm ent of Defense Breast Cancer Research Program Meeting, June 25-28, 2008, Baltimore, Maryland. Abstract appears in p. 293 of Meeting Proceedings.

12. M. Xu, M. Alrubaiee, S. K. Ga yen, and R. R. Alfano, "Optical tom ography using independent component analysis." Poster P42-17 presented at the *Era of Hope*, Department of Defense Breast Cancer Research Progr am Meeting, June 25-28, 2008, Baltim ore, Maryland. Abstract appears in p. 292 of Meeting Proceedings.

7.4. Degrees Obtained

M. Alrubaiee, the graduate student whose research was supported in part by this grant, successfully defended his Ph. D. thesis entitled, "*Time-resolved and Continuous Wave Spectroscopic Imaging of Biological Media*."

7.5. Personnel Supported

Senior Researchers

Robert R. Alfano: As the Principal Investigator (PI) of the project, Robert R. Alfano, Distinguished Professor of Science and Engineering at the City College of New York, was involved in the overall supervision of the research that was carried out, and received partial summer salary from the project. He has been awarded the most presitious OSA Charles Townes Award in 2008.

Wei Cai: As a research associate Dr. Cai was involved in developing numerical algorithm for image reconstruction, and received partial support for his efforts.

Swapan K. Gayen: Served as the Co-PI for the project, and was responsible for directing the experimental effort, coordinating with the theoretical group, and writing manuscripts based on research results for publication. He received partial summer salary from the project. He started as an Associate Professor and was promoted to Professor during the period covered by the project.

Xiaohui Ni: Dr. Xiaohui Ni carried out polarization dependent imaging measurements as a postdoctoral research associate in the final segment of the project, and received partial support for his efforts.

Yimin Wang: Dr. Yimin Wang worked as a postdoctoral research associate for a year on the project, and pursued the development of near-infrared center of intensity time gated imaging approach. He moved onto become a research faculty at the Beckman Laser Institute at University of California, Irvine.

Min Xu: Dr. Min Xu pursued the development of the optical imaging using the independent component analysis approach as a postdoctoral research associate. He was supported in part by the project, and later took up a position as an Assistant Professor of Physics at Fairfield University, CT.

Students
Mohammad Alrubaiee: Mohammad Alrubaiee pursued his graduate research with support from this project and received his Ph. D in 2007. He is continuing his postdoctoral research in the group.

Rozo Oscar: Rozo Oscar was a graduate student on the project and received partial support.

Zhing Zhang: Zhing Zhang was a graduate student on the project and received partial support.

Technicians
Yuri Budansky: Yuri Budansky is a research technician who provided technical support in assembling experimental arrangements, and received partial support for his efforts.

Roman Zeylikovich: Roman Zeylikovich was involved in developing computer programs for computer automation of some experimental arrangements, and received partial support for his efforts.

Adminstration

Lauren Gohara: Lauren Gohara provided adm   inistrative support, such as, book keeping, preparing payroll, placing orders for equi   pment and supplies and m   aking paym ents to vendors, and received partial support for her efforts.

8. CONCLUSION

The work carried out in the project demonstrates the potential for detection and three-dimensional localization of targets (including tumor) within a turbid medium (including a model breast formed with *ex vivo* tissues) with significant accuracy based on the differences in the scattering, absorption, and fluorescence characteristics of the target (*e.g.,* tumor) and the intervening medium (*e.g.,* normal breast tissue).

"*So What Section*"

- A recent study involving 35,319 patients underscores the influence of primary tumor location on breast cancer prognosis, and makes it imperative that breast cancer detection modalities obtain three dimensional (3-D) location of the tumor relative to the axilla.[22] The current work is an important development in obtaining noninvasive 3-D location of a tumor within the breast.

- The applicability of OPTICA for scattering, absorptive, and fluorescent targets makes it versatile since all three phenomena may be used for contrast enhancement between the tumor and normal breast tissues. Fluorescence-based detection may require use of contrast agents, such as, molecular beacons. Use of far-red and NIR native fluorescence wing[23] is also a possibility.

- Three-dimensional target localization will enable closer probing of a smaller volume around of the target providing more details since smaller pixel size could be used without increasing the computation time (as a smaller volume will be probed).

- Further development of the OPTICA approach may find another important application in lumpectomy, where the surgeon looks for the margins of the tumor with high accuracy.

9. REFERENCES

1. M. Xu, M. Alrubaiee, S. K. Gayen and R. R. Alfano, "Three-dimensional optical imaging of objects in a turbid m edium using inde pendent com ponent analys is: theo ry a nd simulation," *J. Biomed. Opt.* **10**, 051705 (2005).

2. M. Alrubaiee, M. Xu, S. K. Gayen, M. Brito, and R. R. Alfa no, "Three-dim ensional optical tom ographic im aging of objects in tissue-simulating turbid m edium using independent component analysis," *Appl. Phys. Lett.* **87**, 191112 (2005).

3. P. Comon, "Independent component analysis – a new concept? " *Signal Process.* **36**, 287 (1994).

4. Annual Report 1 for this project.

5. D. J. Hall, J. C. Hebden, and D . T. De ply, "Im aging very low contrast objects in breastlike scattering m edia w ith a tim e-resolved m ethod," *Appl. Opt.* **36**, 7270 – 7276 (1997).

6. M. Alrubaiee, M. Xu, S. K. Gayen, and R. R. Alfano, "Fluorescence optical tom ography using independent component analysis to detect small objects in turbid media," in Optical Tomography and Spectroscopy of Tissue VI, edited by Britton Chance, Robert R. Alfano, Bruce J. Tromberg, Mamoru Tam ura, Eva M. Sevick-Muraca, Proceedings of SPIE Vol. 5693 (SPIE, Bellingham, WA, 2005), pp. 221-224.

7. M. Xu, M. Alrubaiee, S. K. Gayen, and R. R. Alfano, "Optical tomography using independent com ponent analysis to detect absorptive, scattering, or fluorescent inhomogeneities in turbid media," in *Optical Tomography and Spectroscopy of Tissue VI*, edited by B ritton Chance, Robert R. Alfano, Bruce J. T romberg, Mamoru Tam ura, Eva M. Sevick-Muraca, *Proceedings of SPIE* Vol. 5693 (SPIE, Bellingh am, WA, 2005), pp. 528 – 535.

8. M. Alrubaiee, M. Xu, S. K. Gayen, and R. R. Alfano, "Three-dim ensional localization and cross section reconstructi on of fluorescent targets in *ex vivo* breast tissue using independent component analysis," *Appl. Phys. Lett.* **89**, 133902 (2006).

9. Annual Report 2 for this project.

10. W. Cai, M. Alrubaiee, S. K. Gayen, M. Xu, and R. R. Alfano, "Three-dimensional optical tomography of objects in turbid m edia usi ng the 'round-trip m atrix," in Optical Tomography and Spectroscopy of Tissue VI, edited by Britton Chance, Robert R. Alfano, Bruce J. Tromberg, Mamoru Ta mura, Eva M. Sevick-Muraca, Proceedings of SPIE, Vol. 5693 (SPIE, Bellingham, WA, 2005), pp. 4-9.

11. W. Cai, M. Lax, R. R. Alfano, "Analytical solution of the elastic B oltzmann transport equation in an infinite uniform medium using cumulant expansion" *J. Phys. Chem. B* **104** 3996-4000 (2000).

12. W. Cai, M. Lax, R. R. Alfano, "Analyti cal solution of the polarized photon transport equation in an inf inite unif orm m edium using cum ulant expansion" *Phys. Rev. E* **63**, 016606 (2001).

13. W. Cai, M. Xu, R. R. Alfa no, "Analytical form of the part icle distribution based on the cumulant solution of the elastic Boltzmann transport equation" Phys. Rev. E **71** 041202 (2005).

14. W. Cai, Xiaohui Ni, S. K. Gayen, and R. R. Alfano, "Analytical cumulant solution of the vector radiative transfer equati on investigates backscattering of circularly polarized light from turbid media," *Phys. Rev. E* **74**, 056605 (2006).

15. M. Xu, M. Alrubaiee, S. K. Gayen, and R. R. Alfano, "Determination of light absorption, scattering and anisotropy factor of a highl y scattering m edium using backscattered circular polarized light." *Proceedings of SPIE* Vol. 6435, 64350J (2007).

16. M. Alrubaiee, S. K. Gayen, R. R. Alfano, and J. A. K outcher, "S pectral and tem poral near-infrared i maging of *ex vivo* cancerous and norm al human breast tissues," *Technology in Cancer Research and Treatment* **4**, 455-482 (2005).

17. Annual Report 3 for this project.

18. M. Xu, M. Alrubaiee, S. K. Gayen, and R. R. Alfano, "Optical high resolution cross section imaging of a hum an breast model usin g independent com ponent analysis in CW and time domain," *Proceedings of SPIE,* Vol.6434, 643416 (2007).

19. M. Xu, M. Alrubaiee, S . K. Gayen and R. R. Alfano, "Optical diffuse im aging of a n *ex vivo* m odel cancerous hum an breast using independent component analysis," *IEEE J. Select. Topics Quantum Electron.* **14**, 43 (2008).

20. S. G. De mos and R. R. Alfano, "Optical polarization im aging," *Appl. Opt.* **36**, 150 (1997).

21. S. K. Gayen, M. E. Zevallos, M. Alrubaie e, J. M. Evans, and R. R. Alfano, "Two-dimensional near-infrared transillum ination im aging of biom edical m edia with a chromium-doped forsterite laser," *Appl. Opt.* **37**, 5327 (1998).

22. N. Kroman, J. W ohlfahrt, H. T. Mouridsen, and M. Melbye, "Influence of tum or location on breast cancer prognosis," *Int. J. Cancer* **105**, 542 -545 (2003).

23. G. Zhan g, S. G. Demos, R. R. Alfano, "F ar-red and NIR spectral wing em ission from tissues under 532 and 632 nm photo excitation," *Lasers Life Sci.* **9**, 1-16 (1999).

10. APPENDICES

Appendix 1.   M. Xu, M. Alrubaiee, S . K. Gayen a nd R. R. Alfano, "Three-dim ensional optical imaging of objects in a turbid m edium using independent com ponent analysis: theory and simulation," *J. Biomed. Opt.* **10**, 051705 (2005).

Appendix 2.   M. Alrubaiee, M. Xu, S. K. Ga yen, M. Brito, and R. R. Al fano, "Three-dimensional optical tomographic im aging of objects in tissue-s imulating turb id medium using independent com ponent analysis," *Appl. Phys. Lett.* **87**, 191112 (2005).

Appendix 3.   M. Alrubaiee, M. Xu, S. K. Gayen, a nd R. R. Alfano, "Fluorescence optical tomography using independent component an alysis to detect sm all objects in turbid media," in Optical Tom ography and Spectroscopy of Tissue VI, edited by Britton Chance, Robert R. Alfano, Bruce J. Tromberg, Mamoru Ta mura, Eva M. Sevick-Muraca, Proceedings of SPIE Vol. 5693 (SPIE, Bellingh am, WA, 2005), pp. 221-224.

Appendix 4.   M. Xu, M. Alrubaiee, S. K. Gayen, and R. R. Alfano, "Optical tomography using independent component analysis to detect absorptive, scattering, or fluorescent inhomogeneities in turbid media," in *Optical Tomography and Spectroscopy of Tissue VI,* edited by Britton Chance, Robert R. Alfano, Bruce J. Tromberg, Mamoru Tamura, Eva M. Sevick-Muraca, Proceedings of SPIE Vol. 5693 (SPIE, Bellingham, WA, 2005), pp. 528 – 535.

Appendix 5.   M. Alrubaiee, M. Xu, S. K. Gayen, and R. R. Alfano, "Three-dim ensional localization and cross section reco nstruction o f f luorescent targ ets in *ex vivo* breast tissue using independent component analysis," *Appl. Phys. Lett.* **89**, 133902 (2006).

Appendix 6.   W. Cai, M. Alrubaiee, S. K. Gayen, M. Xu, and R. R. Alfano, "Three-dimensional optical tomography of objects in turbid media using the 'round-trip m atrix," in Optical Tomography and Spectroscopy of Ti ssue VI, edited by Britton Chance, Robert R. Alfano, Bruce J. Trom berg, Mamoru Tamura, Eva M. Sevick-Muraca, Proceedings of SPIE, Vol. 5693 (SPIE, Bellingham, WA, 2005), pp. 4-9.

Appendix 7.   W. Cai, Xi aohui Ni, S. K. Gayen, a nd R. R. Alfano, "Analytical cum ulant solution of the vec tor r adiative tra nsfer equation investigates backscattering of circularly polarized light from turbid media," *Phys. Rev. E* **74**, 056605 (2006).

Appendix 8.   M. Xu, M. Alrubaiee, S. K. Gayen, a nd R. R. Alfano, " Determination of light absorption, scattering and anisotropy factor of a highly scattering m edium using backscattered circul ar p olarized lig ht." *Proceedings of SPIE* Vol. 6435, 64350J (2007).

Appendix 9.   M. Xu, M. Alrubaiee, S. K. Gayen and R. R. Alfano, "Optical diffuse im aging of an *ex vivo* m odel cancerous hum an breast using independent com ponent analysis," *IEEE J. Select. Topics Quantum Electron.* **14**, 43 (2008).

Appendix 10.   Yimin Wang, M. Alrubaiee, S. K. Gayen, and R. R. Alfano, "Detection of a target in a highly scattering turbid m edium us ing near-infrared c enter of in tensity tim e gated imaging," *Optics Communications* (to be submitted).

Optical imaging of turbid media using independent component analysis: theory and simulation

M. Xu
M. Alrubaiee
S. K. Gayen
R. R. Alfano
The City College and Graduate Center of the City
    University of New York
Department of Physics
Institute for Ultrafast Spectroscopy and Lasers
New York, New York 10031

Abstract. A new imaging approach for 3-D localization and characterization of objects in a turbid medium using independent component analysis (ICA) from information theory is developed and demonstrated using simulated data. This approach uses a multisource and multidetector signal acquisition scheme. ICA of the perturbations in the spatial intensity distribution measured on the medium boundary sorts out the embedded objects. The locations and optical characteristics of the embedded objects are obtained from a Green's function analysis based on any appropriate model for light propagation in the background medium. This approach is shown to locate and characterize absorptive and scattering inhomogeneities within highly scattering medium to a high degree of accuracy. In particular, we show this approach can discriminate between absorptive and scattering inhomogeneities, and can locate and characterize complex inhomogeneities, which are both absorptive and scattering. The influence of noise and uncertainty in background absorption or scattering on the performance of this approach is investigated. © *2005 Society of Photo-Optical Instrumentation Engineers.* [DOI: 10.1117/1.2101568]

Keywords: image processing; image reconstruction; medical imaging; inverse problems; absorption; scattering; diffusion; radiative transfer.

Paper SS04240R received Dec. 7, 2004; revised manuscript received Feb. 25, 2005; accepted for publication Mar. 14, 2005; published online Oct. 24, 2005.

1 Introduction

Optical probing of the interior of multiply scattering colloidal suspensions and biological materials has attracted much attention over the last decade. In particular, biomedical optical tomography and spectroscopy, which has the potential to provide functional information about brain activities and diagnostic information about tumors in breast and prostate, are being actively pursued.[1–17] Simultaneous developments in experimental apparatus and techniques for object interrogation and signal acquisition,[2,4,5,18,19] analytical models for light propagation,[10,20–22] and computer algorithms for image reconstruction[6,8] hold promise for realization of these potentials of optical tomography.

Multiple scattering of light in thick turbid media precludes direct imaging of embedded targets. One typically uses an inverse image reconstruction[6,8] (IIR) approach to reconstruct a map of the optical properties, such as absorption coefficient (μ_a) and scattering coefficient (μ_s), of the medium by matching the measured light intensity distribution on the boundary of the turbid medium to that calculated by a forward model for the propagation of light in that medium. The commonly used forward models include the radiative transfer equation[17,23] (RTE), the diffusion approximation (DA) of the RTE (Refs. 6 and 8), and random walk of photons.[24,25]

The inversion problem is ill-posed and must be regularized to stabilize the inversion at a cost of reduced resolution.[8,26] Both iterative reconstruction and noniterative linearized inversion approaches have been used to solve the inversion problem in optical tomography, which is weakly nonlinear, with limited success. Reconstruction of images with adequate spatial resolution and accurate localization and characterization of the inhomogeneities remain a formidable task. The time required for data acquisition and image reconstruction is another important consideration.

In this paper, we present a novel algorithm based on the independent component analysis[27,28] (ICA) from information theory to locate absorptive and scattering inhomogeneities embedded in a thick turbid medium and demonstrate the efficacy using simulated data. ICA has been successfully applied in various other applications such as electroencephalogram and nuclear magnetic resonance spectroscopy.[28–31] We refer to this information theory-inspired approach as optical imaging using independent component analysis, abbreviated as, OPTICA. The novelty of OPTICA over other ICA applications is that OPTICA associates directly the independent components to the Green's functions responsible for light propagation in the turbid medium from the inhomogeneities to the source and the detector, and therefore the retrieved independent components can be used to locate and characterize the inhomogeneities.

OPTICA uses a multisource illumination and multidetector signal acquisition scheme providing a variety of spatial and

Address all correspondence to M. Xu, the City College of the City University of New York, Department of Physics, J419, 138th Street and Convent Avenue, New York, New York 10031. Tel.: (212) 650-6865; Fax: (212) 650-5530; E-mail: minxu@sci.ccny.cuny.edu

angular views essential for three-dimensional (3-D) object localization. Each object (or inhomogeneity) within the turbid medium alters the propagation of light through the medium. The influence of an object on the spatial distribution of the light intensity at the detector plane involves propagation of light from the source to the object, and from the object to the detector, and can be described in terms of two Green's functions (propagators) describing light propagation from source to the object and that from the object to the detector, respectively.

The absorptive or scattering inhomogeneities illuminated by the incident wave are assumed to be virtual sources, and the perturbation of the spatial distribution of the light intensity on the medium boundary is taken to be some weighted mixture of signals arriving from these virtual sources. These virtual sources are statistically independent and can be recovered by ICA of the recorded data set. The number of leading independent components is same as the number of embedded objects. The location and characterization of inhomogeneities are obtained from the analysis of the retrieved virtual sources using an appropriate model of light propagation in the background medium.

The remainder of this paper is organized as follows. Section 2 presents a brief introduction to ICA and reviews the general theoretical framework for OPTICA. Section 3 presents the results from simulations for different configurations. Implications of these results are discussed in Sec. 4.

2 Theoretical Formalism

2.1 ICA

Blind source separation is a class of problem of general interest that consists of recovering unobserved signals or virtual sources from several observed mixtures. Typically the observations are the output of a set of sensors, where each sensor receives a different combination of the source signals. Prior knowledge about the mixture in such problems is usually not available. The lack of prior knowledge is compensated by a statistically strong but often physically plausible assumption of independence between the source signals. Over the last decade, ICA has been proposed as a solution to the blind source separation problem and has emerged as a new paradigm in signal processing and data analysis.[27,28,31,32]

The simplest ICA model, an instantaneous linear mixture model,[32] assumes the existence of n independent signals $s_i(t)$ $(i=1,2,\ldots,n)$ and the observation of at least as many mixtures $x_i(t)$ $(i=1,2,\ldots,m)$ by $m \geq n$ sensors, these mixtures being linear and instantaneous, i.e., $x_i(t) = \sum_{j=1}^{n} a_{ij} s_j(t)$ for each i at a sequence of time t. In a matrix notation,

$$\mathbf{x}(t) = \mathbf{A}\mathbf{s}(t), \quad \mathbf{A} \in \mathbb{R}^{m \times n}, \tag{1}$$

where $\mathbf{A}$ is the mixing matrix. The j'th column of $\mathbf{A}$ gives the mixing vector for the j'th virtual source. ICA can be formulated as the computation of an $n \times m$ separating matrix $\mathbf{B}$ whose output

$$\mathbf{y}(t) = \mathbf{B}\mathbf{x}(t) = \mathbf{C}\mathbf{s}(t), \quad \mathbf{B} \in \mathbb{R}^{n \times m}, \quad \mathbf{C} \equiv \mathbf{B}\mathbf{A} \in \mathbb{R}^{n \times n},$$

$$\tag{2}$$

is an estimate of the vector $\mathbf{s}(t)$ of the source signals.

The basic principle of ICA can be understood in the following way. The central limit theorem in probability theory tells us that the distribution of independent random variables tends toward a Gaussian distribution under certain conditions. Thus, a sum of multiple independent random variables usually has a distribution that is closer to Gaussian than any of the original random variables. In Eq. (2) $y_i(t) = \sum_j C_{ij} s_j(t)$, as a summation of independent random variables $s_j(t)$, is usually more Gaussian than $s_j(t)$, while $y_i(t)$ becomes least Gaussian when it in fact equals one of the $s_j(t)$. This heuristic argument shows that ICA can be intuitively regarded as a statistical approach to find the separating matrix $\mathbf{B}$ such that $y_i(t)$ is least Gaussian. This can be achieved by maximizing some measure of non-Gaussianity, such as maximizing kurtosis[32,33] (the fourth-order cumulate), of $y_i(t)$.

ICA separates independent sources from linear instantaneous or convolutive mixtures of independent signals without relying on any specific knowledge of the sources except that they are independent. The sources are recovered by a maximization of a measure of independence (or, a minimization of a measure of dependence), such as non-Gaussianity and mutual information between the reconstructed sources.[31,32] The recovered virtual sources and mixing vectors from ICA are unique up to permutation and scaling.[31,32]

2.2 Optical Imaging Using ICA

The classical approach to propagation of multiply scattered light in turbid media, which assumes that phases are uncorrelated on scales larger than the scattering mean free path l_s, leads to the RTE in which any interference effects are neglected.[34] The RTE does not admit closed-form analytical solutions in bounded regions and its numerical solution is computationally expensive. The commonly used forward models in optical imaging of highly scattering media is[6,8] the DA to RTE.

The approach OPTICA can be applied to different models of light propagation in turbid media, such as the diffusion approximation,[6,8] the cumulant approximation,[20,22,35] the random walk model,[10,24] and radiative transfer[17,34] when they are linearized. The diffusion approximation is valid when the inhomogeneities are deep within a highly scattering medium. We discuss only the formalism of OPTICA in the diffusion approximation in this paper.

In this diffusion approximation, the perturbation of the detected light intensities on the boundaries of the medium, the scattered wave field, due to absorptive and scattering objects (inhomogeneities) can be written as[3,13]

$$\phi_{\text{sca}}(\mathbf{r}_d, \mathbf{r}_s) = -\int G(\mathbf{r}_d, \mathbf{r}) \delta\mu_a(\mathbf{r}) c G(\mathbf{r}, \mathbf{r}_s) d\mathbf{r}$$

$$-\int \delta D(\mathbf{r}) c \nabla_{\mathbf{r}} G(\mathbf{r}_d, \mathbf{r}) \cdot \nabla_{\mathbf{r}} G(\mathbf{r}, \mathbf{r}_s) d\mathbf{r}, \tag{3}$$

to the first order of the Born approximation[36] when illuminated by a point source of unit power, where $\mathbf{r}_s$, $\mathbf{r}$, and $\mathbf{r}_d$ are the positions of the source, the inhomogeneity, and the detector, respectively; $\delta\mu_a = \mu_{a,\text{obj}} - \mu_a$ and $\delta D = D_{\text{obj}} - D$ are the differences in absorption coefficient and diffusion coefficient, respectively, between the inhomogeneity and the background;

c is the speed of light in the medium; and $G(\mathbf{r},\mathbf{r}')$ is the Green's function describing light propagation from $\mathbf{r}'$ to $\mathbf{r}$ inside the background turbid medium of absorption and diffusion coefficients μ_a and D.

Equation (3) is written in the frequency domain and does not explicitly show the modulation frequency ω of the incident wave for clarity. The following formalism applies to continuous wave, frequency-domain, and time-resolved measurements. The time-domain measurement is first Fourier transformed over time to obtain data over many different frequencies.

The Green's function G for a slab geometry in DA is given by

$$G(\mathbf{r},\mathbf{r}') \equiv G(\rho,z,z') = \frac{1}{4\pi D}\sum_{k=-\infty}^{\infty}\left[\frac{\exp(-\kappa r_k^+)}{r_k^+} - \frac{\exp(-\kappa r_k^-)}{r_k^-}\right]$$

$$r_k^{\pm} = [\rho^2 + (z \mp z' \pm 2kd)]^{1/2}, \tag{4}$$

for an incident amplitude-modulated wave of modulation frequency ω, where $k=0,\pm1,\pm2,\ldots,\rho=[(x-x')^2+(y-y')^2]^{1/2}$ is the distance between the two points $\mathbf{r}=(x,y,z)$ and $\mathbf{r}'=(x',y',z')$ projected onto the xy plane; $\kappa=[(\mu_a-i\omega/c)/D]^{1/2}$ is chosen to have a nonnegative real part; and the extrapolated boundaries of the slab are located at $z=0$ and $z=d=L_z+2z_e$, respectively, where L_z is the physical thickness of the slab and the extrapolation length z_e should be determined from the boundary condition of the slab.[37–39] Greens' functions in Eq. (3) for other geometries can be obtained either analytically or numerically.[40,41]

2.2.1 Absorptive inhomogeneities

We first consider absorptive inhomogeneities. Under the assumption that absorptive inhomogeneities are localized, that is, the j'th one is contained in volume V_j centered at $\mathbf{r}_j(1\leq j\leq J)$, the scattered wave field in Eq. (3) can be rewritten as

$$-\phi_{\text{sca}}(\mathbf{r}_d,\mathbf{r}_s) = \sum_{j=1}^{J} G(\mathbf{r}_d,\mathbf{r}_j)q_j G(\mathbf{r}_j,\mathbf{r}_s), \tag{5}$$

where $q_j=\delta\mu_a(\mathbf{r}_j)cV_j$ is the absorption strength of the j'th inhomogeneity. The scattered wave is in a form of an instantaneous linear mixture of Eq. (1). One absorptive inhomogeneity is represented by one virtual source $q_j G(\mathbf{r}_j,\mathbf{r}_s)$ with a mixing vector $G(\mathbf{r}_d,\mathbf{r}_j)$.

As the virtual source $q_j G(\mathbf{r}_j,\mathbf{r}_s)$ at the j'th inhomogeneity is independent of the virtual sources at other locations, ICA can be used with the observations obtained for the light source at $n\gg J$ different positions to separate out both virtual sources $s_j(\mathbf{r}_s)$ and the mixing vectors[27,32] $a_j(\mathbf{r}_d)$. The j'th virtual source $s_j(\mathbf{r}_s)$ and the j'th mixing vector $a_j(\mathbf{r}_d)$ provide the scaled projections of the Green's function on the source and detector planes, $G(\mathbf{r}_j,\mathbf{r}_s)$ and $G(\mathbf{r}_d,\mathbf{r}_j)$, respectively. We can write

$$s_j(\mathbf{r}_s) = \alpha_j G(\mathbf{r}_j,\mathbf{r}_s),$$

$$a_j(\mathbf{r}_d) = \beta_j G(\mathbf{r}_d,\mathbf{r}_j), \tag{6}$$

where α_j and β_j are scaling constants for the j'th inhomogeneity.

Both the location and strength of the j'th object can be computed by a simple fitting procedure using Eq. (6). We adopted a least-squares fitting procedure given by:

$$\min_{\mathbf{r}_j,\alpha_j,\beta_j}\left\{\sum_{\mathbf{r}_s}[\alpha_j^{-1}s_j(\mathbf{r}_s)-G(\mathbf{r}_j,\mathbf{r}_s)]^2 + \sum_{\mathbf{r}_d}[\beta_j^{-1}a_j(\mathbf{r}_d)-G(\mathbf{r}_d,\mathbf{r}_j)]^2\right\}. \tag{7}$$

The fitting yields the location $\mathbf{r}_j$ and the two scaling constants α_j and β_j for the j'th inhomogeneity whose absorption strength is then given by $q_j=\alpha_j\beta_j$.

2.2.2 Scattering inhomogeneities

For scattering inhomogeneities, a similar analysis shows the scattered wave can be written as

$$-\phi_{\text{sca}}(\mathbf{r}_d,\mathbf{r}_s) = \sum_{j=1}^{J'} g_z(\mathbf{r}_j,\mathbf{r}_d)q_j' g_z(\mathbf{r}_j,\mathbf{r}_s)$$
$$+ \sum_{j=1}^{J'} \rho_{dj}\cos\theta_d g_{\perp}(\mathbf{r}_j,\mathbf{r}_d)q_j'\rho_{sj}\cos\theta_s g_{\perp}(\mathbf{r}_j,\mathbf{r}_s)$$
$$+ \sum_{j=1}^{J'} \rho_{dj}\sin\theta_d g_{\perp}(\mathbf{r}_j,\mathbf{r}_d)q_j'\rho_{sj}\sin\theta_s g_{\perp}(\mathbf{r}_j,\mathbf{r}_s), \tag{8}$$

where $q_j'=\delta D(\mathbf{r}_j)cV_j'$ is the diffusion strength of the j'th scattering inhomogeneity of volume V_j' $(j=1,2,\ldots,J')$; $\rho_{dj}=[(x_d-x_j)^2+(y_d-y_j)^2]^{1/2}$, $\rho_{sj}=[(x_s-x_j)^2+(y_s-y_j)^2]^{1/2}$; θ_d and θ_s are the azimuthal angles of $\mathbf{r}_d-\mathbf{r}_j$ and $\mathbf{r}_s-\mathbf{r}_j$, respectively, and the two auxiliary functions are given by

$$g_{\perp}(\mathbf{r},\mathbf{r}') = \frac{1}{4\pi D}\sum_{k=-\infty}^{+\infty}\left[(\kappa r_k^+ + 1)\frac{\exp(-\kappa r_k^+)}{(r_k^+)^3} - (\kappa r_k^- + 1)\frac{\exp(-\kappa r_k^-)}{(r_k^-)^3}\right], \tag{9}$$

and

$$g_z(\mathbf{r},\mathbf{r}') = \frac{1}{4\pi D}\sum_{k=-\infty}^{+\infty}\left\{(z-z'+2kd)(\kappa r_k^+ + 1)\frac{\exp(-\kappa r_k^+)}{(r_k^+)^3} - (z+z'-2kd)(\kappa r_k^- + 1)\frac{\exp(-\kappa r_k^-)}{(r_k^-)^3}\right\}. \tag{10}$$

The scattered wave from one scattering inhomogeneity is thus a mixture of contributions from $(3J')$ virtual sources:

$$q_j'g_z(\mathbf{r}_j,\mathbf{r}_s), \quad q_j'\rho_{sj}\cos\theta_s g_{\perp}(\mathbf{r}_j,\mathbf{r}_s), \quad q_j'\rho_{sj}\sin\theta_s g_{\perp}(\mathbf{r}_j,\mathbf{r}_s), \tag{11}$$
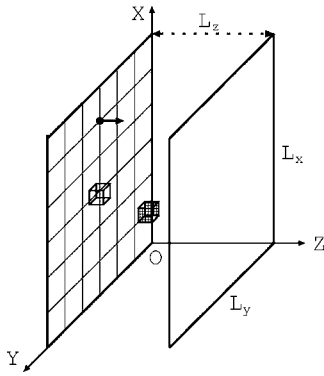
with mixing vectors

Fig. 1 Light intensity on one side of the slab is measured when a point source scans on the other side. Two inhomogeneities are placed at (50, 60, 20) and (30, 30, 30) mm inside the slab.

$$g_z(\mathbf{r}_j, \mathbf{r}_d), \quad \rho_{dj} \cos \theta_d g_\perp(\mathbf{r}_j, \mathbf{r}_d), \quad \rho_{dj} \sin \theta_d g_\perp(\mathbf{r}_j, \mathbf{r}_d),$$

$$(12)$$

where $1 \leqslant j \leqslant J'$, respectively. Both the location and strength of the j'th scattering object are computed by fitting the retrieved virtual sources and mixing vectors to Eqs. (11) and (12) using a least-squares procedure, respectively.

There are, in general, three virtual sources of specific patterns (one centrosymmetric and two dumbbell-shaped) associated with one scattering inhomogeneity, whereas only one centrosymmetric virtual source is associated with one absorptive inhomogeneity. This difference may serve as the basis to discriminate absorptive and scattering inhomogeneities.

The only assumption made in OPTICA is that virtual sources are mutually independent. The number of inhomogeneities within the medium is determined by the number of the independent components presented in the multisource multidetector data set. No specific light propagation model is assumed in this step. The analysis of retrieved independent components from ICA then localizes and characterizes the absorptive and scattering inhomogeneities inside the turbid medium using an appropriate model of the light propagator. Extra independent components may appear, depending on the level of noise in the data. These components can be discarded and only the leading independent components must be analyzed to detect and characterize inhomogeneities of interest.

3 Results

Simulations were performed for a 50-mm-thick slab, as shown schematically in Fig. 1. The absorption and diffusion coefficients of the uniform slab are $\mu_a = 1/300$ mm^{-1} and $D = 1/3$ mm, respectively, close to that of human breast tissue.[42] The incident cw beam scans a set of 21×21 grid points covering an area of 90×90 mm^2. The spacing between two consecutive grid points is 4.5 mm. This light intensity on the other side of the slab is recorded by a CCD camera on 42×42 grid points covering the same area.

In the simulations presented in the following subsections, we fix the ratio of strength of absorption to that of diffusion to be 0.01, which produce perturbations of comparable magnitude on the light intensities measured on the detector plane from the absorption and scattering inhomogeneities. As the
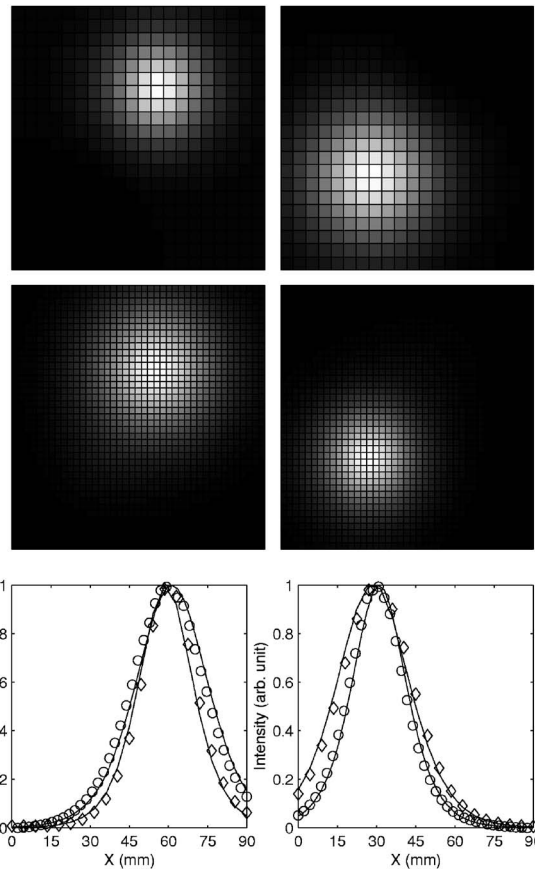
Fig. 2 Normalized independent spatial intensity distributions on the input (or source) plane (the first row), the exit (or detector) plane (the second row), and the least-squares fitting using Eq. (7) (the third row). The left column is for the first absorptive inhomogeneity at (50, 60, 20) mm and the right column is for the second absorptive inhomogeneity at (30, 30, 30) mm. On the third row, the horizontal profile of intensity distributions on the source plane (diamonds) and on the detector plane (circles) are displayed, and solid lines show the respective Green's function fit used for obtaining locations and strengths of objects. The noise level is 5%.

scattered wave is linear with respect to the absorption and diffusion strengths, we also set the strength of either absorption or diffusion to be unity in simulations for convenience.

3.1 Absorptive Inhomogeneities

Two absorptive inhomogeneities, each of a unity absorption strength, are placed at positions (50, 60, 20) and (30, 30, 30) mm, respectively. Gaussian noise of 5% was added to the simulated light intensity change on the detector plane. OPTICA operates on a noisy scattering wave $-\phi_{\text{sca}}(\mathbf{r}_d, \mathbf{r}_s)[1 + n(\mathbf{r}_d, \mathbf{r}_s)]$, where $n(\mathbf{r}_d, \mathbf{r}_s)$ is a Gaussian random variable of a standard deviation 0.05.

ICA of the perturbations in the spatial intensity distributions provided corresponding independent intensity distributions on the source and detector planes. ICA-generated independent intensity distributions on the source and detector planes are shown in Fig. 2 for the two absorptive inhomogeneities. Locations of the absorptive objects are obtained from fitting these independent component intensity distributions to those of the diffusion approximation in a slab Eq. (4) by the
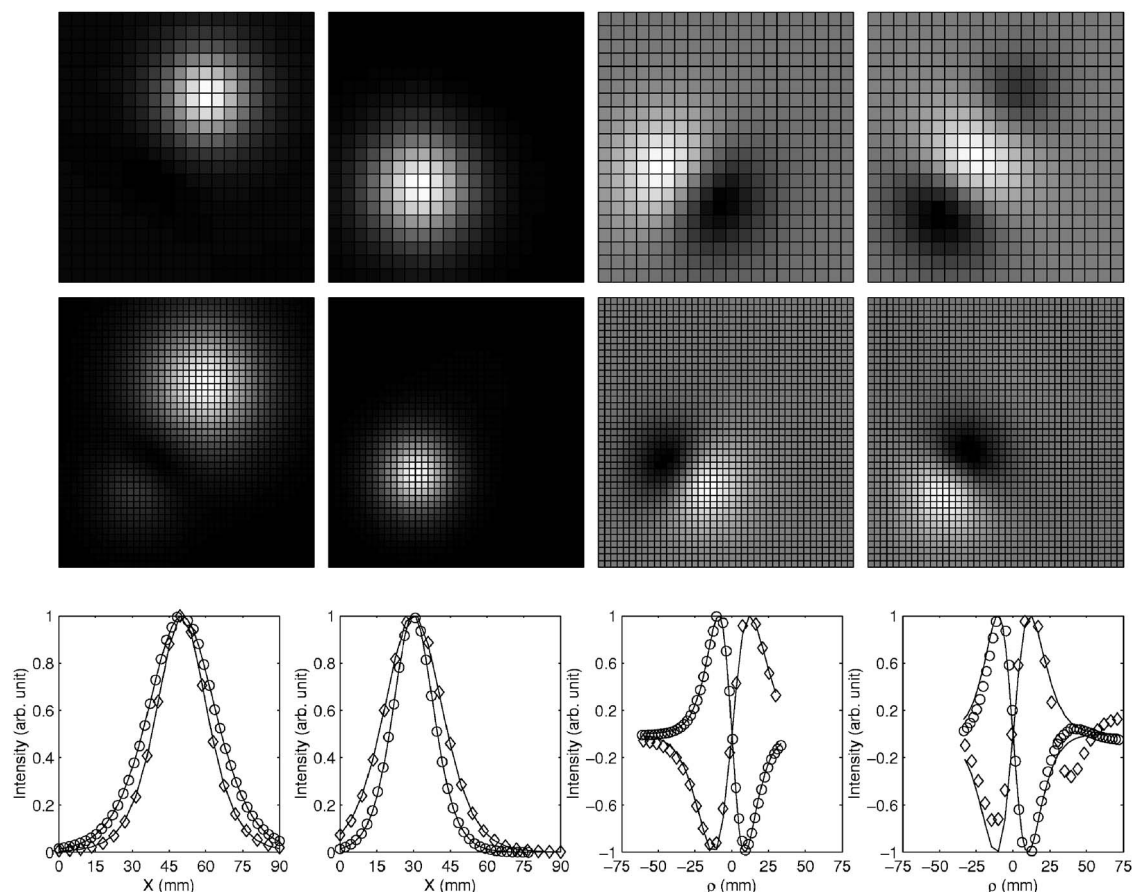
Fig. 3 Normalized independent spatial intensity distribution on the source plane, i.e., virtual sources (the first row) and on the detector plane, i.e., mixing vectors (the second row), and the least-squares fitting (the third row). The first column is for the first absorptive inhomogeneity at $(50,60,20)$ mm and the second through fourth columns are for the second scattering inhomogeneity at $(30,30,30)$ mm and represent the centrosymmetric and two dumbbell-shaped pairs of virtual sources and mixing vectors, respectively. The dumbbell comprises one bright part and its antisymmetric dark counterpart. In the third row, the profile of intensity distributions on the source plane (diamonds) and on the detector plane (circles) are displayed, and solid lines show the respective Green's function fit used for obtaining locations and strengths of objects. The X coordinate is the horizontal coordinate. The ρ coordinate is the coordinate on the symmetrical line passing through the dumbbell axis. The small dark circular region appearing near the right-upper corner of the normalized independent spatial intensity distribution on the first row and in the fourth column is an artifact.

least-squares procedure of Eq. (7). The first object is found at $(50.0,60.0,20.0)$ mm and the second one at $(30.0,30.0,30.1)$ mm. The coordinates of both objects agree to within 0.1 mm of their known locations. The strengths of the two objects are $q_1=1.00$ and $q_2=0.99$, respectively, with an error not greater than 1% of the true values.

3.2 *Discrimination between Absorptive and Scattering Inhomogeneities*

In the second example, one absorptive object of absorption strength of 0.01 is placed at $(50,60,20)$ mm and one scattering object of diffusion strength of negative unity (corresponding to an increase in scattering for the inhomogeneity) is placed at $(30,30,30)$ mm, respectively. We added 5% Gaussian noise to the simulated light intensity change on the detector plane.

Figure 3 shows the ICA-generated independent intensity distributions on the source and detector planes and the least-squares fitting. The first column corresponds to the absorptive inhomogeneity. The second through fourth columns corre-

spond to the scattering object, which produces one pair of centrosymmetric and two pairs of dumbbell-shaped virtual sources and mixing vectors. The absorptive inhomogeneity is found to be at $(50.2,60.3,20.2)$ mm with a strength q_1 $=0.0101$. The scattering object produces three pairs (one centrosymmetric and two dumbbell-shaped) of virtual sources and mixing vectors centering around the position (x,y) $=(30,30)$ mm (see the second through fourth columns in Fig. 3). The dumbbell-shaped virtual source or mixing vector comprises one bright part and its antisymmetric dark counterpart. The resolved position and strength of the scattering object are found to be $(30.0,30.0,30.0)$ mm and $q_2=-0.99$, $(32.1,32.4,30.2)$ mm and $q_2=-0.96$, and $(31.3,30.2,27.1)$ mm and $q_2=-1.05$, respectively, through fitting to the individual pair. For the scattering object, the best result is obtained from the fitting to the first pair of centrosymmetric virtual source and mixing vector from the scattering object. Taking the position and strength of the scattering object to be that from fitting the centrosymmetric virtual source and mixing vector, the error of the resolved positions
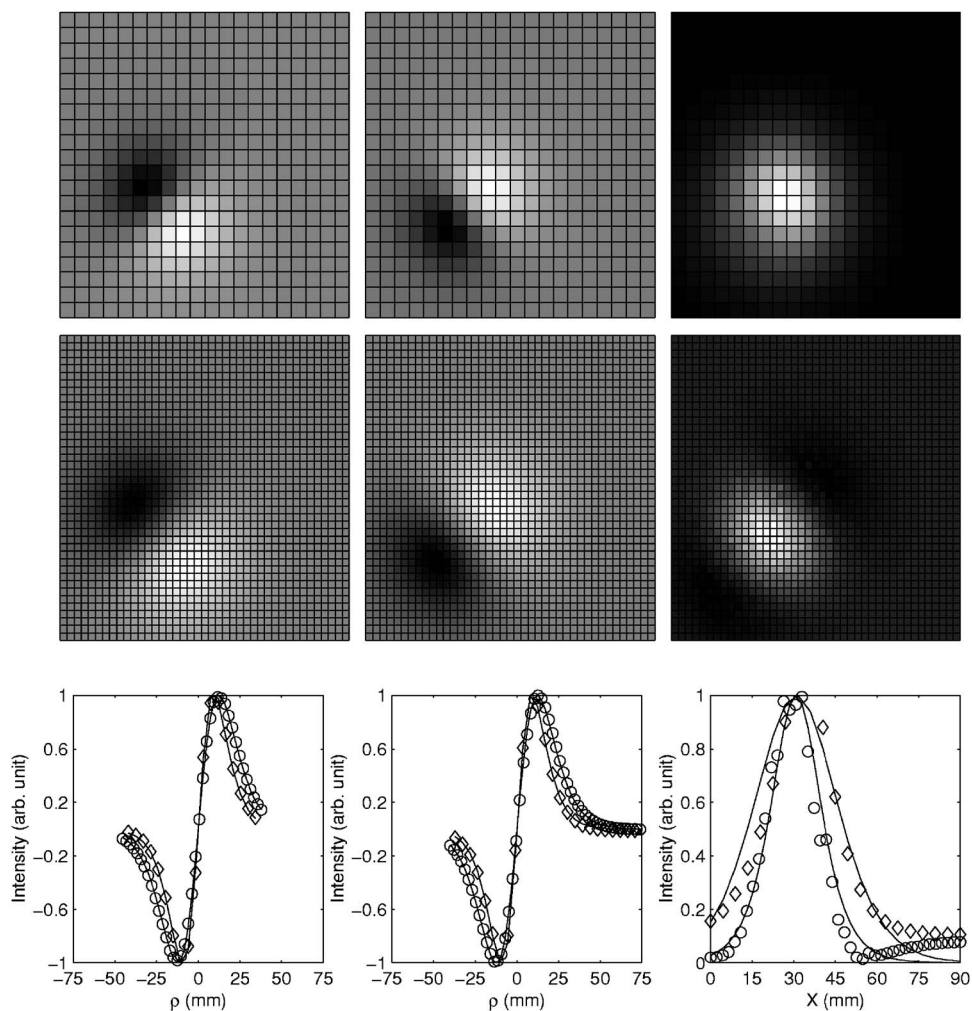
Fig. 4 Normalized independent spatial intensity distribution on the source plane (the first row) and on the detector plane (the second row), and the least-squares fitting (the third row) for one inhomogeneity located at $(30, 30, 20)$ mm with strengths of absorption $q_1 = 0.01$ and diffusion $q_2 = 1$. The first and second columns correspond to the pairs of dumbbell-shaped virtual sources and mixing vectors produced by its scattering component. The third column corresponds to its absorptive component obtained by first removing the scattering contribution. In the third row, the profile of intensity distributions on the source plane (diamonds) and on the detector plane (circles) are displayed, and solid lines show the respective Green's function fit used to obtain locations and strengths of objects. The X coordinate is the horizontal coordinate and the ρ coordinate is the coordinate on the symmetrical line passing through the dumbbell axis.

of both objects is within 0.3 mm of their known locations. The error of the resolved strengths of both objects is approximately 1% of the true values.

3.3 Colocated Absorptive and Scattering Inhomogeneities

For one complex inhomogeneity that is both absorptive and scattering, the two pairs of dumbbell-shaped virtual sources and mixing vectors produced by its scattering abnormality can be used to obtain its scattering strength. By subtracting the scattering contribution off the measured scattered wave, our procedure can be applied again to the cleaned data and we proceed to obtain its absorption strength. The third example considers a complex inhomogeneity at $(30, 30, 20)$ mm with strengths of absorption $q_1 = 0.01$ and diffusion $q_2 = 1$ (corresponding to a decrease in scattering), respectively. We added 5% Gaussian noise to the simulated light intensity change on the detector plane.

Figure 4 shows the ICA-generated independent intensity distributions on the source and detector planes and the least-squares fitting. The first and second columns correspond to the pairs of dumbbell-shaped virtual sources and mixing vectors produced by its scattering component. The position and strength of this diffusive component is obtained to be $(32.7, 33.0, 20.5)$ mm and $q_2 = 0.95$, and $(31.7, 30.1, 20.4)$ mm and $q_2 = 0.96$ by fitting the two individual dumbbell-shaped pairs, respectively. The position and strength of the diffusive component is found to be $(30.9, 30.9, 20.4)$ mm and $q_2 = 0.95$ if both dumbbell-shaped virtual sources and mixing vectors are used in fitting. The third column of Fig. 4 corresponds to its absorptive component obtained by first removing the scattering contribution from the measured scattered wave. The depth and strength of the absorption component is found to be $(30.8, 30.7, 32.7)$ mm and $q_1 = 0.0091$.
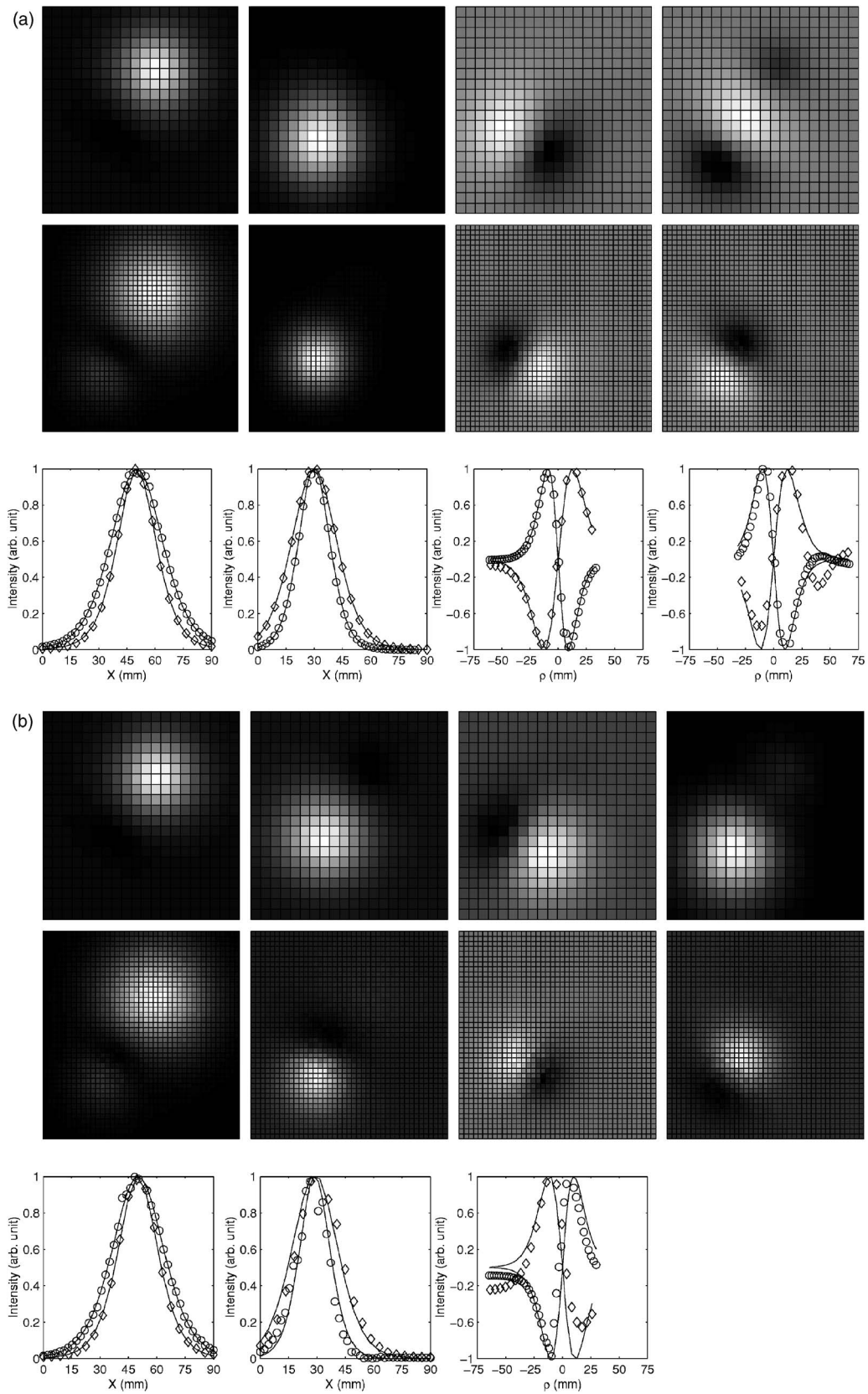
Fig. 5 Same as Fig. 3 with (a) 10% and (b) 20% Gaussian noise. The dumbbell-shaped virtual source on the source plane in the fourth column of (b) is deformed and the least-squares fitting is not shown.

Table 1 Comparison of known and OPTICA determined positions and strengths of absorption (Abs) and scattering (Sca) inhomogeneities under different levels of Gaussian noise.

Noise	Target	Known Position (x, y, z) (mm)	Known Strength	Resolved Position (x, y, z) (mm)	Resolved Strength	Error in Position (mm)	Error in Strength (%)
5%	Abs	(50, 60, 20)	0.01	(50.2, 60.3, 20.2)	0.0101	~0.3	~1
	Sca	(30, 30, 30)	−1	(30.0, 30.0, 30.0)	−0.99	~0.1	~1
10%	Abs	(50, 60, 20)	0.01	(50.2, 60.3, 20.1)	0.0101	~0.3	~1
	Sca	(30, 30, 30)	−1	(30.0, 30.1, 30.0)	−0.98	~0.1	~2
20%	Abs	(50, 60, 20)	0.01	(50.1, 60.3, 20.5)	0.0102	~0.5	~2
	Sca	(30, 30, 30)	−1	(28.9, 27.0, 32.9)	−0.59	~3	~50

The error in positioning the scattering component is less than 1 mm and the error of the resolved strength of the scattering strength is ~5%. The errors in positioning and the resolved strength of the absorptive component equal ~3 mm and ~10%, respectively, which are larger than those of the scattering component because the error is amplified when the estimated scattering component is used in subtraction off its contribution to the scattered wave in our procedure.
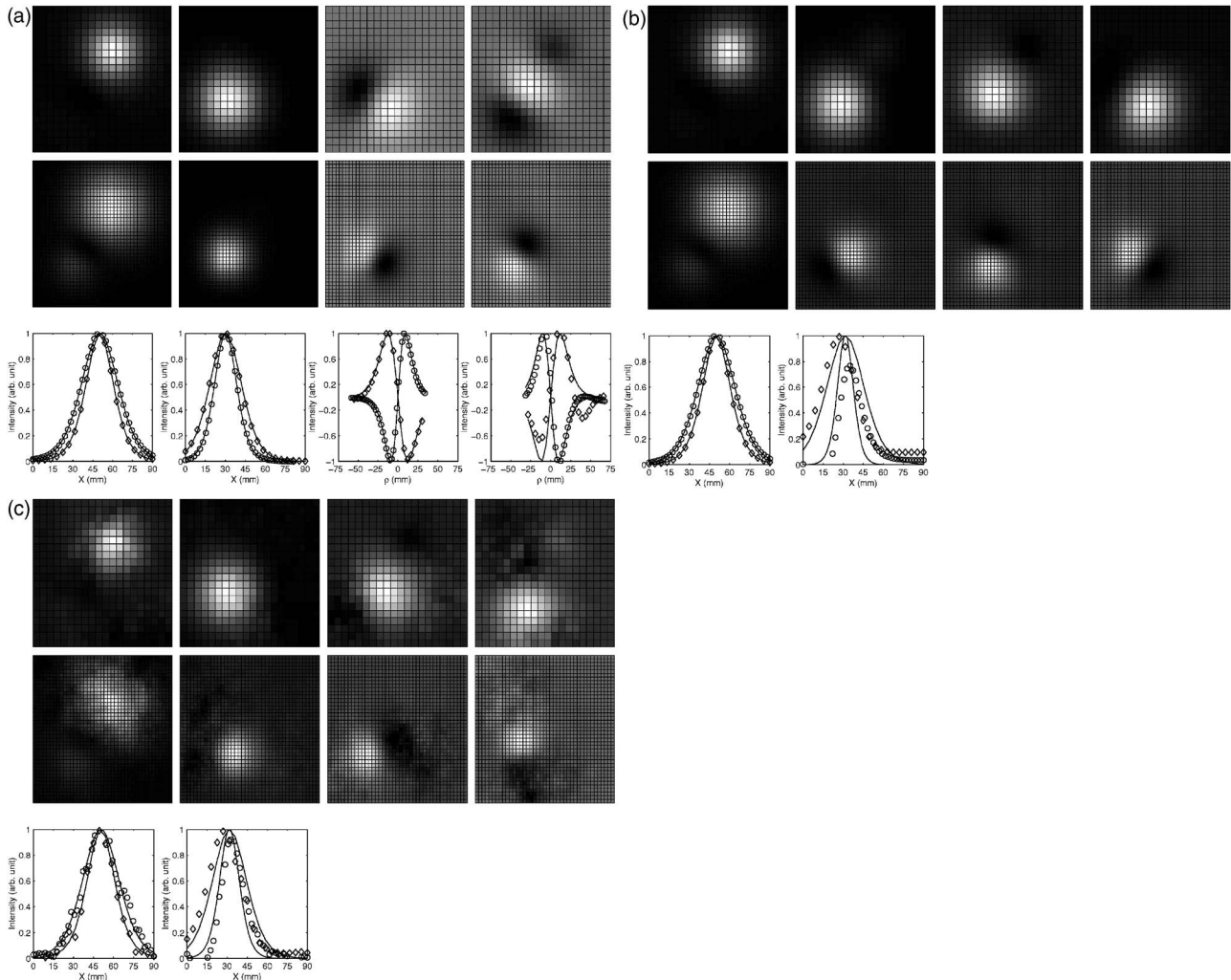
Fig. 6 Same as Fig. 3 with (a) 40, (b) 34, and (c) 10 dB background absorption uncertainty.

Table 2 Comparison of known and OPTICA determined positions and strengths of absorption (Abs) and scattering (Sca) inhomogeneities under different levels of background absorption uncertainty.

SNR (dB)	Target	Known Position (x, y, z) (mm)	Known Strength	Resolved Position (x, y, z) (mm)	Resolved Strength	Error in Position (mm)	Error in Strength (%)
40	Abs	(50, 60, 20)	0.01	(50.2, 60.3, 20.1)	0.0101	~0.3	~1
	Sca	(30, 30, 30)	−1	(30.1, 30.1, 30.0)	−0.99	~0.1	~1
34	Abs	(50, 60, 20)	0.01	(50.2, 60.3, 20.1)	0.0100	~0.3	~1
	Sca	(30, 30, 30)	−1	(31.6, 31.7, 25.3)	−0.52	~5	~50
10	Abs	(50, 60, 20)	0.01	(50.6, 60.3, 20.3)	0.0090	~0.3	~10
	Sca	(30, 30, 30)	−1	(31.7, 29.6, 31.7)	−0.78	~5	~50

3.4 Effect of Noise

To demonstrate the effect of noise on the performance of OPTICA, different levels of Gaussian noise were added to the simulated light intensity change on the detector plane.

Figure 5 shows the case presented in Fig. 3 of Sec. 3.2 with, instead, 10 and 20% Gaussian noise added to the scattered wave. The resolved absorptive inhomogeneity is at $(50.2, 60.3, 20.1)$ mm with strength 0.0101 at 10% noise, and at $(50.1, 60.3, 20.5)$ mm with strength 0.0102 at 20% noise. The resolved position and strength of the scattering object are found to be $(30.0, 30.1, 30.0)$ mm and $q_2 = -0.98$, $(32.1, 32.4, 30.4)$ mm and $q_2 = -0.95$, and $(31.4, 30.1, 27.5)$ mm and $q_2 = -1.00$, respectively, through fitting to the pair of centrosymmetric and two pairs of dumbbell-shaped virtual sources and mixing vectors [see the second to fourth columns of Fig. 5(a)], respectively, at 10% noise. The resolved values become $(28.9, 27.0, 32.9)$ mm and $q_2 = -0.59$ from fitting the pair of centrosymmetric virtual source and mixing vector [see the second column of Fig. 5(b)], and $(30.3, 32.3, 26.6)$ mm and $q_2 = -1.33$ from fitting the first pair of dumbbell-shaped virtual source and mixing vector [see the third column of Fig. 5(b)], respectively, at 20% noise. The dumbbell-shaped virtual source in the source plane, of the second pair of dumbbell-shaped virtual source and mixing vector, is deformed and the fitting is not shown [see the fourth column of Fig. 5(b)]. The deformation of dumbbell appears first in the source plane with the increase of noise as the grid spacing on the source plane is larger than that in the detector plane in the simulation.

The error in localization and characterization of scattering inhomogeneities increases rapidly with the increase of noise, from ~0.1 mm in positioning and ~2% in strength at 10% noise to ~3 mm in positioning and ~50% in strength at 20% noise. On the other hand, the effect of noise on localization and characterization of absorptive inhomogeneities is much smaller, the errors at both noise levels are less than 0.5 mm in positioning and ~2% in strength. The results in Sec. 3.2 and this section are summarized in Table 1.

3.5 Effect of Uncertainty in Background

In the examples discussed here, we have assumed the light intensities change measured on the detector plane is obtained with an exact knowledge about the background. To examine the effect of uncertainty in background optical property on the performance of OPTICA, we model the error in the estimation of the background absorption or diffusion coefficients as a uniform Gaussian random field $f(\mathbf{r})$. The Gaussian noise addressed in Sec. 3.4 is set to be zero here. OPTICA operates on a "dirty" scattering wave $-\phi_{\mathrm{sca}}(\mathbf{r}_d, \mathbf{r}_s) + \delta\phi_{\mathrm{sca}}(\mathbf{r}_d, \mathbf{r}_s)$, where $\delta\phi_{\mathrm{sca}}(\mathbf{r}_d, \mathbf{r}_s)$ is the change in the scattered wave from that of a uniform background of absorption μ_a (or diffusion D) to that of a background of absorption $\mu_a + f(\mathbf{r})$ [or diffusion $D + f(\mathbf{r})$]. The magnitude of the background uncertainty is represented by the signal-to-noise ratio (SNR) defined by

$$\mathrm{SNR(dB)} = 10 \log_{10} \frac{\sum_{\mathbf{r}_d} \sum_{\mathbf{r}_s} |\phi_{\mathrm{sca}}(\mathbf{r}_d, \mathbf{r}_s)|^2}{\sum_{\mathbf{r}_d} \sum_{\mathbf{r}_s} |\delta\phi_{\mathrm{sca}}(\mathbf{r}_d, \mathbf{r}_s)|^2}. \quad (13)$$

Figures 6(a)–6(c) show the case presented in Fig. 3 of Sec. 3.2 with 40, 34, and 10 dB SNR due to background absorption uncertainty, respectively. The resolved absorptive inhomogeneity is at $(50.2, 60.3, 20.1)$ mm with strength 0.0101 at 40 dB SNR, and at $(50.2, 60.3, 20.1)$ mm with strength 0.0100 at 34 dB SNR, and at $(50.6, 60.3, 20.3)$ mm with strength 0.0090 at 10 dB SNR.

The resolved position and strength of the scattering object are found to be $(30.1, 30.1, 30.0)$ mm and $q_2 = -0.99$, $(32.1, 32.9, 30.0)$ mm and $q_2 = -0.95$, and $(31.4, 30.0, 27.5)$ mm and $q_2 = -1.01$, respectively, through fitting to the pair of centrosymmetric and two pairs of dumbbell-shaped virtual sources and mixing vectors [see the second to fourth columns of Fig. 5(a)], respectively, at 40 dB SNR. The resolved values become $(31.6, 31.7, 25.3)$ mm and $q_2 = -0.52$ and $(31.7, 29.6, 31.7)$ mm and $q_2 = -0.78$ at 34 dB and 10 dB SNRs, respectively, from fitting the pair of centrosymmetric virtual source and mixing vector [see the second columns of Figs. 5(b) and 5(c)]. The dumbbell-shaped virtual sources and mixing vectors, especially the dumbbell-shaped virtual sources on the source plane are deformed and the fitting are not shown [see the third and fourth columns of Figs. 5(b) and 5(c)]. The results for the influence of background absorption uncertainty on the performance are summarized in Table 2.

Figures 7(a) and 7(b) show the case presented in Fig. 3 of Sec. 3.2 with 34 and 10 dB SNR due to background scattering
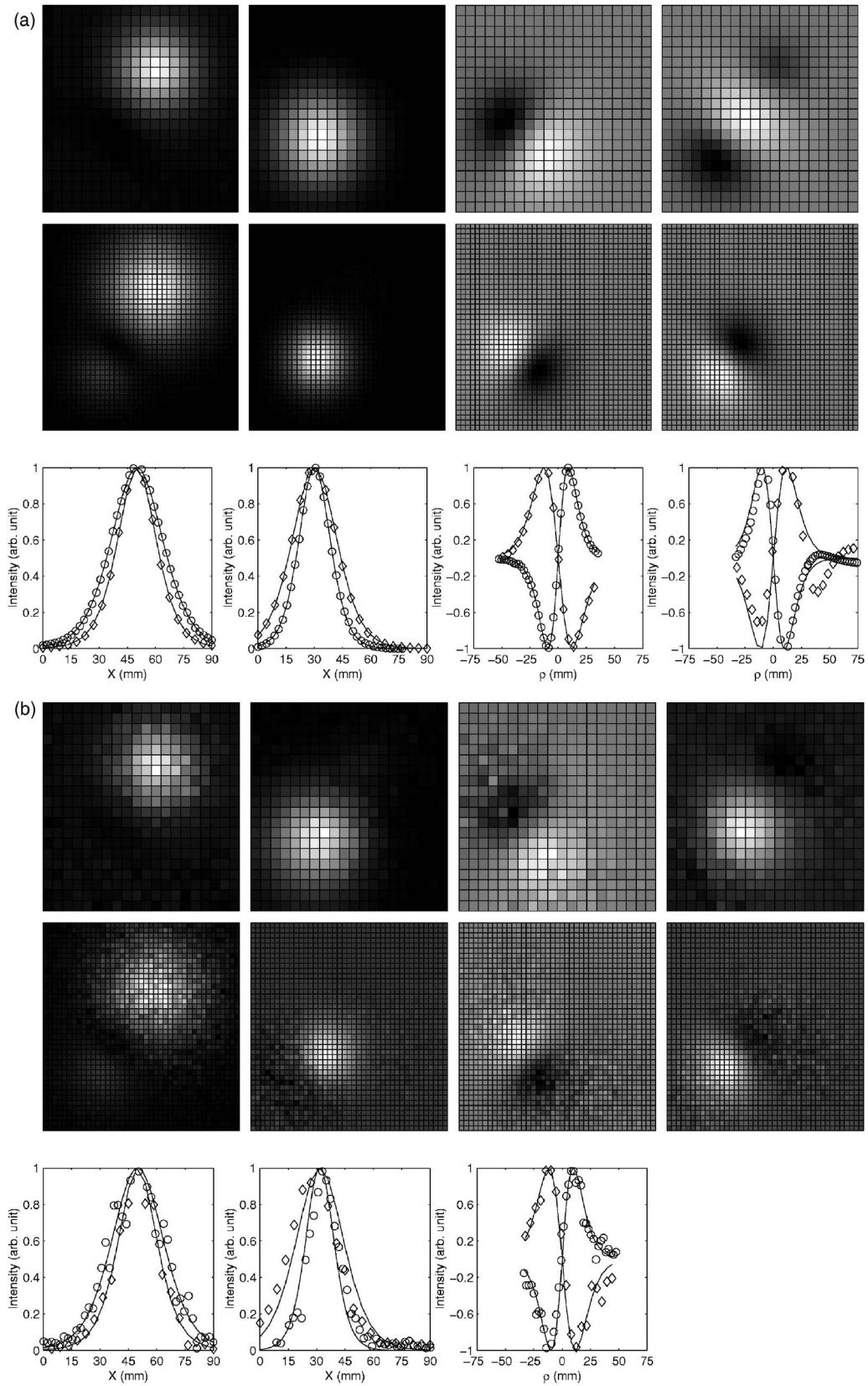
Fig. 7 Same as Fig. 3 with (a) 34 and (b) 10 dB background scattering uncertainty.

Table 3 Comparison of known and OPTICA determined positions and strengths of absorption (Abs) and scattering (Sca) inhomogeneities under different levels of background scattering uncertainty.

SNR (dB)	Target	Known Position (x, y, z) (mm)	Known Strength	Resolved Position (x, y, z) (mm)	Resolved Strength	Error in Position (mm)	Error in Strength (%)
34	Abs	(50, 60, 20)	0.01	(50.1, 60.3, 20.1)	0.0100	~0.3	~1
	Sca	(30, 30, 30)	−1	(30.0, 30.1, 30.0)	−0.99	~0.1	~1
10	Abs	(50, 60, 20)	0.01	(49.9, 60.5, 20.1)	0.0099	~0.5	~1
	Sca	(30, 30, 30)	−1	(31.7, 31.1, 32.5)	−0.75	~2.5	~25

uncertainty. The resolved absorptive inhomogeneity is at $(50.1, 60.3, 20.1)$ mm with strength 0.0100 at 34 dB SNR and at $(49.9, 60.5, 20.1)$ mm with strength 0.0099 at 10 dB SNR.

The resolved position and strength of the scattering object are found to be $(30.0, 30.1, 30.0)$ mm and $q_2 = -0.99$, $(32.2, 33.0, 30.0)$ mm and $q_2 = -0.96$, and $(32.3, 29.3, 27.1)$ mm and $q_2 = -1.08$, respectively, through fitting to the pair of centrosymmetric and two pairs of dumbbell-shaped virtual sources and mixing vectors [see the second to fourth columns of Fig. 5(a)], respectively, at 34 dB SNR. The resolved position and strength of the scattering object are found to be $(31.7, 31.1, 32.5)$ mm and $q_2 = -0.75$, $(30.9, 31.4, 27.5)$ mm and $q_2 = -1.08$, respectively, through fitting to the pair of centrosymmetric and the first pair of dumbbell-shaped virtual sources and mixing vectors [see the second to fourth columns of Fig. 5(b)] at 10 dB SNR. The results for the influence of background scattering uncertainty on the performance are summarized in Table 3.

The uncertainty in the background absorption or diffusion coefficients affects the performance of OPTICA in a similar fashion as the noise does discussed in Sec. 3.4. The error in localization and characterization of scattering inhomogeneities increases rapidly while the error in localization and characterization of absorptive inhomogeneities only increases mildly with the increase of the uncertainty in the background optical property. The uncertainty in background scattering has a less adverse effect on the performance of OPTICA than that in background absorption.

4 Discussion

The simulational study of OPTICA presented in this paper demonstrates its potential in optical imaging of objects in turbid media. It was shown to be able to locate and characterize absorptive and scattering inhomogeneities within highly scattering medium. In particular, OPTICA can discriminate between absorptive and scattering inhomogeneities and locate and characterize complex inhomogeneities, which is both absorptive and scattering. The accuracy of localization and characterization of inhomogeneities is high. In the cases investigated for concentrated inhomogeneities within a tissue-emulating slab of thickness of 50 mm, the errors in resolved object locations are not greater than 1 mm and the errors in the resolved optical strengths are ~2% under favorable noise levels and reliable background estimations.

Noise at higher levels and/or larger uncertainty in the optical property of the background medium makes it difficult to discriminate between absorptive and scattering inhomogeneities. In such a situation, other corroborative evidence, such as multiwavelength measurements, are required to determine the nature of inhomogeneities. Noise at higher levels and/or larger uncertainties in the optical property of the background medium also introduces larger errors in localization and characterization of scattering inhomogeneities. The accuracy of localization and characterization of absorptive inhomogeneities is only mildly affected by the amount of noise and/or uncertainty in the range investigated.

OPTICA unmixes inhomogeneities based on the mutual statistical independence between them and does not rely on a Gaussian distribution of light intensity on the surface of the embedding medium. OPTICA has several salient features. First, OPTICA provides the independent components due to the inhomogeneities with minimal processing of the data and does not have to resort to any specific light propagation model for obtaining this information. Specific light propagation models are needed only in the later stage to determine location and optical strength. Second, different geometries, or even an arbitrary shaped boundary, can be used with OPTICA. Although we used the slab geometry in the work reported in this paper, the approach does not depend on any specific geometry. Third, the approach is fast and is amenable to near real-time detection and localization of objects in a turbid medium, which is a key consideration for *in vivo* medical imaging.

As is well known, the diffusion approximation to RTE, which is widely used in inverse image reconstruction, does not apply when the separation between any two of the source, the inhomogeneity and the detector is small, or when there are clear regions in the medium. A special treatment is also required when the medium has aligned microstructures, such as myofibrils, axons, or collagen fibers in tissues.[43] The fact that a prior assumption of a specific model of light propagation in the medium is not assumed in the identification of independent components by ICA and is required only in a Green's function analysis of the retrieved independent component is desirable, especially in situations that demand a more complex model than the conventional DA. Performing the fitting procedure for each identified independent component is much simpler and more transparent than matching the measured light intensity to a forward model iteratively. The quality of reconstruction of OPTICA is expected to be higher than the

conventional approach when only an imperfect forward model is available.

OPTICA is most suited to detect small objects. Given its ability to identify low-contrast small objects, the approach is expected to be especially useful for detection of tumors at their early stages of development.

Acknowledgments

References

1. G. Muller, R. R. Alfano, S. R. Arridge, J. Beuthan, E. Gratton, M. Kaschke, B. R. Masters, S. Svanberg, and P. van der Zee, Eds., *Medical Optical Tomography: Functional Imaging and Monitoring*, Vol. IS11 of SPIE Institute Series, SPIE Press, Bellingham, WA (1993).

2. A. Yodh and B. Chance, "Spectroscopy and imaging with diffusing light," *Phys. Today* **48**, 38–40 (1995).

3. M. A. O'Leary, D. A. Boas, B. Chance, and A. G. Yodh, "Experimental images of heterogeneous turbid media by frequency-domain diffusing-photon tomography," *Opt. Lett.* **20**, 426–428 (1995).

4. S. K. Gayen and R. R. Alfano, "Emerging optical biomedical imaging techniques," *Opt. Photonics News* **7**, 17–22 (1996).

5. J. C. Hebden, S. R. Arridge, and D. T. Delpy, "Optical imaging in medicine: I. Experimental techniques," *Phys. Med. Biol.* **42**, 825–840 (1997).

6. S. R. Arridge and J. C. Hebden, "Optical imaging in medicine: II. Modelling and reconstruction," *Phys. Med. Biol.* **42**, 841–853 (1997), (eng).

7. W. Cai, S. K. Gayen, M. Xu, M. Zevallos, M. Alrubaiee, M. Lax, and R. R. Alfano, "Optical tomographic image reconstruction from ultrafast time-sliced transmission measurements," *Appl. Opt.* **38**, 4237–4246 (1999).

8. S. R. Arridge, "Optical tomography in medical imaging," *Inverse Probl.* **15**, R41–R93 (1999).

9. D. Grosenick, H. Wabnitz, H. H. Rinneberg, K. T. Moesta, and P. M. Schlag, "Development of a time-domain optical mammograph and first in vivo applications," *Appl. Opt.* **38**, 2927–2943 (1999).

10. V. Chernomordik, D. Hattery, A. H. Gandjbakhche, A. Pifferi, P. Taroni, A. Torricelli, G. Valentini, and R. Cubeddu, "Quantification by random walk of the optical parameters of nonlocalized abnormalities embedded within tissuelike phantoms," *Opt. Lett.* **25**, 951–953 (2000).

11. V. A. Markel and J. C. Schotland, "Inverse scattering for the diffusion equation with general boundary conditions," *Phys. Rev. E* **64**, 035601 (2001).

12. A. H. Hielscher and S. Bartel, "Use of penalty terms in gradient-based iterative reconstruction schemes for optical tomography," *J. Biomed. Opt.* **6**, 183–192 (2001).

13. M. Xu, M. Lax, and R. R. Alfano, "Time-resolved Fourier optical diffuse tomography," *J. Opt. Soc. Am. A* **18**, 1535–1542 (2001).

14. B. A. Brooksby, H. Dehghani, B. W. Pogue, and K. D. Paulsen, "Near-infrared (NIR) tomography breast image reconstruction with a priori structural information from MRI: algorithm development for reconstructing heterogeneities," *IEEE J. Sel. Top. Quantum Electron.* **9**, 199–209 (2003).

15. H. Dehghani, B. W. Pogue, S. P. Poplack, and K. D. Paulsen, "Multiwavelength three-dimensional near-infrared tomography of the breast: initial simulation, phantom, and clinical results," *Appl. Opt.* **42**, 135–145 (2003).

16. *Topics in Biomedical Optics*, J. C. Hebden, D. A. Boas, J. S. George, and A. J. Durkin, Eds., pp. 2869–3329, a special issue of *Appl. Opt.* **42** (2003).

17. W. Cai, M. Xu, and R. R. Alfano, "Three dimensional radiative transfer tomography for turbid media," *IEEE J. Sel. Top. Quantum Electron.* **9**, 189–198 (2003).

18. L. Wang, P. P. Ho, C. Liu, G. Zhang, and R. R. Alfano, "Ballistic 2-D imaging through scattering walls using an ultrafast optical Kerr gate," *Science* **253**, 769–771 (1991).

19. R. R. Alfano, X. Liang, L. Wang, and P. Ho, "Time-resolved imaging of translucent droplets in highly scattering media," *Science* **264**, 1913–1914 (1994).

20. W. Cai, M. Lax, and R. R. Alfano, "Analytical solution of the elastic Boltzmann transport equation in an infinite uniform medium using cumulant expansion," *J. Phys. Chem. B* **104**, 3996–4000 (2000).

21. W. Cai, M. Lax, and R. R. Alfano, "Analytical solution of the polarized photon transport equation in an infinite uniform medium using cumulant expansion," *Phys. Rev. E* **63**, 016606 (2000).

22. M. Xu, W. Cai, M. Lax, and R. R. Alfano, "Photon migration in turbid media using a cumulant approximation to radiative transfer," *Phys. Rev. E* **65**, 066609 (2002).

23. A. D. Klose and A. Hielscher, "Fluorescence tomography with simulated data based on the equation of radiative transfer," *Opt. Lett.* **28**, 1019–1021 (2003).

24. A. H. Gandjbakhche, G. H. Weiss, R. F. Bonner, and R. Nossal, "Photon path-length distributions for transmission through optically turbid slabs," *Phys. Rev. E* **48**, 810–818 (1993).

25. A. H. Gandjbakhche, V. Chernomordik, J. C. Hebden, and R. Nossal, "Time-dependent contrast functions for quantitative imaging in time-resolved transillumination experiments," *Appl. Opt.* **37**, 1973–1981 (1998).

26. A. N. Tikhonov and A. V. Groncharsky, Eds., *Ill-Posed Problems in the Natural Sciences*, MIR, Moscow (1987).

27. P. Comon, "Independent component analysis—a new concept?" *Signal Process.* **36**, 287–314 (1994).

28. A. J. Bell, "Information theory, independent component analysis, and applications," in *Unsupervised Adaptive Filtering*, Vol. I, S. Haykin, Ed., pp. 237–264, Wiley, New York (2000).

29. D. Nuzillard and J.-M. Nuzillard, "Application of blind source separation to 1-D and 2-D nuclear magnetic resonance spectroscopy," *IEEE Signal Process. Lett.* **5**, 209–211 (Aug. 1998).

30. R. Vigário, J. Särelä, V. Jousmäki, M. Hämäläinen, and E. Oja, "Independent component approach to the analysis of EEG and MEG recordings," *IEEE Trans. Biomed. Eng.* **47**, 589–593 (2000).

31. A. Hyvärinen, J. Karhunen, and E. Oja, *Independent Component Analysis*, Wiley, New York (2001).

32. J.-F. Cardoso, "Blind signal separation: statistical principles," *Proc. IEEE* **86**, 2009–2025 (1998).

33. A. Hyvärinen and E. Oja, "Independent component analysis: algorithms and applications," *Neural Networks* **13**, 411–430 (2000).

34. S. Chandrasekhar, *Radiative Transfer*, Dover, New York (1960).

35. M. Xu, W. Cai, M. Lax, and R. R. Alfano, "A photon transport forward model for imaging in turbid media," *Opt. Lett.* **26**, 1066–1068 (2001).

36. P. M. Morse and H. Feshbach, *Method of Theoretical Physics*, Vols. I and II, McGraw-Hill, New York (1953).

37. M. Lax, V. Nayaramamurti, and R. C. Fulton, "Classical diffusion photon transport in a slab," in *Laser Optics of Condensed Matter*, J. L. Birman, H. Z. Cummins, and A. A. Kaplyanskii, Eds., pp. 229–237, Plenum, New York (1987).

38. J. X. Zhu, D. J. Pine, and D. A. Weitz, "Internal reflection of diffusive light in random media," *Phys. Rev. A* **44**, 3948–3959 (1991).

39. R. C. Haskell, L. O. Svaasand, T.-T. Tsay, T.-C. Feng, M. S. McAdams, and B. J. Tromber, "Boundary conditions for the diffusion equation in radiative transfer," *J. Opt. Soc. Am. A* **11**, 2727–2741 (1994).

40. S. R. Arridge, "Photon-measurement density functions. Part I: Analytic forms," *Appl. Opt.* **34**, 7395–7409 (1995).

41. S. R. Arridge and M. Schweiger, "Photon-measurement density functions. Part 2: Finite-element-method calculations," *Appl. Opt.* **34**, 8026–8037 (1995).

42. H. Heusmann, J. Kölzer, and G. Mitic, "Characterization of female breasts *in vivo* by time resolved and spectroscopic measurements in near infrared spectroscopy," *J. Biomed. Opt.* **1**, 425–434 (1996).

43. J. Heino, S. Arridge, J. Sikora, and E. Somersalo, "Anisotropic effects in highly scattering media," *Phys. Rev. E* **68**, 031908 (2003).

Three-dimensional optical tomographic imaging of scattering objects in tissue-simulating turbid media using independent component analysis

M. Alrubaiee, M. Xu, S. K. Gayen, M. Brito, and R. R. Alfano[a)]
Institute for Ultrafast Spectroscopy and Lasers, Physics Department, The City College of New York and the Graduate School of the City University of New York, 138th Street at Convent Avenue, New York, New York 10031

An information-theory-based approach for the detection and three-dimensional localization of scattering targets embedded in a turbid medium, such as a tumor in the breast, is introduced. The approach uses multisource illumination of the medium, multidetector transillumination signal acquisition, and independent component analysis of the information theory for target detection and localization. The efficacy of the approach is demonstrated by detecting and obtaining location information about scattering targets embedded in human breast tissue-simulating turbid media of thickness 50 times the transport mean-free path. © *2005 American Institute of Physics*.
[DOI: 10.1063/1.2130547]

Detection and localization of scattering targets within a turbid medium is a challenging problem with diverse practical applications, such as imaging of a breast tumor, identification of mines in coastal water, and detection of an airplane, or, structures through cloud and fog cover. A recent study involving 35 319 patients underscores the influence of primary tumor location on breast cancer prognosis, and makes it imperative that breast cancer detection modalities obtain three dimensional (3D) location of the tumor relative to the axilla.[1] Optical detection of targets in a turbid medium makes use of the difference in optical properties, such as scattering coefficient, absorption coefficient, index of refraction, and fluorescence between the targets of interest and the intervening medium.[2] Multiple scattering of light by the turbid medium produces a noise background that deteriorates the contrast, blurs the image, and in severe cases makes direct transillumination imaging impossible. Inverse image reconstruction approaches that are commonly used to retrieve image information have to deal with the fact that inverse problems are ill posed, and attain different measures of success with $\sim$1 cm spatial resolution.[3]

This article introduces an alternative approach for detection and 3D localization of targets (optical inhomogeneities) embedded inside a highly scattering turbid medium. The approach makes use of transmitted light signal collected by multiple detectors following multiple-source illumination of the turbid medium containing the targets. The resulting multiple angular views provide robust data that is analyzed using the independent component analysis (ICA) (Ref. 4) of information theory to determine the locations of targets relative to the medium boundaries with millimeter accuracy. We refer to this optical domain application of ICA as OPTICA to distinguish it from other applications. While OPTICA may be used for the detection and localization of absorptive, scattering, and fluorescent targets, this letter focuses on scattering targets.

The perturbation in the light intensity distribution on the boundaries of the medium, the scattered wave field, due to scattering inhomogeneities is given by[5]

$$\phi_{\text{sca}}(\mathbf{r}_d,\mathbf{r}_s) = -\int d^3r\, \delta D(\mathbf{r}) c\nabla_r G(\mathbf{r}_d,\mathbf{r}) \cdot \nabla_r G(\mathbf{r},\mathbf{r}_s), \quad (1)$$

in the diffusion approximation (DA). Here, $\mathbf{r}_s$, $\mathbf{r}$, and $\mathbf{r}_d$ are the positions of the source, the inhomogeneity and the detector, respectively, $\delta D = D_{\text{obj}} - D$ is the difference between the diffusion coefficient of the object, D_{obj} and that of the medium, D, c is the speed of light in medium, and $G(\mathbf{r},\mathbf{r}_s)$ and $G(\mathbf{r},\mathbf{r}_d)$ are source-target and target-detector Green's functions, respectively. While the formalism, detailed elsewhere and tested for simulated data,[6] is applicable for different sample sizes and shapes, Green's functions for the slab geometry[7] are used here since rectangular slab samples were used in experiments.

Under the assumption that the scattering inhomogeneities are localized in a few regions within the turbid medium, Eq. (1) may be rewritten as

$$
\begin{aligned}
-\phi_{\text{sca}}(\mathbf{r}_d,\mathbf{r}_s) = &\sum_{j=1}^{n} g_z(\mathbf{r}_j,\mathbf{r}_d) q_j g_z(\mathbf{r}_j,\mathbf{r}_s) \\
&+ \sum_{j=1}^{n} \rho_{dj}\cos\theta_d g_\perp(\mathbf{r}_j,\mathbf{r}_d) q_j \rho_{sj}\cos\theta_s g_\perp(\mathbf{r}_j,\mathbf{r}_s) \\
&+ \sum_{j=1}^{n} \rho_{dj}\sin\theta_d g_\perp(\mathbf{r}_j,\mathbf{r}_d) q_j \rho_{sj}\sin\theta_s g_\perp(\mathbf{r}_j,\mathbf{r}_s),
\end{aligned}
$$
$$(2)$$

where $q_j = \delta D(\mathbf{r}_j)cV_j$ is the strength of the jth scattering inhomogeneity of volume, V_j located at $\mathbf{r}_j$, $\rho_{dj} = [(x_d - x_j)^2 + (y_d - y_j)^2]^{1/2}$, $\rho_{sj} = [(x_s - x_j)^2 + (y_s - y_j)^2]^{1/2}$, and θ_d and θ_s are the polar angles of $\mathbf{r}_d - \mathbf{r}_j$, and $\mathbf{r}_s - \mathbf{r}_j$, respectively, g_z, and $g_\perp$ are the longitudinal and transverse components of the Green's functions, and the summation is over all the inhomogeneities. The contribution to ϕ_{sca} from the jth inhomogeneity consists of three terms. These three terms may be interpreted as contributions from three "virtual sources" $q_j g_z(\mathbf{r}_j,\mathbf{r}_s)$, $q_j \rho_{sj}\cos\theta_s g_\perp(\mathbf{r}_j,\mathbf{r}_s)$, and $q_j \rho_{sj}\sin\theta_s g_\perp(\mathbf{r}_j,\mathbf{r}_s)$ weighted by $g_z(\mathbf{r}_j,\mathbf{r}_d)$, $\rho_{dj}\cos\theta_d g_\perp(\mathbf{r}_j,\mathbf{r}_d)$, and $\rho_{dj}\sin\theta_d g_\perp(\mathbf{r}_j,\mathbf{r}_d)$, respectively. The first virtual source, $q_j g_z(\mathbf{r}_j,\mathbf{r}_s)$ is centrosymmetric, the other two are dumbbell
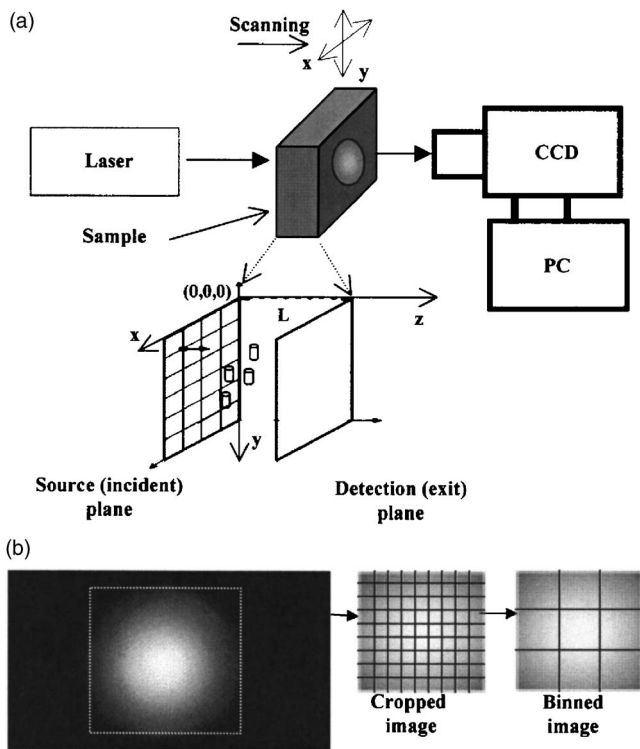
(a)

(b)

FIG. 1. (a) A schematic diagram of the experimental arrangement. Inset shows a 2D array of horizontal and vertical points in the input plane that are scanned across the laser beam. (b) A typical raw image recorded by the CCD, and how it is cropped and binned for analysis.

shaped and orthogonal to each other. The centrosymmetric virtual source makes the dominant contribution to ϕ_{sca}, compared to the other two. The detected fraction of ϕ_{sca} on the exit plane (also referred to as the detection plane) of the sample is a weighted linear mixture of contributions from $3n$ virtual sources, if there are n scattering targets within the medium. All virtual sources are assumed to be statistically independent.

Independent component analysis of the measured ϕ_{sca} can then retrieve the "virtual sources" and corresponding weighting matrices.[6] The contribution of each target to ϕ_{sca} on the detection plane (and also on the source plane) can be obtained as a two-dimensional (2D) independent intensity distribution (IID). IID due to a target may be looked upon as the light intensity pattern that a source located at the target position would generate on the detection (or source) plane. The 3D location of the target relative to sample boundaries is estimated from fits of these OPTICA generated IID to the model Green's functions.

The experimental arrangement for demonstrating the efficacy of OPTICA is shown schematically in Fig. 1. Continuous-wave 784 nm radiation from a diode laser delivered by a 200-μm-optical fiber was used for illuminating the

entrance face (henceforth referred to as the "source plane") of the slab sample. Multiple source illumination was realized in practice by step scanning the slab sample along the horizontal (x) and vertical (y) directions across the laser beam. A camera lens collected the diffusely transmitted light on the opposite face of the slab (henceforth referred to as the "detection plane") sample and projected it onto the sensing element of a cooled charged couple device (CCD) camera. Each illuminated pixel of the 1024 × 1024 pixels of the CCD camera could be regarded as a detector. For illumination of every scanned point on the source plane, the CCD camera recorded the diffusely transmitted intensity pattern on the detection plane.

Two different samples were used in the experiments reported here. The first sample was a 250 mm × 250 mm × 50 mm transparent plastic cell filled with Intralipid-10% suspension in water. The concentration of Intralipid-10% was adjusted to provide a transport length ℓ_t of ~2 mm at 784 nm. A ~9-mm-diameter glass sphere filled with a suspension of 0.707 μm diameter polystyrene spheres in water was the scattering target. The microspheres do not absorb 784 nm light, and their concentration was adjusted to provide a scattering length, ℓ_s of ~0.0188 mm, transport length ℓ_t of ~0.133 mm, and anisotropy factor, g ~ 0.858. The location of the center of the target was (25 mm, 25 mm, 21 mm) with respect to the front upper left corner of the sample cell [see inset of Fig. 1(a)]. This sample was used to test the predictions of the theoretical formalism.

The second sample was a 166-mm-long, 82-mm-wide, and 55-mm thick scattering slab cast from a suspension of titanium dioxide particles and a near-infrared dye in epoxy resin containing four cylindrical scattering targets.[8] The slab material had an optical transport length of ~1.1 mm, and absorption coefficient of 0.006 mm^{-1}. Each of the four cylinders had a length of 5 mm, a diameter of 5 mm, absorption coefficient equal to that of the slab material, and scattering coefficients 4, 2, 1.5, and 1.1 times higher than that of the slab. The center of each cylinder was located in the plane halfway between the front and back surfaces of the slab, and their known coordinates are presented in Column 3 of Table I. The second sample was used to test the efficacy of OPTICA on a breast-simulating specimen. Sample 1 was scanned in an x-y array of 21 × 21 grid points with a step size of 2.5 mm across the laser beam, while Sample 2 was scanned in a 20 × 18 array of same step size.

Figure 1(b) presents a typical 2D raw image of the detection plane recorded by the CCD camera for illumination of a grid point in the source plane. Similar 2D raw images are recorded for every scanned grid point on the source plane. As Fig. 1(b) further shows, each raw image is then cropped to select out the information-rich region, and binned to enhance the signal-to-noise ratio. All the binned images are then added and an average image (henceforth, referred to

TABLE I. Comparison of the known and OPTICA determined positions of the targets in Sample 2.

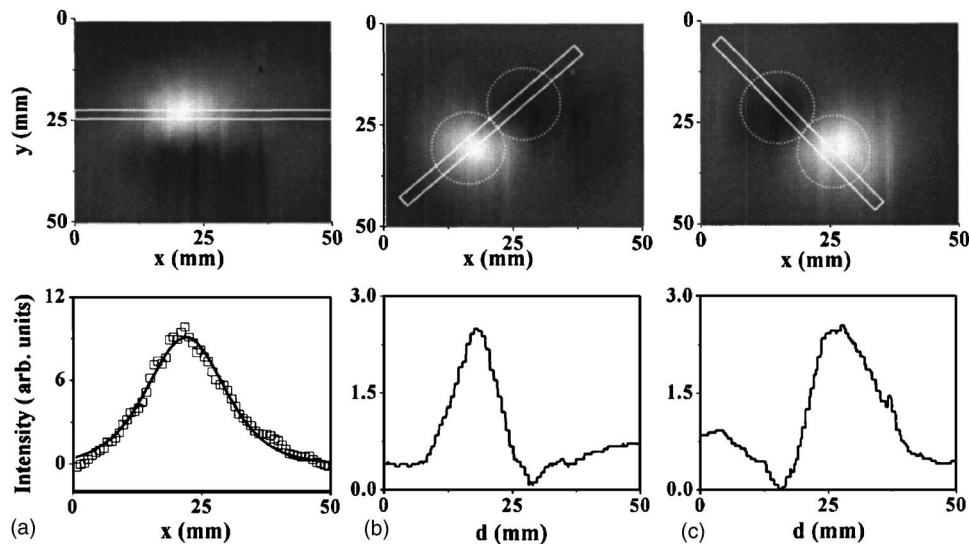| Target No.	$\mu_{s,target}/\mu_{s,slab}$	Known position (x, y, z) mm	Observed position (x, y, z) mm	Error $(\Delta x, \Delta y, \Delta z)$
1	4	(60, 60, 27.5)	(62, 63, 28.1)	(2, 3, 0.6)
2	2	(47, 30, 27.5)	(48, 33, 28.9)	(1, 3, 1.4)
3	1.5	(33, 60, 27.5)	(33, 62, 27.1)	(0, 2, 0.4)
4	1.1	(20, 30, 27.5)	(18, 33, 32.6)	(2, 3, 5.1)

FIG. 2. Independent 2D spatial intensity distributions at the detection plane of the scattering sphere in Sample 1 generated by OPTICA: (a) The centrosymmetric component. (b) and (c) the dumbbell shaped components. The white dotted circles in the images presented in (b) and (c) are provided as guide for the eyes to show the high intensity and low intensity areas of the dumbbell. The white rectangles in the images are the regions that are integrated over to generate the spatial profiles. In the lower frame of (a), the solid line represents a Green's function fit to the experimental data represented by open squares.

as the "reference image") is generated to serve as the background. The difference between the reference image and the mth binned image is proportional to the perturbation in light intensity distribution on the detection plane, $\phi_{sca,m}$ for illumination of the mth grid point. All the $\phi_{sca,m}$'s are then stacked, and used as input for independent component analysis.

OPTICA generated 2D independent intensity distributions (IIDs) at the detection plane for the single scattering target in Sample 1 are presented in the upper frames of Figs. 2(a)–2(c). The corresponding spatial intensity profiles integrated over the areas enclosed by white dashed boxes appear in the lower frames. As predicted by the theoretical formalism, three intensity distributions from three virtual sources corresponding to the single scattering target are observed. The spatial intensity profile of Fig. 2(a) is symmetric about the vertical centerline (centrosymmetric), the profile of Fig. 2(b) has a peak followed by a dip, and that of Fig. 2(c) has a dip followed by a peak, and resemble the predicted dumbbell shape. The location of the target determined from the Green's function fit of the intensity distribution is (23 mm, 25 mm, 22 mm) which agrees well with the known position of (25 mm, 25 mm, 21 mm). The relative peak intensity of the centrosymmetric component is approximately four times larger than that of the dumbbells. For more highly scattering samples and with a decrease in the signal-to-noise ratio, the dumbbell-shaped components get much reduced in intensity, and may not be observable. It should be mentioned that an absorptive target generates only a centrosymmetric IID.

The results of OPTICA measurements on Sample 2 are summarized in Table I, that compares the known locations of all 4 targets with those obtained from this approach. Except for Target No. 4, coordinates of other targets are obtained within 0–3 mm (a standard deviation of ~2 mm) of the respective known positions. The larger error in the estimated location of Target No. 4 may be due to its low contrast and

hence higher susceptibility to noise. Overall, the errors in location estimates are smaller than the target dimensions even for a breast-simulating scattering medium.

What is remarkable about the OPTICA approach is that even at this initial stage of development it could detect and locate all four scattering targets, including the weakest target with a scattering coefficient just 1.1 times the background and hence was considered to be "rather unlikely to be found."[8] For highly scattering medium (such as Sample No. 2), only the centrosymmetric virtual sources corresponding to scattering targets could be observed. Additional information, such as measurements at different wavelengths are needed for identification of the target as a scatterer or an absorber. Although the DA was used in this case, OPTICA does not depend on any specific light propagation model, and can be used with other models. This feature makes OPTICA a more general approach applicable for a variety of scattering media where DA may not hold. OPTICA is suited for detection of small inhomogeneities on mm scale, and has the potential for detection and localization of tumors in the breast at early stages of growth.

[1]N. Kroman, J. Wohlfahrt, H. T. Mouridsen, and M. Melbye, Int. J. Cancer **105**, 542 (2003).
[2]S. K. Gayen and R. R. Alfano, Opt. Photonics News **7**, 22 (1996).
[3]S. R. Arridge, Inverse Probl. **15**, R41 (1999).
[4]P. Comon, Signal Process. **36**, 287 (1994).
[5]M. Xu, M. Lax, and R. R. Alfano, J. Opt. Soc. Am. A **18**, 1535 (2001).
[6]M. Xu, M. Alrubaiee, S. K. Gayen, and R. R. Alfano, J. Biomed. Opt. **10**, 051705 (2005).
[7]M. Lax, V. Narayanamurti, and R. C. Fulton, in *Laser Optics of Condensed Matter*, edited by J. L. Birman, H. Z. Cummins, and A. A. Kaplyanskii (Plenum, New York, 1987), pp. 229–237.
[8]D. J. Hall, J. C. Hebden, and D. T. Delpy, Appl. Opt. **36**, 7270 (1997).

Fluorescence optical tomography using independent component analysis to detect small targets in turbid media

M. Alrubaiee, M. Xu, S. K. Gayen, and R. R. Alfano

Institute for Ultrafast Spectroscopy and Lasers, Physics Department

The City College of New York, 138th Street at Convent Avenue, New York, NY 10031

ABSTRACT

A new approach for optical fluorescence tomographic imaging of targets in a turbid medium that uses the independent component analysis (ICA) from information theory is presented. Fluorescence signals from targets embedded in a turbid medium are measured on the boundary of the medium using a multi-source excitation and a multi-detector acquisition scheme. Differences between excitation and fluorescence wavelengths enable sensitive, minimal-background signal acquisition. ICA of the fluorescence signal on the medium boundary sorts out the embedded objects, and their locations are obtained from Green's function analysis based on any appropriate light propagation model. Fluorescence tomographic imaging experiments were carried out using Intralipid-10% suspension in water contained in a 50-mm thick rectangular transparent plastic cell as the turbid medium, and small glass spheres containing indocyanine green (ICG) solution as fluorescent targets. The near-infrared (NIR) fluorescence was excited using 785 nm light, and monitored over a narrow band around 830 nm. The transport mean free paths at 785 nm and 830 nm were 1.01 mm and 1.14 mm, respectively. The approach could image and determine the position of an ICG filled sphere of radius as small as 4 mm. It is applicable to small objects, different medium geometries, and amenable to near real time imaging applications.

Keyword: Near-infrared fluorescence imaging, imaging through turbid media, tissue-like phantom, inverse image reconstruction, independent component analysis.

1. INTRODUCTION

The advent of novel fluorescence beacons and contrast agents with ability to attach themselves to a desired large cluster of abnormal cells or organelles,[1] and fluoresce when excited with light of appropriate wavelength make fluorescence tomography attractive for detection and diagnosis of tumors in human body organs, such as, breast and prostate. Direct imaging approaches fail to provide accurate location of fluorescent targets embedded in a turbid medium[2,3] Researchers then resort to tomographic image reconstruction (TIR) schemes that use fluorescence signals measured from the surface of the specimen, an appropriate model for light propagation, and numerical algorithms to reconstruct fluorescent target(s) inside the specimen.[4-9]

We introduce a novel optical tomography approach that uses independent components analysis[10,11] of information theory to analyze the fluorescence signal excited by a multi-source illumination scheme and measured by a multi-detector signal acquisition arrangement providing a variety of spatial and angular views essential for three-dimensional (3D) localization and characterization of the target. We refer to this approach as fluorescence OPTICA.

2. THEORY

Fluorescence tomography requires accounting for propagation of excitation light beams that induce fluorescence from embedded targets, and that of the fluorescence emitted by the localized targets to the detectors. In fluorescence OPTICA, the incident light at wavelength λ_x propagates from the source point r_s at the input (or, source) plane to the target located at position r inside the medium. Fluorescence at wavelength λ_m propagates from target at r to the detector at r_d. The propagation of excitation and fluorescent light beams is described by coupled diffusion equations at the excitation and emission wavelengths.[8,9]

The fluorescence signal $U_m(r_d, r_s, \omega)$ can be expressed in terms of the two Green's functions $G_x(r, r_s, \omega)$ and $G_m(r_d, r, \omega)$ describing light propagation from the source at r_s to the target at r at the excitation wavelength λ_x and the light propagation from the target to the detector at r_d at the emission wavelength λ_m. The subscripts x and m refer to the

quantities associated with the excitation and emission wavelengths, respectively. Assuming the jth fluorescent target is contained in volume V_j centered at $\mathbf{r}_j$, the fluorescence signal under illumination by a unit point source at $\mathbf{r}_s$ is given by

$$U_m(\mathbf{r}_d, \mathbf{r}_s, \omega) = \sum_{j=1}^{J} G_m(\mathbf{r}_d, \mathbf{r}_j, \omega) f_j(\omega) G_x(\mathbf{r}_j, \mathbf{r}_s, \omega) \tag{1}$$

where $f_j(\omega) = \gamma(\mathbf{r}_j) c V_j / [1 - i\omega\tau(\mathbf{r}_j)]$ represents the fluorescence strength of the jth inhomogeneity, γ is the fluorescent yield, and τ is the fluorescence lifetime. The contribution of jth source, $f_j G_x(\mathbf{r}_j, \mathbf{r}_s, \omega)$ is weighted by a mixing vector $G_m(\mathbf{r}_d, \mathbf{r}_j, \omega)$ and all the weighted sources are mixed to produce the detected signal $U_m(\mathbf{r}_d, \mathbf{r}_s, \omega)$. ICA assumes that the signals from the fluorescent targets are statistically independent, and that the measured signal is a weighted mixture of contributions from these independent sources.[10,11] By seeking the maximal mutual independence, both fluorescent sources and mixing vectors can be obtained by independent component analysis of the multi-source multi-detector data set $U_m(\mathbf{r}_d, \mathbf{r}_s, \omega)$.

3. EXPERIMENTAL ARRANGEMENT

Figure 1 shows schematically the experimental setup used for testing the fluorescence OPTICA approach. The turbid used in the experiment was Intralipid-10% suspension in water contained in a 250 mm x 250 mm x 50 mm transparent plastic cell. The concentration of Intralipid-10% was adjusted to provide a transport length $l_t \sim 1$mm at 785 nm. The fluorescent target consists of glass sphere with a hook attached to a white thin string as shown in Fig. 2(a). The sphere is filled with a solution of Indocyanine green (ICG) dye in water. The absorption coefficient of the ICG solution at 785 nm is 11.5 mm^{-1}. To test how small an object could be observed, we used three different spheres with diameters 12 mm, 9 mm and 4 mm in turn. A 785-nm continuous wave (CW) laser beam was delivered through a $\sim$200-μm diameter optical fiber and focused to a $\sim$1 mm spot onto the input surface of the sample cell. A computer-controlled translation stage scanned the sample in a set of 10 x 10 grid points (step size = 2.5-mm), in the x-y plane perpendicular to the incident beam realizing a multi-source illumination scheme. For illumination at everyone of these points a 1024 x 1024 pixels cooled charge couple device (CCD) camera acquired a 2-D fluorescence image of the exit surface (opposite to the input surface) of the cell. The fluorescence spectrum of ICG in water, when excited at 785-nm, spans the wavelength range of 790-966 nm as shown in the inset of Fig. 1. We used a narrow-band filter centered at 830-nm to acquire a fraction of the fluorescence, and discriminate against the much more intense laser excitation beam. The images were stored in a personal computer for subsequent analysis by the numerical algorithm of fluorescence OPTICA.

Fig.1 A schematic diagram of the experimental arrangement for fluorescence OPTICA. The inset shows the fluorescence spectrum of ICG solution in water

4. RESULTS

A typical 2-D fluorescence image of the exit surface of the turbid medium recorded by the CCD camera is shown in Figure 2(b). The fluorescent target in this case was the 4-mm diameter sphere. Independent components analysis used the set of 100 images to generate independent intensity distribution on source and detector planes, as shown in Figures 2(c) and 2(d), respectively. The Green's function (solid line) fit to these intensity distributions represented by squares for the source plane and by circles for the detector plane are shown in Figures 3(a) and 3(b), respectively. The x-y-z co-ordinates of the fluorescence target were estimated to be approximately, $x = 15$ mm, $y = 15$ mm, and $z = 16$ mm, which are in excellent agreement with the known location of $x = 15$ mm, $y = 15$ mm, and $z = 15$ mm. This result is for the smallest of the spheres, and hence the most difficult of the three cases. The locations of the other two spheres were readily observed using the fluorescence OPTICA.
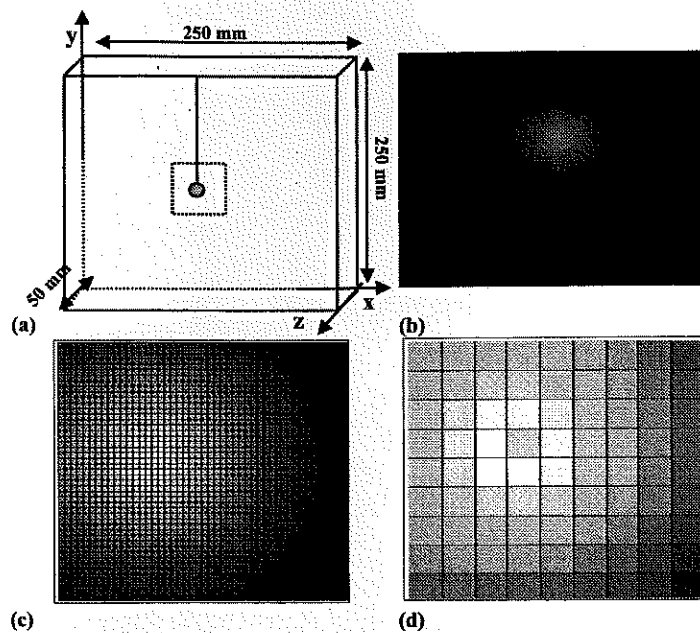
Fig. 2. (a) A schematic diagram showing the positions of fluorescence sphere filled with ICG in the Intralipid-10% suspension, (b) Fluorescence image at 830-nm. Independent spatial intensity distributions (independent components) in (c) the entrance, and (d) exit plane of the specimen.
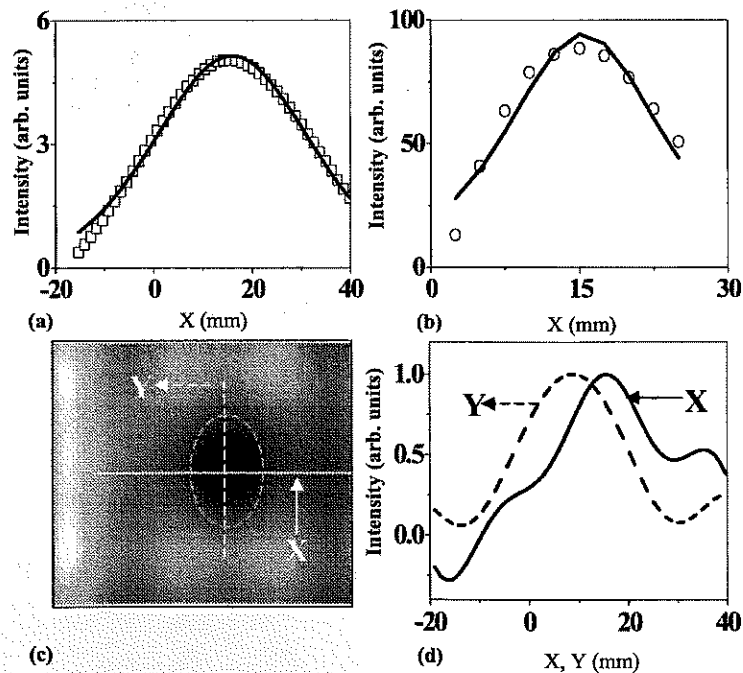
The shape of the 4-mm diameter object was reconstructed by using back-projection Fourier transforms. Figure 3(c) shows the projection onto the x-y plane, and Figure 3(d) shows the corresponding spatial intensity profiles. The full width half maximum (FWHM) of the profile in the x-direction is ~16-mm, while that in the y-direction is 18 mm. We attribute this change in shape and size to the projection of the hook being superimposed onto that of the sphere. This artifact was much reduced for the 12-mm diameter sphere where the shape of the hook could be distinguished, and the FWHM of the profiles were only 14 mm, much closer to the actual value.

5. DISCUSSION

Fig. 3 (a)-(b) Green's functions (solid line) fits to Independent spatial intensity (circle) from Fig. 2 (c)-(d) respectively. (c)-(d) Shape reconstructed using back-projection Fourier transform with corresponding spatial intensity profile

The approach presented in this article effectively used a multiple source excitation (realized through scanning of the sample in the x-y plane) and multiple detectors (each pixel on the CCD may be viewed as a detector) for data acquisition providing sufficient data for extracting useful location information about the fluorescent target. While OPTICA can be used for locating absorptive and scattering targets as well,[12] the advantage for the fluorescent target is that the background light can be minimized by use of appropriate filters, making it a 'zero-background' measurement, as opposed to the situations involving absorptive and scattering targets when changes in high light levels are measured. The 3-D localization of the object is achieved with a high accuracy, and shorter computation time compared to other commonly used methods for 3-D inverse image reconstruction. The ability to discern the ~4-mm diameter ICG sphere demonstrate the potential to detect breast tumors in early stage of growth when the treatment is most effective.

ACKNOWLEDGEMENTS

REFERENCES

1. Sanjay Tyagi, Salvatore A.E. Marras, Fred Russell Kramer, "Wavelength-shifting molecular beacons", *Nature Biotechnology* **18**, 1191 (2000).
2. Alexander D. Klose, AndreasH. Hielscher, "Fluorescence tomography with simulated data based on the equation of radiative transfer" *Opt. Lett.* **28**,1019 (2003).
3. M. A. O'Leary, D. A. Boas, X. D. Li, B. Chance, A. G. Yodh, "Fluorescence lifetime imaging in turbid media", *Opt. Lett.* **21**,158 (1996).
4. W. Cai, S. K. Gayen, M. Xu, M. Zevallos, M. Alrubaiee, M. Lax, R. R. Alfano "Optical tomographic image reconstruction from ultrafast time-sliced transmission measurements," *Appl. Opt.* **38**, 4237 (1999).
5. V. Ntziachristos, "Experimental three-dimensional fluorescence reconstruction of diffuse media by use of a normalized Born approximation", *Opt. Lett.* **26**, 893 (2001).
6. S. R. Arridge, "Optical tomography in medical imaging," *Inverse Probl.* **15**, R41 (1999).
7. A. D. Kim, "Optical Diffusion of Continuous-Wave, Pulsed, and Density Waves in Scattering Media and Comparisons with Radiative Transfer", *Appl. Opt.* **37**, 5313 (1998)
8. M. S. Patterson and B. W. Pogue, "Mathematical model for time-resolved and frequency-domain fluorescence spectroscopy in biological tissues," *Appl. Opt.* **33**, 1963 (1994).
9. A. B. Milstein, S. Oh, K. J. Webb, C. A. Bouman, Q. Zhang, D. A. Boas, and R. P. Millane, "Fluorescence optical diffusion tomography," *Appl. Opt.* **42**, 3081 (2003).
10. P. Comon, *Signal-Processing* **36**, 287-104 (1994).
11. J. -F. Cardoso, "Blind signal separation: statistical principle," Proceedings of the IEEE **9**, 2009 (1998).
12. M. Alrubaiee, M. Xu, S. K. Gayen, W. Cai, and R. R. Alfano, "Time-resolved and quasi-continuous wave three-dimensional tomographic imaging of objects in tissue-like turbid media" Proceedings of SPIE Vol. **5463**, 82-85 (2004).

Optical tomography using independent component analysis to detect absorptive, scattering, or fluorescent inhomogeneities in turbid media

M. Xu, M. Alrubaiee, S. K. Gayen and R. R. Alfano

Institute for Ultrafast Spectroscopy and Lasers,
New York State Center of Advanced Technology for Ultrafast Photonic Materials and Applications,
and Department of Physics,
The City College and Graduate Center of City University of New York, New York, NY 10031

ABSTRACT

A new imaging approach for three-dimensional localization and characterization of absorptive, scattering or fluorescent objects in a turbid medium is presented and demonstrated using simulated and experimental data. This approach uses a multi-source and multi-detector signal acquisition scheme and independent component analysis (ICA) from information theory for target localization and characterization. Independent component analysis of the perturbation in the spatial intensity distribution or the fluorescent signal measured on the medium boundary sorts out the embedded objects. The location and optical characteristics (size, shape and optical property) of the embedded objects are obtained from a Green's function analysis based on an appropriate model for light propagation in the background medium and back-projections of the retrieved independent components.

Keywords: optical imaging, independent component analysis, absorption, scattering, fluorescence

1. INTRODUCTION

Optical probing of the interior of highly scattering colloidal suspensions and biological materials has attracted much attention over the last decade. In particular, biomedical optical tomography and spectroscopy using near infrared (NIR) light has been actively pursued to provide, for example, functional information about brain activities and diagnostic information about breast tumor because NIR light can penetrate deep into tissues and is sensitive to certain physiological parameters such as hemoglobin concentration and blood flow.[1-7] Both endogenous contrasts such as increased hemoglobin absorbance, and exogenous contrasts such as fluorescence agents have been studied for the purpose of medical diagnostics and prognostic measure.

Most works[4, 8-10] in imaging of endogenous or exogenous contrasts in turbid media adopt an inverse problem formalism based on the diffusion approximation or radiative transfer of light propagation in highly scattering media. A map of the spatial distribution of the endogenous contrast inside the medium is reconstructed by matching the detected light intensity change due to the contrast to that calculated by a forward model for light propagation in that medium. A map of the spatial distribution of the exogenous contrast is reconstructed, in a similar fashion, by matching the detected fluorescence to that calculated by a forward model for the propagation of the fluorescence light excited by an incident light beam in that medium. The commonly used forward models include the radiative transfer equation (RTE),[7, 10] the diffusion approximation (DA) of RTE,[4] and random walk of photons.[11]

Further author information: (Send correspondence to M. X.)
M. X.: Email: minxu@sci.ccny.cuny.edu

In this paper, we present an alternative approach using independent component analysis (ICA) of information theory to detect absorptive, scattering, or fluorescent inhomogeneities within tissue-like turbid media. We use a multi-source multi-detector scheme of data acquisition where light intensities are measured on the boundary of the medium by a two dimensional detector array when an external point source scans on the other side of the medium. The recorded data set (after removal of background signal in imaging of absorption or scattering contrasts) provides a set of observations made in multiple channels (detectors) from virtual sources (the inhomogeneities illuminated by the incident wave) over multiple discrete sampling points (the source scanning positions). Absorptive, scattering or fluorescent inhomogeneities appear as statistically independent virtual sources. These virtual sources are recovered by independent component analysis of the data set and sorts out the inhomogeneities. The location and characterization (size, shape and optical property) of inhomogeneities are obtained from a Green's function analysis based on any appropriate model of light propagation in the background medium and back-projections of the retrieved independent components. This approach is best suited for small inhomogeneities.

We refer to this information theory-inspired approach as optical imaging using independent component analysis, abbreviated as, OPTICA. ICA has been successfully applied in various other applications such as electroencephalogram and nuclear magnetic resonance spectroscopy.[12-15] The novelty of OPTICA over other ICA applications is that OPTICA associates directly the independent components to the Green's functions responsible for light propagation in the turbid medium from the inhomogeneities to the source and the detector, and therefore the retrieved independent components can be used to locate and characterize the inhomogeneities.

2. THEORY

2.1. Absorptive and scattering inhomogeneities

Absorptive and scattering inhomogeneities within a turbid medium alter the propagation of light through the medium. The alteration of the spatial distribution of the light intensity on the boundary of the medium depends on two Green's functions (propagators) $G(\mathbf{r}, \mathbf{r}_s, \omega)$ and $G(\mathbf{r}_d, \mathbf{r}, \omega)$ describing light propagation from the source at $\mathbf{r}_s$ to the inhomogeneity at $\mathbf{r}$ and from the inhomogeneity to the detector at $\mathbf{r}_d$, respectively, where ω is the modulation frequency of light.

In a parallel geometry, the scattered wave due to the presence of J absorptive inhomogeneities and J scattering inhomogeneities can be written as[16]

$$
\begin{aligned}
-\phi_{\text{sca}}(\mathbf{r}_d, \mathbf{r}_s, \omega) = & \sum_{j=1}^{J} G(\mathbf{r}_d, \mathbf{r}_j, \omega) q_j G(\mathbf{r}_j, \mathbf{r}_s, \omega) + \sum_{j=1}^{J'} g_z(\mathbf{r}_j, \mathbf{r}_d, \omega) q_j' g_z(\mathbf{r}_j, \mathbf{r}_s, \omega) \\
& + \sum_{j=1}^{J'} \rho_{dj} \cos\theta_d g_{\perp}(\mathbf{r}_j, \mathbf{r}_d, \omega) q_j' \rho_{sj} \cos\theta_s g_{\perp}(\mathbf{r}_j, \mathbf{r}_s, \omega) \\
& + \sum_{j=1}^{J'} \rho_{dj} \sin\theta_d g_{\perp}(\mathbf{r}_j, \mathbf{r}_d, \omega) q_j' \rho_{sj} \sin\theta_s g_{\perp}(\mathbf{r}_j, \mathbf{r}_s, \omega)
\end{aligned}
\tag{1}
$$

where $q_j = \delta\mu_a(\mathbf{r}_j) c V_j$ is the absorption strength of the jth inhomogeneity of volume V_j, $q_j' = \delta D(\mathbf{r}_j) c V_j'$ is the diffusion strength of the jth scattering inhomogeneity of volume V_j', $\delta\mu_a$ and δD are the deviation of the absorption and diffusion coefficients of the inhomogeneity from that of the background medium respectively, c is the speed of light in the background medium, $\rho_{dj} = \sqrt{(x_d - x_j)^2 + (y_d - y_j)^2}$ and $\rho_{sj} = \sqrt{(x_s - x_j)^2 + (y_s - y_j)^2}$ are the projections of $\mathbf{r}_d - \mathbf{r}_j$ and $\mathbf{r}_s - \mathbf{r}_j$ on the xy plane, respectively, and θ_d and

θ_s are the azimuthal angles of $\mathbf{r}_d - \mathbf{r}_j$ and $\mathbf{r}_s - \mathbf{r}_j$, respectively. The expressions of the Green's function G and the two auxiliary functions g_z and $g_\perp$ depend on the light propagation model in the background medium.[16]

In OPTICA, the absorptive or scattering inhomogeneities illuminated by the incident wave are assumed to be *virtual sources*, and the perturbation of the spatial distribution of the light intensity on the boundary described by Eq. (1) may be considered to be a linear mixture of signals arriving from these virtual sources. One absorptive inhomogeneity is represented by one virtual source $q_j G(\mathbf{r}_j, \mathbf{r}_s)$ with a mixing vector $G(\mathbf{r}_d, \mathbf{r}_j)$. One scattering inhomogeneity is represented by three virtual sources:

$$q'_j g_z(\mathbf{r}_j, \mathbf{r}_s), \quad q'_j \rho_{sj} \cos\theta_s g_\perp(\mathbf{r}_j, \mathbf{r}_s), \quad q'_j \rho_{sj} \sin\theta_s g_\perp(\mathbf{r}_j, \mathbf{r}_s), \tag{2}$$

with mixing vectors

$$g_z(\mathbf{r}_j, \mathbf{r}_d), \quad \rho_{dj} \cos\theta_d g_\perp(\mathbf{r}_j, \mathbf{r}_d), \quad \rho_{dj} \sin\theta_d g_\perp(\mathbf{r}_j, \mathbf{r}_d) \tag{3}$$

respectively.

Owing to the statistical independence between virtual sources, independent component analysis of the recorded data set can identify prominent independent components. Each independent component consists of one virtual source and its corresponding weighting vector. The number of leading independent components is same as the number of inhomogeneities. The details of the theoretical formalism of OPTICA for absorption or scattering inhomogeneities were presented elsewhere.[16]

2.2. Fluorescent inhomogeneities

Light propagation in a highly scattering medium with fluorescent targets excited by an external source is approximately described by coupled diffusion equations at the excitation and emission wavelengths.[8, 9] The fluorescence signal $U_m(\mathbf{r}_d, \mathbf{r}_s, \omega)$ can be expressed in terms of the two Green's functions $G_x(\mathbf{r}, \mathbf{r}_s, \omega)$ and $G_m(\mathbf{r}_d, \mathbf{r}, \omega)$ describing light propagation from the source at $\mathbf{r}_s$ to the target at $\mathbf{r}$ at the excitation wavelength λ_x and the light propagation from the target to the detector at $\mathbf{r}_d$ at the emission wavelength λ_m. The subscripts x and m refer to the quantities associated with the excitation and emission wavelengths, respectively.

Assuming the jth fluorophores is contained in volume V_j centered at $\mathbf{r}_j$, the fluorescence signal under illumination by a unit point source at $\mathbf{r}_s$ is given by

$$U_m(\mathbf{r}_d, \mathbf{r}_s, \omega) = \sum_{j=1}^{J} G_m(\mathbf{r}_d, \mathbf{r}_j, \omega) f_j(\omega) G_x(\mathbf{r}_j, \mathbf{r}_s, \omega) \tag{4}$$

where $f_j(\omega) = \gamma(\mathbf{r}_j) c V_j / [1 - i\omega\tau(\mathbf{r}_j)]$ represents the fluorescence strength of the jth inhomogeneity, γ is the fluorescent yield, and τ is the fluorescence lifetime.

Eq. (4) takes exactly the same form of the scattered wave Eq. (1) for absorptive inhomogeneities only (setting $q'_j = 0$ in Eq. (1)). The jth virtual source $f_j G_x(\mathbf{r}_j, \mathbf{r}_s, \omega)$ is weighted by a mixing vector $G_m(\mathbf{r}_d, \mathbf{r}_j, \omega)$ and all the weighted virtual sources are mixed to produce the detected signal $U_m(\mathbf{r}_d, \mathbf{r}_s, \omega)$. By seeking the maximal mutual independence, both virtual sources and mixing vectors can be obtained by independent component analysis of the multi-source multi-detector data set $U_m(\mathbf{r}_d, \mathbf{r}_s, \omega)$.

Let us denote the recovered jth virtual source by $s_j(\mathbf{r}_s) \propto G_x(\mathbf{r}_j, \mathbf{r}_s, \omega)$ and the recovered corresponding mixing vector by $a_j(\mathbf{r}_d) \propto G_m(\mathbf{r}_d, \mathbf{r}_j, \omega)$. Both localization and strength of the jth object can be computed by a least square fitting procedure:

$$\min_{\mathbf{r}_j, \alpha_j, \beta_j} \left\{ \sum_{\mathbf{r}_s} \left[\alpha_j^{-1} s_j(\mathbf{r}_s) - G_x(\mathbf{r}_j, \mathbf{r}_s) \right]^2 + \sum_{\mathbf{r}_d} \left[\beta_j^{-1} a_j(\mathbf{r}_d) - G_m(\mathbf{r}_d, \mathbf{r}_j) \right]^2 \right\}. \tag{5}$$

The fitting yields the location r_j of and the two scaling constants α_j and β_j for the jth inhomogeneity. The fluorescence strength is then given by $f_j = \alpha_j \beta_j$.

The size and shape of the inhomogeneity can be estimated after the fluorescent object has been localized. The fluorescence signal due to the jth object is $U_{m_j}(r_d, r_s, \omega) = a_j(r_d)s_j(r_s)$. One can estimate the volume V_j of the jth object by its thickness profile $\Delta z_j(\rho)$ in the z direction where ρ is the lateral coordinate on the $z = z_j$ plane with z_j the z coordinate of the center of the jth object. The fluorescence signal from the jth object is approximately given by:

$$U_{m_j}(r_d, r_s, \omega) \simeq f_j(\omega)\frac{1}{V_j}\int G_m(\rho_d - \rho, \omega)\Delta z_j(\rho)G_x(\rho - \rho_s, \omega)d\rho \tag{6}$$

where the integration is performed over the $z = z_j$ plane, and ρ_d and ρ_s are the lateral coordinates of the detector and the source respectively. In the Fourier space, the thickness Δz_j can be solved from Eq. (6) and is given by

$$\Delta z_j(q) = \frac{V_j}{f_j(\omega)}\frac{U_{m_i}(q - q_s, q_s, \omega)}{G_m(q - q_s, \omega)G_x^*(q_s, \omega)}. \tag{7}$$

where q and q_s are the spatial frequency on the xy plane and $*$ denotes complex conjugate. The inverse Fourier transform of $\Delta z_j(q)$ yields the thickness profile of the fluorescent target in the z direction. The FWHM (full width at half maximum value) and the contour of the thickness profile provide an estimation of size and shape of the jth target, respectively. This procedure to obtain size and shape of the fluorescent inhomogeneity also applies to the absorptive and scattering inhomogeneities.

3. RESULTS

The first test of OPTICA involved imaging of two absorptive inhomogeneities using simulated data. In simulation, the absorptive objects are placed at $(50, 60, 20)$mm and $(30, 30, 30)$mm, respectively, inside a slab of volume $90 \times 90 \times 50$mm^3 shown schematically in Fig. 1(a). Each inhomogeneity has a volume of $6.75 \times 6.75 \times 4.69$mm^3 and an absorption strength of unity. The absorption and diffusion coefficients of the uniform slab is $\mu_a = 1/300$mm^{-1}and $D = 1/3$mm respectively, close to that of human breast tissue.[17] The incident CW beam scans a set of 21×21 grid points covering an area of 90×90mm^2. The spacing between two consecutive grid points is 4.5mm. The light intensity on the other side of the slab is recorded by a CCD camera on 42×42 grid points covering the same area. 10% Gaussian noise was added to the simulated light intensity change on the detector plane.

Independent component analysis of the perturbation in the spatial intensity distributions provided corresponding independent intensity distributions on the source and detector planes. ICA generated independent intensity distributions on the source and detector planes are shown in Fig. 1(b), for the two absorptive inhomogeneities. Locations of the absorptive objects are obtained from fitting these independent component intensity distributions to those of the diffusion approximation in a slab by least square. The first object is found at $(50.0, 60.0, 21.1)$mm and the second one at $(30.0, 30.0, 29.9)$mm. The xy coordinates of both objects agree exactly with their known values and the z coordinate of both objects is within 1.2mm of their known center locations. The strengths of the two objects are $q_1 = 0.88$ and $q_2 = 0.88$ respectively, with an error of $\sim 12\%$ of the true values.

The thickness map for the two absorptive objects is back-projected using a formula similar to Eq. (7) and presented in Fig. 2. For each case, the Green's function at the source and detector planes (circle) are shown with the fitting in solid lines on the first row. The longitudinal thickness map of the target and the thickness profiles along X and Y directions are also displayed on the second row. Both targets are observed to have approximately
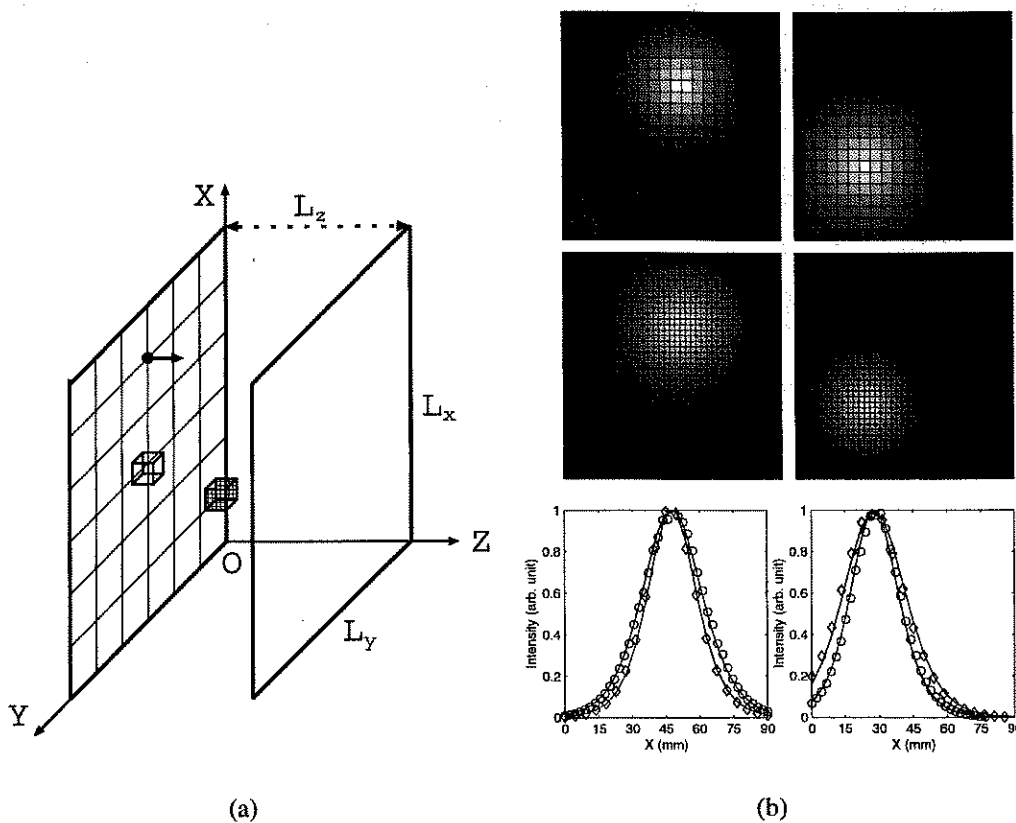
Figure 1. (a) The light intensity on one side of the slab is measured when a point source scans on the other side. Two inhomogeneities are placed at $(50, 60, 20)$mm and $(30, 30, 30)$mm inside a $90 \times 90 \times 50$mm^3 slab. (b) Normalized independent spatial intensity distributions on the source plane (the first row), the detector plane (the second row), and the least square fitting (the third row). The left column is for the first absorptive inhomogeneity at $(50, 60, 20)$mm and the right column is for the second absorptive inhomogeneity at $(30, 30, 30)$mm. On the third row, the horizontal profile of intensity distributions on the source plane (diamond) and on the detector plane (circle) are displayed, and solid lines show the respective Green's function fit used for obtaining locations and strengths of objects. The noise level is 10%.

a square shape. The FWHM of the peak for the first and the second target are found to be 16.0mm and 13.6mm, and 9.5mm and 10.5mm in the x and y directions, respectively. These values should be compared to the size of the absorptive target of 6.75mm in the xy plane. The estimation of the size and shape of the second absorptive object is more accurate as it is closer to the detector plane where the grid spacing is finer.

The second example is to image a spherical fluorescent target placed inside a 250mm×250mm × 50mm slab filled with Intralipid-10% aqueous suspension using experimental data [see Fig. 3(a)]. The fluorescent target was a 9.0mm diameter sphere filled with a solution of Indocyanine green (ICG) dye in water that could be excited in the 650nm-800nm spectral range. The wavelength of the CW incident light is $\lambda_x = 785$nm. Two long wavelength pass absorption filters were placed before the CCD camera to block the excitation wavelength and allow the fluorescence light to pass. The wavelength of the peak fluorescence light adjusted by the filtering and the camera response efficiency is about $\lambda_m = 870$nm. The Intralipid-10% suspension is diluted with pure water such that the transport mean free paths and absorption coefficients are $l_x = 1.01$mm and $\mu_{a_x} = 0.0022$mm^{-1} at the excitation wavelength and $l_{t_m} = 1.14$mm and $\mu_{a_m} = 0.0054$mm^{-1} at the emission wavelength, respectively. The sphere is placed at the position $(11, 9, 32)$mm inside the slab. The sphere is 33mm away from the input window. The point source scans over a 10×10 grid system with spacing 2.5mm between consecutive
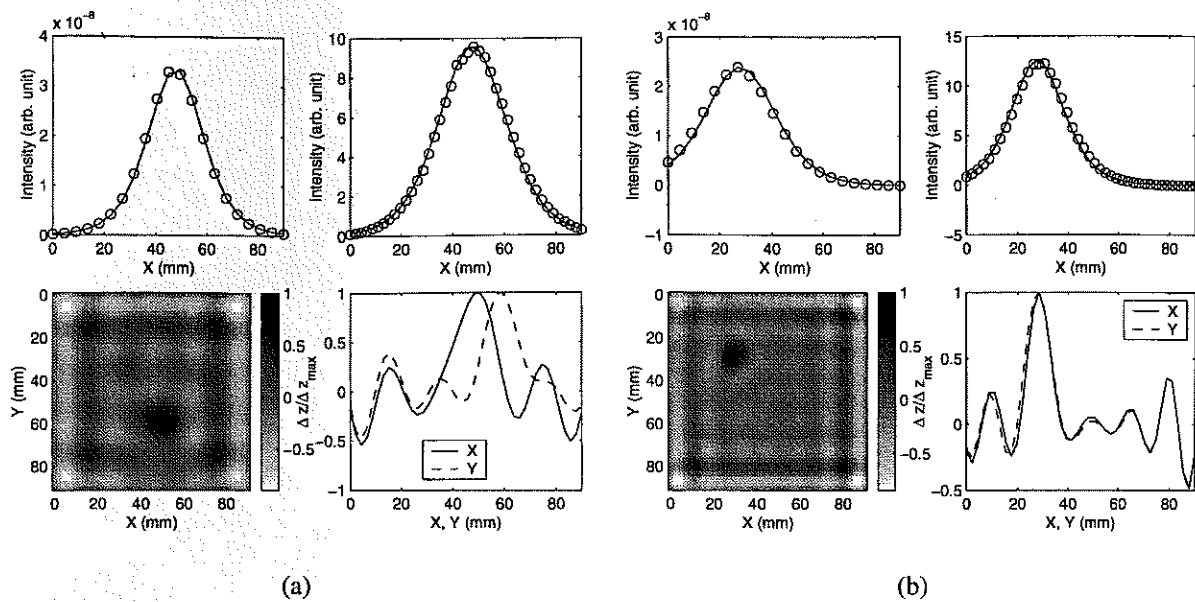
Figure 2. Fitting of the independent intensity distribution of the absorptive objects of volume $6.75 \times 6.75 \times 4.69\text{mm}^3$ inside the slab described in the text for (a) the first absorptive object at $(50, 60, 20)$mm and (b) the second absorptive object at $(30, 30, 30)$mm. For each case, the Green's function at the source and detector planes (circle) are shown with the fitting in solid lines [the first row]. The longitudinal thickness map of the target and the thickness profiles along X and Y directions are also displayed [the second row].
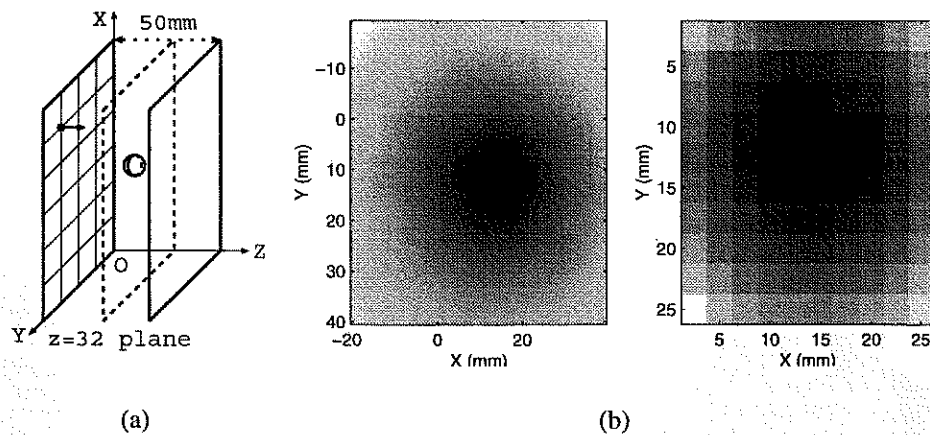
Figure 3. (a) The schematic diagram showing a fluorescent sphere embedded inside a slab. (b) Independent intensity distributions of the fluorescence from the target generated by ICA at the detector plane (Left) and at the source plane (Right). The fluorescent sphere is located on the $z = 32$mm plane.

grids. The grid spacing on the detector plane is 1.23mm.

Independent intensity distributions at the detector plane and the source plane obtained by ICA is shown in Fig. 3(b). The fluorescent target is found to be centered at $(x, y) = (11, 9)$mm and $z = 33$mm away from the input window by fitting independent intensity distributions at the detector plane and the source plane to the Green's functions in the diffusion approximation [see Fig. 4(a) and (b)]. The (x, y) coordinate agrees exactly with the known xy coordinates and the z coordinate is within 1mm error of the known z coordinate. The

Two
alized
nd the
nd the
file of
show

.6mm,
size of
sorptive

50mm
cent tar-
could be
wo long
ngth and
ering and
are water
2mm^{-1}
, respec-
from the
nsecutive
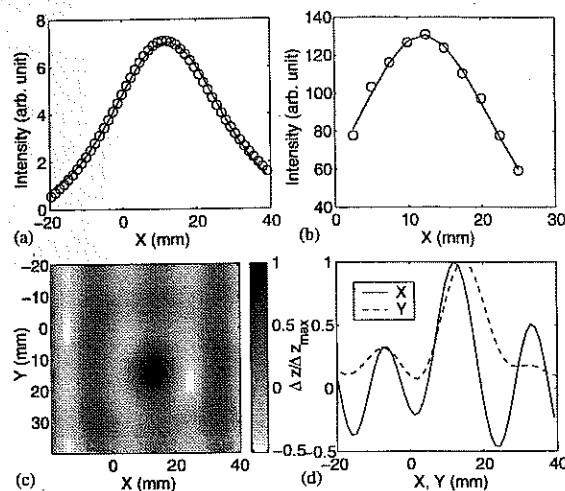
Figure 4. Fitting of the independent intensity distribution of fluorescence from a sphere of diameter 9mm embedded in Intralipid-10% solution to the Green's function (a) at the detector plane and (b) at the source plane. (c) The longitudinal thickness map of the target centered at $(11, 9)$mm. (d) The thickness profiles along X and Y directions.

fluorescence strength is obtained to be $f = 0.0462\text{mm}^3/\text{ps}$.

The thickness map is back-projected using Eq. (7) and presented in Fig. 4(c). The horizontal and vertical thickness profiles of $\Delta z/\Delta z_{max}$ passing through the center are also plotted in Fig. 4(d). The target is observed to have a circular shape. The FWHM of the peak found to be $d = 11.5$mm. This value should be compared to the diameter of the fluorescent target 9mm.

ACKNOWLEDGMENTS

REFERENCES

1. A. Yodh and B. Chance, "Spectroscopy and imaging with diffusing light," *Phys. Today* **48**(3), pp. 38–40, 1995.
2. S. K. Gayen and R. R. Alfano, "Emerging optical biomedical imaging techniques," *Opt. Photon. News* **7**(3), pp. 17–22, 1996.
3. W. Cai, S. K. Gayen, M. Xu, M. Zevallos, M. Alrubaiee, M. Lax, and R. R. Alfano, "Optical tomographic image reconstruction from ultrafast time-sliced transmission measurements," *Appl. Opt.* **38**(19), pp. 4237–4246, 1999.
4. S. R. Arridge, "Optical tomography in medical imaging," *Inverse Problems* **15**, pp. R41–R93, 1999.
5. M. Xu, M. Lax, and R. R. Alfano, "Time-resolved Fourier optical diffuse tomography," *J. Opt. Soc. Am. A* **18**(7), pp. 1535–1542, 2001.
6. H. Dehghani, B. W. Pogue, S. P. Poplack, and K. D. Paulsen, "Multiwavelength three-dimensional near-infrared tomography of the breast: initial simulation, phantom, and clinical results," *Appl. Opt.* **42**, pp. 135–145, 2003.
7. W. Cai, M. Xu, and R. R. Alfano, "Three dimensional radiative transfer tomography for turbid media," *IEEE JSTQE* **9**, pp. 189–198, 2003.
8. M. S. Patterson and B. W. Pogue, "Mathematical model for time-resolved and frequency-domain fluorescence spectroscopy in biological tissues," *Appl. Opt.* **33**, pp. 1963–1974, Apr. 1994.

9. A. B. Milstein, S. Oh, K. J. Webb, C. A. Bouman, Q. an Zhang, D. A. Boas, and R. P. Millane, "Fluorescence optical diffusion tomography," *Appl. Opt.* **42**, pp. 3081–3094, June 2003.

10. A. D. Klose and A. Hielscher, "Fluorescence tomography with simulated data based on the equation of radiative transfer," *Opt. Lett.* **28**, pp. 1019–1021, June 2003.

11. A. H. Gandjbakhche, V. Chernomordik, J. C. Hebden, and R. Nossal, "Time-dependent contrast functions for quantitative imaging in time-resolved transillumination experiments," *Appl. Opt.* **37**, pp. 1973–1981, Apr. 1998.

12. D. Nuzillard and J.-M. Nuzillard, "Application of blind source separation to 1-d and 2-d nuclear magnetic resonance spectroscopy," *IEEE Signal Processing Letters* **5**(8), pp. 209–211, August 1998.

13. R. Vigário, J. Särelä, V. Jousmäki, M. Hämäläinen, and E. Oja, "Independent component approach to the analysis of EEG and MEG recordings," *IEEE Trans. Biomedical Engineering* **47**(5), pp. 589–593, 2000.

14. A. J. Bell, "Information theory, independent component analysis, and applications," in *Unsupervised Adaptive Filtering, Vol. I*, S. Haykin, ed., pp. 237–264, Wiley, 2000.

15. A. Hyvärinen, J. Karhunen, and E. Oja, *Independent Component Analysis*, John Wiley, New York, 2001. 481+xxii pages.

16. M. Xu, M. Alrubaiee, S. K. Gayen, and R. R. Alfano, "Three-dimensional localization and optical imaging of objects in turbid media using independent component analysis," *Appl. Opt.* , 2004. (accepted).

17. H. Heusmann, J. Kölzer, and G. Mitic, "Characterization of female breasts *in vivo* by time resolved and spectroscopic measurements in near infrared spectroscopy," *J. Biomed. Opt.* **1**, pp. 425–434, 1996.

d in
linal

rtical
erved
red to

R, and
MD17-
k MD
cement

5.
pp. 17–

c image
99.

A **18**(7),

-infrared
)3.
E JSTQE

nce spec-

Localization and cross section reconstruction of fluorescent targets in *ex vivo* breast tissue using independent component analysis

M. Alrubaiee,[a] M. Xu, S. K. Gayen, and R. R. Alfano
Institute for Ultrafast Spectroscopy and Lasers, Physics Department, The City College of New York of the City University of New York, 138th Street, Convent Avenue, New York, New York 10031

An information theory based approach is introduced for the detection and three-dimensional localization of fluorescent targets embedded in a turbid medium. The approach uses multisource illumination of the medium, multidetector transillumination acquisition of fluorescence signal, independent component analysis for target detection and localization, and a back-projection algorithm for reconstruction of target cross section. The efficacy of the approach is demonstrated by locating and estimating the cross section of a fluorescent target embedded in a $100 \times 100 \times 26$ mm^3 *ex vivo* human breast tissue specimen and in a tissue-simulating turbid medium of thickness 50 times the transport mean free path. © *2006 American Institute of Physics*. [DOI: 10.1063/1.2356024]

Development of optical fluorescence tomography is of interest for cancer detection and diagnosis.[1–4] The recent advent of fluorescence beacons and contrast agents with the ability to attach themselves to desired abnormal cells or organelles[5] enhances the target specificity and diagnostic potential of fluorescence based optical imaging approaches. Determination of accurate location of targets embedded in a turbid medium remains a formidable task for both direct imaging and inverse image reconstruction approaches and for all types of targets—fluorescent, absorptive, and scattering.[6–11] We have introduced an approach, known as optical tomography using independent component analysis (OPTICA), that enables more accurate determination of target location in turbid media than existing optical methods.[12,13] It uses multisource optical probing of the sample, multidetector acquisition of transmitted signal, and independent component analysis[14] of information theory to analyze the signal for three-dimensional (3D) localization and characterization of the target. The efficacy of OPTICA for locating small absorptive and scattering targets embedded in turbid media has been demonstrated.[11,15] In this letter, OPTICA formalism is extended for fluorescent targets, and its efficacy is tested by obtaining 3D location and cross sectional image of a fluorescent target in an *ex vivo* human breast tissue sample and in a tissue-simulating turbid medium from experimental data.

The theoretical formalism for fluorescence OPTICA is based on the premise that the spatial distribution of the light intensity at the exit boundary of the medium is a weighted mixture of signals arriving from the fluorescent targets ("sources") embedded in the medium:

$$x(\mathbf{r}_d,\mathbf{r}_s) = \sum_j a_j(\mathbf{r}_d)s_j(\mathbf{r}_s), \qquad (1)$$

where $a_j(\mathbf{r}_d)$ is the mixing vector and $a_j(\mathbf{r}_d)s_j(\mathbf{r}_s)$ represents the contribution of the jth target to the fluorescent signal at the detector plane for illumination of the source plane at $\mathbf{r}_s$. Independent component analysis assumes that these fluorescent sources are independent, treats the problem of detecting those as a source separation problem, and obtains a_j and s_j

by seeking maximal mutual independence between s_j's.[12,14]

Light propagation in a highly scattering medium with an embedded fluorescent target excited by an external light source is approximately described by coupled diffusion equations at the excitation and emission wavelengths.[16,17] The fluorescence signal $U_m(\mathbf{r}_d,\mathbf{r}_s,\omega)$ can be expressed in terms of the two Green's functions $G_x(\mathbf{r},\mathbf{r}_s,\omega)$ and $G_m(\mathbf{r}_d,\mathbf{r},\omega)$ describing light propagation from the excitation source at $\mathbf{r}_s$ to the fluorescent target at $\mathbf{r}$ at the excitation wavelength λ_x and the light propagation from the target to the detector at $\mathbf{r}_d$ at the emission wavelength λ_m. In this letter we report on slab samples. Consequently, Green's functions for a slab geometry[18] under the diffusion approximation of the equation of radiative transfer are used.

Assuming that the jth fluorescent target is contained in volume V_j centered at $\mathbf{r}_j$, the fluorescence signal under excitation by a unit point source at $\mathbf{r}_s$ is given by

$$U_m(\mathbf{r}_d,\mathbf{r}_s,\omega) = \sum_{j=1}^{j} G_m(\mathbf{r}_d,\mathbf{r}_j,\omega)f_j(\omega)G_x(\mathbf{r}_j,\mathbf{r}_s,\omega), \qquad (2)$$

where $f_j(\omega) = \gamma(\mathbf{r}_j)cV_j/[1-i\omega\tau(\mathbf{r}_j)]$ represents the fluorescence signal strength of the jth target, γ is the fluorescent yield, c is the speed of light in medium, τ is the fluorescence lifetime, and ω is the angular modulation frequency of the excitation light intensity.

Both the location and the strength of the jth target can be computed by using a least square fitting procedure:

$$\min_{\mathbf{r}_j,\alpha_j,\beta_j}\left\{\sum_{r_s}[\alpha_j^{-1}s_j(\mathbf{r}_s)-G_x(\mathbf{r}_j,\mathbf{r}_s)]^2 + \sum_{r_d}[\beta_j^{-1}a_j(\mathbf{r}_d)\right.$$
$$\left. -G_m(\mathbf{r}_d,\mathbf{r}_j)]^2\right\}, \qquad (3)$$

where $s_j(\mathbf{r}_s) \propto G_x(\mathbf{r}_j,\mathbf{r}_s,\omega)$ and $a_j(\mathbf{r}_d) \propto G_m(\mathbf{r}_d,\mathbf{r}_j,\omega)$. The fitting yields the location $\mathbf{r}_j$ of and the two scaling constants α_j and β_j for the jth target. The fluorescence strength then is $f_j = \alpha_j\beta_j$.

The size and shape of the jth target can be estimated from a back projection of $U_{m_j}(\mathbf{r}_d,\mathbf{r}_s,\omega)$ from the detection plane onto the "target plane," i.e., $z=z_j$ plane. The fluorescence signal from the jth target is approximated by

[a]Electronic mail: malrub@sci.ccny.cuny.edu

$$U_{m_j}(\mathbf{r}_d,\mathbf{r}_s,\omega) = \int G_m(\boldsymbol{\rho}_d - \boldsymbol{\rho},\omega)X_j(\boldsymbol{\rho})G_x(\boldsymbol{\rho} - \boldsymbol{\rho}_s,\omega)d\boldsymbol{\rho},$$

$$(4)$$

where the integration is over the $z=z_j$ plane and $\boldsymbol{\rho}_d$ and $\boldsymbol{\rho}_s$ are the lateral coordinates of the detector and the source, respectively. In the Fourier space, $X_j(\mathbf{q})$ can be obtained from Eq. (4) as

$$X_j(\mathbf{q}) = \frac{U_{m_j}(\mathbf{q} - \mathbf{q}_s, \mathbf{q}_s, \omega)}{G_m(\mathbf{q} - \mathbf{q}_s, \omega)G_x^*(\mathbf{q}_s, \omega)},$$

$$(5)$$

where $\mathbf{q}$ and $\mathbf{q}_s$ are the spatial frequencies on the x-y plane and * denotes complex conjugate. The inverse Fourier transforms of $X_j(\mathbf{q})$ yield the cross sectional image of the fluorescent target in the $z=z_j$ plane. The full width at half maximum (FWHM) of the cross sectional image provides an estimate of the real target size. The cross sectional image is a two-dimensional (2D) distribution of the fluorescent object at the target plane.

The experimental arrangement to test the fluorescence OPTICA approach is shown schematically in Fig. 1(a). The fluorescent target was a glass sphere (outer diameter of ~4 mm and inner diameter of 3.2 mm) filled with a solution of indocyanine green (ICG) in water. The water solution of ICG had an absorption coefficient of 11.5 cm^{-1} at 784 nm and fluoresced over the 790–966 nm spectral range with a peak at 825 nm. The sphere was placed inside a $100 \times 100 \times 26$ mm^3 slab of *ex vivo* female breast tissue specimen contained in a transparent plastic box. One of the sides of the box could be moved to uniformly compress and hold the tissue specimen in position. The breast tissue specimen consisted primarily of adipose tissue with small amount of skin and was provided to us by the National Disease Research Interchange under an Internal Review Board approval at the City College of New York. In another experiment to test if the approach could locate a target inside an average-size human female breast, the sphere was placed inside a $250 \times 250 \times 50$ mm^3 transparent plastic cell filled with Intralipid-10% suspension in water. The concentration of Intralipid-10% was adjusted to provide transport lengths l_t of ~1 mm at 784 nm and 1.1 mm at 830 nm, which are within the reported range of values for healthy human breast tissues.[19]

A 200 μm optical fiber delivered a 784 nm, 300 mW continuous-wave beam from a diode laser for sample illumination. The beam was collimated to a 1 mm spot onto the entrance face (henceforth referred to as the "source plane") of the slab samples. Multiple source illumination was realized in practice by step scanning the slab samples across the laser beam in an x-y array of grid points using a computer controlled translation stage. The x-y array was 18×15 for the tissue sample and 10×10 for the Intralipid-10% sample, with a step size of 2.5 mm for both the cases. The signal from the opposite face of the sample (henceforth referred to as the "detection plane") was passed through a narrow-band interference filter centered at 830 nm (FWHM ~10 nm, 50% transmission) to block the scattered 784 nm pump light. A camera lens collected the fraction of filtered fluorescence around 830 nm and projected it onto the sensing element of a cooled 16 bit, 1024×1024 pixel charged couple device (CCD) camera. Each illuminated pixel of the CCD camera could be regarded as a detector. For illumination of every scanned point on the source plane, the CCD camera recorded
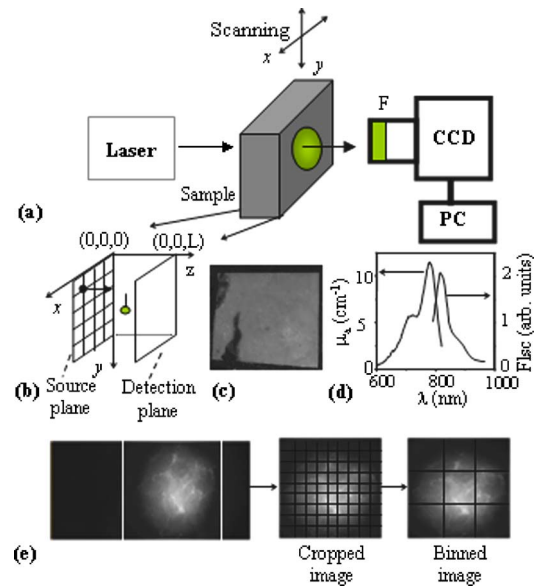

FIG. 1. (a) Schematic diagram of the experimental arrangement (CCD =charge coupled device camera, F=filter, PC=personal computer). (b) An expanded view of the sample input (source) plane and exit (detection) plane showing the grid points in the x-y plane. (c) A photograph of the exit face of the tissue sample. (d) Absorption and fluorescence spectra of the ICG dye solution in water. (e) A typical raw CCD image of the detection plane and how it is cropped and binned for analysis.

the diffusely transmitted 2D fluorescence intensity pattern on the detection plane. A second scan to estimate the average value of $\kappa = \sqrt{3\mu_a\mu_s'}$ (where μ_a and μ_s' are the absorption and scattering coefficients, respectively) of the background medium used a short-pass filter at 750 nm to block the fluores-
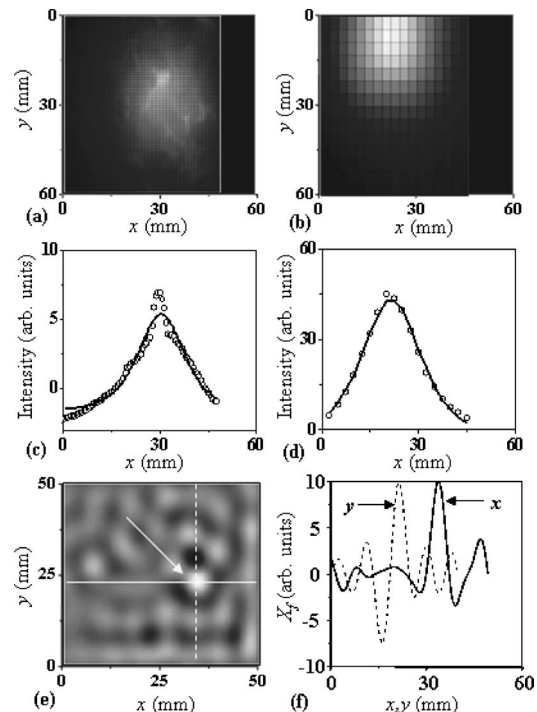

FIG. 2. OPTICA generated fluorescence intensity distribution on (a) the detector and (b) the source planes. [(c) and (d)] Green's function fits to the horizontal spatial profiles through the centers of intensity distributions in (a) and (b), respectively. (e) Cross sectional image at the $z=z_j$ plane. (f) Spatial profiles of the cross sectional image along the x and y directions shown by the white lines in (e).

TABLE I. Comparison of known positions and sizes of the target with OPTICA-determined values.

Samples	Known position (x, y, z) (mm)	Observed position (x, y, z) (mm)	Profile FWHM[a] $(\Delta x, \Delta y)$ (mm)
Breast tissue *ex vivo*	(30, 27, 15)	(30, 27, 16)	(4, 4)
Intralipid-10% in water	(115, 115, 15)	(115, 115, 16)	(12, 12)

[a]The FWHM values should be compared with the inner diameter of 3.2 mm of the sphere.

cence signal and admit a very small fraction of the transmitted excitation light.

Figure 1(b) shows a photograph of the exit surface of the tissue sample. Figure 1(c) presents a typical 2D raw image (fluorescence intensity distribution) of the detection plane recorded by the CCD camera for illumination of a grid point in the source plane. Each raw image is then cropped to select out the information-rich region and binned to enhance the signal-to-noise ratio. All the binned images corresponding to illumination of the grid points in sequence are then stacked and used as input for independent component analysis.

Figures 2(a) and 2(b) present the OPTICA generated intensity distributions on the detector and source planes, respectively, of the tissue sample. The corresponding Green's function fits to horizontal profile through the center of intensity distributions are shown in Figs. 2(c) and 2(d), respectively. The (x, y, z) location of the target center obtained from this analysis is displayed in Table I. The lateral positions (x, y) agree completely, and the axial position agrees within 1 mm of the known values. The cross sectional image obtained using back-projection Fourier transforms in Eq. (5), is shown in Fig. 2(e). Figure 2(f) shows intensity profiles of the cross sectional image along the x and y directions shown by the white dotted lines in Fig. 2(e). The FWHM values of intensity profiles of the cross sectional image, presented in column 4 of Table I, are 4 mm, in good agreement with the known 3.2 mm inner diameter of the fluorescent sphere.

The results of measurements on the same fluorescent sphere embedded in Intralipid-10% suspension in water are also summarized in Table I. Again the lateral positions are in exact agreement, while the axial position agrees within 1 mm. However, the FWHM values of the intensity profiles of the cross sectional image are estimated to be 12 mm each, which is 3.7 times the 3.2 mm inner diameter of the sphere. We attribute this difference primarily to the much larger thickness $(50l_t)$ of the Intralipid-10% sample than that of the tissue sample $(26l_t)$. Spatial resolution decreases rapidly with sample thickness (for the same axial target position) because of the diffuse nature of light propagation through a highly scattering medium. Since the transport lengths (l_t) were comparable and the target was located 15 mm from the source plane for both the samples, the target-detector plane distance in Intralipid-10% sample was more than three times larger than that in the tissue sample, which in turn led to a much higher estimate for the target size. As the incident beam power was limited to 300 mW for both the samples, higher optical thickness resulted in much lower fluorescence signal-to-noise ratio for the Intralipid-10% sample, which in turn contributed to a higher estimate of the target cross section. Substantial improvements in target size estimate are expected if an intensified CCD camera for higher sensitivity, and more incident beam powers are used.

It should be noted that multisource measurements, though crucial for detection of multiple targets, might not be needed for a single target, since the position of the target determines the normalized fluorescence intensity distribution. However, multisource measurements help reduce the deleterious effects of noise and inaccuracy in the estimation of optical properties of the medium and provide better assessment of 3D location even in the case of a single target.

The simpler but important case involving a single target (e.g., a tumor in the breast) was chosen for experimental demonstration. In simulation the approach could locate three targets with one target $\sim 20l_t$ behind another in a $\sim 50l_t$ thick turbid medium. Localization of even more targets is possible and will be presented along with experimental results in a future publication.

In summary, OPTICA can provide rather accurate 3D location of a fluorescent target in a turbid medium and an estimate of its cross section.

[1]C. D'Andrea, L. Spinelli, D. Cornelli, G. Valentini, and R. Cubeddu, Phys. Med. Biol. **50**, 2313 (2005).

[2]I. Gannot, V. Chernomordik, A. Garashi, and A. Gandjbakhche, Opt. Lett. **29**, 742 (2004), and Ref. 7 therein.

[3]A. Eidsath, V. Chernomordik, A. Gandjbakhche, P. Smith, and A. Russo, Phys. Med. Biol. **47**, 4079 (2002), and Refs. 2, 5, and 6 therein.

[4]A. B. Thompson, D. J. Hawrysz, and E. M. Sevick-Muraca, Appl. Opt. **42**, 4125 (2003), and Ref. 8 therein.

[5]Sanjay Tyagi, Salvatore A. E. Marras, and Fred Russell Kramer, Nat. Biotechnol. **18**, 1191 (2000).

[6]Alexander D. Klose and Andreas H. Hielscher, Opt. Lett. **28**, 1019 (2003).

[7]M. A. O'Leary, D. A. Boas, X. D. Li, B. Chance, and A. G. Yodh, Opt. Lett. **21**, 158 (1996).

[8]W. Cai, S. K. Gayen, M. Xu, M. Zevallos, M. Alrubaiee, M. Lax, and R. R. Alfano, Appl. Opt. **38**, 4237 (1999).

[9]V. Ntziachristos and R. Weissleder, Opt. Lett. **26**, 893 (2001).

[10]S. R. Arridge, Inverse Probl. **15**, R41 (1999).

[11]A. D. Kim and A. Ishimaru, Appl. Opt. **37**, 5313 (1998).

[12]M. Xu, M. Alrubaiee, S. K. Gayen, and R. R. Alfano, Appl. Opt. **44**, 1889 (2005).

[13]M. Xu, M. Alrubaiee, S. K. Gayen, and R. R. Alfano, J. Biomed. Opt. **44**, 1889 (2005).

[14]J.-F. Cardoso, Proc. IEEE **86**, 2009 (1998).

[15]M. Alrubaiee, M. Xu, S. K. Gayen, M. Brito, and R. R. Alfano, Appl. Phys. Lett. **87**, 191112 (2005).

[16]M. S. Patterson and B. W. Pogue, Appl. Opt. **33**, 1963 (1994).

[17]A. B. Milstein, S. Oh, K. J. Webb, C. A. Bouman, Q. Zhang, D. A. Boas, and R. P. Millane, Appl. Opt. **42**, 3081 (2003).

[18]M. Lax, V. Narayanamurti, and R. C. Fulton, in *Laser Optics of Condensed Matter*, edited by J. L. Birman, H. Z. Cummins, and A. A. Kaplyanskii (Plenum, New York, 1987), pp. 229–237.

[19]H. Heusmann, J. Kölzer, and G. Mitic, J. Biomed. Opt. **1**, 425 (1996).

Three-dimensional optical tomography of objects in turbid media using the 'round-trip matrix'

W. Cai, M. Alrubaiee, S. K. Gayen, M. Xu, R. R. Alfano

Institute for Ultrafast Spectroscopy and lasers, Physics Department

The City College of New York, New York, NY 10031

ABSTRACT

A new algorithm based on multi-static data and vector subspace classification to eigenvectors of a round-trip matrix is introduced for optical imaging and localization of objects embedded in a turbid medium. The transport of light from multiple sources through excitation of the embedded objects to the array of detectors is represented by a response matrix that can be constructed from experimental data. The 'round-trip (RT) matrix' is constructed by multiplying the response matrix by its transpose for continuous-wave (adjoint matrix for frequency domain) illumination. Mathematically, the RT matrix is equivalent to transfer of light from the sources via the embedded objects to the array of detectors and back, and is similar to the time-reversal matrix used in the general area of array processing for acoustic and radar time-reversal imaging. The eigenvectors with leading non-zero eigenvalues of the RT matrix correspond to embedded objects, which are orthogonal to the vectors in the noise subspace. The vector subspace method along with Green's functions calculated from an appropriate model for light propagation through turbid media is then used to determine the locations of the embedded objects. We tested this algorithm in simulation for light transmitting through a 50 l_{tr} thick ($l_{tr} \sim 1$ mm is transport mean free path) parallel slab turbid medium with up to six embedded absorptive objects. The method was able to globally locate all six objects with surprising accuracy. This "round-trip tomographic imaging" approach is fast, applicable to different geometries and to different forward models.

Key words: Image reconstruction; Turbid media; Optical medical imaging; Time reversal imaging.

I. Introduction

Search of reliable and fast running approaches for inverse image reconstruction of turbid medium is an important task for optical imaging of human's tissue, breast, prostate, et al. Recent inverse algorithms, such as Newton-Raphson-Marquart algorithms [1] and that direct linear inversion of 3-D matrices [2], are time consuming. The iterative methods may not ensure that the obtained result arrives at a "global minimum," and does not converge to a "local minimum," which is not a true image.

In this paper, a new algorithm based on multi-static data and vector subspace classification to eigenvectors of a round-trip matrix is introduced for optical imaging and localization of objects embedded in a turbid medium. The transport of light, from multiple sources through excitation of the embedded objects to the array of detectors, is represented by a response matrix that can be constructed from experimental data. The 'round-trip (RT) matrix' is constructed by multiplying the response matrix by its transpose for continuous-wave (adjoint matrix for frequency domain) illumination. Mathematically, the RT matrix is equivalent to transfer of light from the sources via the embedded objects to the array of detectors and back, and is similar to the time-reversal matrix used in the general area of array processing for acoustic and radar time-reversal imaging. The time reversal imaging approaches [3-7] were successfully applied in areas of acoustic propagation and coherent propagation of electro-magnetic wave in vacuum space.

The eigenvectors with leading non-zero eigenvalues of the RT matrix correspond to embedded objects, which are orthogonal to the vectors in the noise subspace. The vector subspace method, which is called "Multiple-Signal-Classification" (MUSIC), along with Green's functions calculated from an appropriate forward mode, is then used to determine the locations of the embedded objects. We test and apply the this imaging method for light propagation in highly scattering turbid media, where the phase coherence of light no longer exist, and photons are scattered and diffuse into a broad area of detectors. The testing results using simulated data show that this method is able to globally locate the hidden objects with surprising accuracy even in a highly scattering turbid medium. When the locations of heterogeneities are found, inversion of optical parameters for these objects can be much easier than that were unknown. Since this imaging method is simple, running very fast, and can be generally applied for different geometries and other conditions, it is expected that the imaging approach have broad applications in medical imaging

II. The steps of performing imaging using the round-trip matrix

The following steps will be performed to locate the hidden objects in a turbid medium.

(1) When a set of experimental data of light intensity injected from source R_j and received by detector R_l (l, $j = 1$, 2,...., N) is obtained, a $N \times N$ response matrix K (K_{lj} or K_{jl}) is constructed by subtracting the corresponding data in a background medium.

(2) A $N \times N$ round-trip matrix $T = K^t K$ for the frequency domain, or $T = K^T K$ for CW case, is constructed (either SDxDS for K_{lj}; or DSxSD for K_{jl}), where K^t and K^T are, separately, the adjoint matrix and the transpose matrix of K; The T matrix is Hermitian (or real and symmetry in CW case), which had N real eigenvalues, and their eigenvectors are orthogonal with each other. All the eigenvalues and the eigenvectors of the T matrix are computed (for example, using the standard UV decomposition codes).

(3) Separating the non-zero eigenvalues of T from the near-zero eigenvalues, the number of non-zero eigenvalues, M, determines the number of hidden objects. The corresponding eigenvectors are μ_m, $m = 1$,...., M (each has N components). Up to this step, no physical forward model of light propagation is introduced yet.

(4) A multiple signal classification (MUSIC) approach is used to determine the locations of M hidden objects: The 3D medium is divided to p voxels. The Green's function is calculated using a proper forward model. [$G^s(X_p, R_j)$ for SDxDS case, or $G^d(R_l, X_p)$ for DSxSD case], where X_p is the position of pth voxel. These Green's functions for the pth voxel form a vector g_p of N components. A pseudo spectrum can be computed according to the following formula:

$$P(\mathbf{X}_p) = \frac{< \mathbf{g}_p , \mathbf{g}_p >}{\left| < \mathbf{g}_p , \mathbf{g}_p > - \sum_{m=1}^{M} \left| < \mu_m , \mathbf{g}_p > \right|^2 \right|} \quad , \tag{1}$$

where the inner product $\left\langle A, B \right\rangle = \sum_{n=1}^{N} A^*(n)B(n)$. A maximum value of $P(\mathbf{X}_p)$ at $\mathbf{X}_p$, which is the position of one

of the M hidden objects. By sorting of $P(\mathbf{X}_p)$, the positions of embedded objects are determined.

III. Testing based on simulation data

A slab turbid medium, with a transport mean free path $l_{tr} = 1$ mm, absorption length $l_a = 300$ mm, and thickness $z_d = 50$ mm, is divided into 20 layers. A CW light source, injected perpendicular to the $z_s = 0$ plane, scans by a 16x16 array on the x-y plane, with each pixel 5x5mm^2. An array of detectors with the same spacing is located at z = z_d plane (transmission geometry). The medium is divided into 16x16x20 voxels, each of dimension 5x5x2.5 mm^3. The indices (i, j, l) represent the (x, y, z) coordinates of the voxel. Six ($M = 6$) absorbing objects are located in the medium, separately, at A(6,8,4), B(13,10,10), C(10,7,6), D(6,9,6), E(7,9,6), and F(8,12,14), with absorption difference of $\Delta \mu_a = 0.01$ mm^{-1} from the background. The objects D, and E are attached, and their x-y positions are close to that of A, hence, the objects D, E, A, are difficult to be distinguished. The objects C, D, E, are located in the same z layer.

Using a diffusion model of light propagation in slab geometry, intensities from the source array to the detector array through medium with and without hidden objects are calculated and subtracted. The data with adding (a) noise = 0, (b) noise = 5% are produced as simulated "experimental" data. The dimension of the K matrix (sources are in row, and detectors are in column) is $N = 16 \times 16 = 256$. Then, the matrix $T = K^T K$ (DSxSD) is constructed from simulated data, and 256 eigenvalues of T and corresponding eigenvectors is computed.

The computed data of eigenvalues are sorted in descent order and are listed in the *first column* of the table 1. At this stage (without calculation of the Green's function), we have seen that there are 6 largest eigenvalues, which can be clearly distinguished from other near-zero eigenvalues. Hence, the signal space is determined as $M = 6$ from simulated data. Next step, the diffusion model is used to calculate the Green's functions from a voxel to the detectors (need not that from the sources to the voxel), and the pseudo-spectrum (16x16x20) is calculated according to Eq. (1) using these Green's function and the computed M eigenvectors in the signal space. The values of pseudo-spectrum are sorted in descent order. The largest values of them and the corresponding positions of voxels are listed in the *second column* in the table 1.

We see that for the zero-noise case, the six non-zero eigenvalues are more 10 orders of magnitude larger than other near-zero eigenvalues. All six largest pseudo-values are located at the correct locations we set previously, and their values are more 10 orders of magnitude larger than the value at their neighborhood locations. This result is magically well.

For the case of 5% noise, the values of the near-zero eigenvalues greatly increase, but still one order of magnitude less than smallest non-zero eigenvalue, as shown on the *third column* in the table 1. The pseudo-values, shown in the *fourth column* of the table 1, at locations (13,10,10), (10,7,6), and (8,12,14), although have greatly reduced comparing to the zero-noise case, are clearly maximum comparing to their neighborhood, that is the well resolved case we discuss before. The pseudo-value at (6,8,4) is also a maximum. The pseudo-values at (6,9,6) and (7,9,6) can be regarded as a local maximum, although the maximum for object at (7,9,6) has been little bit moved. All these peaks are among the largest values in 256x20 values in the pseudo-spectrum. This image result is quite well comparing to that of other image reconstruction approaches.

(a) simulated data (no noise)

eigen value	i	j	l	P(i,j,l)
5.878267e-10	13	10	10	3.071404e+15
4.244296e-11	7	9	6	2.982245e+15
1.584357e-11	10	7	6	1.275038e+15
3.861900e-12	6	9	6	7.403212e+14
1.094898e-13	8	12	14	5.251203e+14
8.792975e-15	6	8	4	4.044517e+14
3.239483e-25	6	8	3	5912.727
7.226278e-26	7	9	5	4089.3306
6.936422e-26	6	8	5	3767.8683
6.689055e-26	7	9	7	3053.547
6.411725e-26	6	9	5	2816.3402
6.326671e-26	10	7	5	2485.2019
6.055272e-26	6	9	7	2065.8781

(b) simulated data (5% noise)

eigen value	i	j	l	P(i,j,l)
5.878410e-10	13	10	10	51384.399
4.239479e-11	10	7	6	23437.917
1.582402e-11	8	12	14	18144.901
3.858276e-12	10	7	5	2200.9195
1.136558e-13	6	8	4	2105.3805
-1.473045e-14	10	7	7	1697.181
-9.815438e-15	6	8	3	1476.2329
-8.444224e-15	7	9	5	1327.5666
7.192133e-15	6	8	5	1271.6959
-6.470322e-15	7	9	4	977.96331
6.156419e-15	7	9	6	924.28242
-4.679483e-15	6	8	2	923.62776
-4.508637e-15	13	10	9	791.29503
4.028535e-15	10	7	4	711.70233
3.657569e-15	6	9	6	656.91035
3.372298e-15	7	9	3	625.15459
3.087945e-15	6	9	7	596.06539
-2.838656e-15	13	10	11	554.31961

IV. Advantages of the approach

(1) This approach is simple and running very fast. If the weight matrix in the above example is written, it is 256x256 in row and 256x20 in column. In "round-trip matrix" imaging, the problem is reduced to make a singular value decomposition of a matrix of 256 in row and 256 in column. Computation can be completed in a few minute on a personal computer.
(2) As shown above, the positions of objects can be globally determined, and the image results are quite well.
(3) Only one kind Green's function is needed, either that from sources to a voxel or that from a voxel to detectors. Hence, the requirement for the forward model is reduced. Especially, error due to use of the diffusion model in computation of the Green's function from the sources to voxels can be avoided, if only the Green's function from voxels to detectors is required.
(4) This approach can be generally used under many different conditions, either parallel geometry or cylindrical geometry.

(5) The background medium may be uniform or non-uniform, as long as the Greens function of the background can be estimated. For example, this algorithm may be used for imaging based on the difference of data obtained using different wavelengths.

V. Brief description of theory for the imaging using the round-trip matrix

The theoretical foundation of the above approach is based on the work by A. J. Devaney [3].

Experimental data are collected by a array of multiple-sources and multiple-detectors, which are expressed by a response matrix K. In a linear form using the Born perturbation method, the K matrix can be theoretically expressed as:

$$K = \{K_{l,j}\} = \sum_{m=1}^{M} G^d(\mathbf{R}_l, \mathbf{X}_m)\tau_m G^s(\mathbf{X}_m, \mathbf{R}_j) \equiv \sum_{m=1}^{M} g_m^d \tau_m g_m^s \qquad (2)$$

or

$$K = \{K_{j,l}\} = \sum_{m=1}^{M} G^s(\mathbf{X}_m, \mathbf{R}_j)\tau_m G^d(\mathbf{R}_l, \mathbf{X}_m) = \sum_{m=1}^{M} g_m^s \tau_m g_m^d$$

where $l, j = 1, 2, \ldots, N$ are, separately, indices of detectors and sources, $m = 1, 2, \ldots, M$ is the index of hidden objects, with $M < N$; $\mathbf{R}_j$, $\mathbf{R}_l$, and $\mathbf{X}_m$ are, respectively, the positions of a source, a detector, and an object; τ_m is difference of the optical parameters (absorption and scattering) of the object from that of the background medium (the background medium may be uniform or non-uniform), and $G^s(\mathbf{X}_m, \mathbf{R}_j)$ and $G^d(\mathbf{R}_l, \mathbf{X}_m)$ are the Green's functions in the background medium. The vector $g_m = [G(\mathbf{X}_m, \mathbf{R}_1), G(\mathbf{X}_m, \mathbf{R}_2), \cdots, G(\mathbf{X}_m, \mathbf{R}_N)]$ in Eq. (1) has N components.

When data of the K matrix is obtained by measurements, a NxN round-trip matrix $T = K^{\dagger}K$ for the frequency domain, or $T = K^T K$ for CW case, is constructed (SDxSD for K_{lj}; or DSxSD for K_{jl}), where $K^{\dagger}$ and K^T are, separately, the adjoint matrix and the transpose matrix of K. This T matrix was called the "time-reversal" matrix, as time-reversal process in time-domain becomes phase conjugation in the frequency-domain through a Fourier transform. In the time-reversal experiments, a special "phase conjugate" mirror is applied, that the process after reflected from the mirror is equivalent to a time-reversal process, instead of a process along future of time. However, we do not see this time-reversal process, especially, in CW case. What we see is a round-trip from sources to detectors, and then back to sources (or, theoretically, from detectors to source, and back to detectors). Therefore, a "round-trip" matrix may be proper for description of the T matrix here. The T matrix is Hermitian (or real and symmetry in CW case), hence, its eigenvalues are real and the corresponding eigenvectors consist a complete set of orthonormal vectors.

In the many cases, it can be proved that **the rank of T matrix equals to the number of hidden objects M**, which means this matrix has M non-zero eigenvalues. The corresponding eigenvectors construct a signal subspace. The $N - M$ eigenvectors with zero eigenvalues (or near zero, in the case of presence of noise) construct a noise subspace. These two subspaces are orthogonal with each other. Use of orthogonality of eigenvectors of the T matrix is the main tool for accurately locating hidden objects in a turbid medium using time-reversal imaging.

The T matrix (for DSxSD) can be written as:

$$T = \left[\sum_{m=1}^{M} g_m^d \tau_m g_m^s\right]^* \left[\sum_{m'=1}^{M} g_{m'}^s \tau_{m'} g_{m'}^d\right] = \sum_{m=1}^{M}\sum_{m'=1}^{M} \Lambda_{m,m'} g_m^{d*} g_{m'}^d \qquad (3)$$

where

$$\Lambda_{m,m'} = \tau_m \tau_{m'} < g_m^s, g_{m'}^s > = \tau_m \tau_{m'} \sum_{j=1}^{N} G^{s*}(\mathbf{X}_m, \mathbf{R}_j) G^s(\mathbf{X}_{m'}, \mathbf{R}_j) , \qquad (4)$$

where the inner product is defined as $\left\langle A, B\right\rangle = \sum_{n=1}^{N} A^*(n)B(n)$.

For a well-resolved case, we have $< g_m^s, g_{m'}^s > \approx 0, < g_m^d, g_{m'}^d > \approx 0$ when $m \neq m'$. We interpret the quantity

$$H^d(\mathbf{r}, \mathbf{X}_m) = \sum_{n=1}^{N} G^d(\mathbf{R}_n, \mathbf{r})^* G^d(\mathbf{R}_n, \mathbf{X}_m) , \qquad (5)$$

as being the point spread function (PSF) of the detector array, which represents an "image" of object m from measurements on N detectors in terms of the *backprojection* of the outgoing wave Green's function. If the object m' is located far enough from the object m, that is $H(\mathbf{X}_{m'}, \mathbf{X}_m) \approx 0$, then these two objects are regarded to be well resolved.

If all M objects are well resolved each other, we have $\Lambda^s_{mm'} = \Lambda^s_m \delta_{mm'}$ and $T = \sum_{m=1}^{M} \Lambda^s_m g^{d*}_m g^d_m$,

$\Lambda^s_m = |\tau_m|^2 \rho^s_m$, with a normalized factor $\rho^s_m = <g^s_m, g^s_m>$. In this case, we can prove that M non-zero eigenvectors

are precisely $\mu_m = g^{d*}_m /(\rho^d_m)^{1/2}$, and the corresponding non-zero eigensvalues are $|\tau_m|^2 \rho^s_m \rho^d_m$.

[prove] $\quad T g^{d*}_{m_0} = \sum_{m=1}^{M} \Lambda^s_m g^{d*}_m g^d_m g^{d*}_{m_0} = \sum_{m=1}^{M} \Lambda^s_m g^{d*}_{m_0} \rho^d_m \delta_{m,m_0} = |\tau_{m_0}|^2 \rho^s_{m_0} \rho^d_{m_0} g^{d*}_{m_0}$. $\qquad$ (6)

The non-zero eigenvalue of mth object is related to the optical strength of the object, and the Green's function from this object to the sources and detectors. In the well resolved case, when the eigenvectors $\mu_m(j)$ in the signal subspace are computed using a Green's function based a forward model. The locations of targets can be determined by:

$$\psi_m(\mathbf{r}) = \sum_{j=1}^{N} G(\mathbf{r}, \mathbf{R}_j) \mu_m(j) = \frac{1}{(\rho_m)^{1/2}} H^*(\mathbf{r}, \mathbf{X}_m) \ , \qquad (7)$$

where $H(\mathbf{r}, \mathbf{X}_m)$ is the point spread function of a target located at $\mathbf{X}_m$. The maximum of $H(\mathbf{r}, \mathbf{X}_m)$ at $\mathbf{r}$ determines the position of mth target.

The M eigenvectors span the signal subspace P_S. Because T is a NxN matrix, other $N-M$ eigenvectors have zero eigenvalues and span the noise subspace P_N, and $P_S + P_N = I$. In the case of non-well-resolved targets, the vector characterizing an object can be a linear combination of several eigenvectors in the signal subspace, hence, Eq. (7) is not available for determining locations of objects. A MUSIC approach is applied to determine the locations of targets, which uses the property that any linear combination of eigenvectors in the signal subspace must be orthogonal to the vectors in the noise subspace. We use a forward model to calculate the Green's function at test location $\mathbf{X}_p$:

$$g(\mathbf{X}_p) = [G(\mathbf{X}_p, \mathbf{R}_1), G(\mathbf{X}_p, \mathbf{R}_2), \cdots, G(\mathbf{X}_p, \mathbf{R}_N)] \ . \qquad (8)$$

MUSIC uses a pseudo-spectrum to determine the target locations. After the eigenvectors in the noise space u_j are obtained, the following pseudo-spectrum can be computed:

$$P(\mathbf{X}_p) = \frac{1}{\sum_{\Lambda_j \approx 0} |\langle u_j, g(\mathbf{X}_p) \rangle|^2} \ , \qquad (9)$$

that $P(\mathbf{X}_p)$ become large at object locations and will be small otherwise. It is more convenient to use $P_N = I - P_S$, and apply the eigenvectors in the signal space instead of the eigenvectors in the noise space. We have

$$\sum_{j=M+1}^{N} \left| \langle \mu_j, g_p \rangle \right|^2 = |[I - P_S] g_p|^2 = \left| g_p - \sum_{m=1}^{M} \mu_m \langle \mu_m, g_p \rangle \right|^2 = |g_p|^2 - \sum_{m=1}^{M} |<\mu_m, g_p>|^2 . \qquad (10)$$

The denominator of the Eq. (1) is obtained from Eq. (10). We use $|g_p|^2$ in the numerator of Eq. (1) to make the expression normalized.

VI. Summary

In this paper we test the image algorithm using the round-trip matrix to locate hidden objects in highly scattering turbid media using light signals of an array of multiple sources-detectors. The testing results using simulated data show that this method is able to globally locate the hidden objects with high accuracy in a highly scattering turbid medium. Since this image method is simple, running very fast, and can be generally applied for different geometries and other conditions, it is expected that the approach has broad applications in medical imaging.

References:
1. B. A. Brooksby, H. Dehghani, B. W. Pogue, K. D. Paulsen, "Near-Infrared (NIR) Tomography Breast Image Reconstruction with A Priori Structural Information From MRI: Algorithm Development for Reconstructing Heterogeneities", IEEE IJSQEN **9** p199-209 (2003).
2. Y. Tao, Y. Wang, Y. Pei, W. Zhu, R. L. Barbour, "Frequency-domain optical imaging of absorption and scattering distribution using a born iterative method," J. Opt. Soc. Am. A **14** 325-342 (1997).
3. A. J. Devaney, "Super-resolution Processing of Multi-static Data Using Time Reversal and MUSIC", Preprint.
4. A. J. Devaney, "Time Reversal Imaging of Obscured Targets From Multstatic Data", Preprint.
5. C. Prada, J. L. Thomas, M. Fink, "The iterative time reversal process: Analysis of the convergence", J. Acoustical Society of America, **97**, 62 (1995).
6. C. Prada, S. Manneville, D. Spokiansky, and M. Fink, " Decomposition of the time reversal operator: Detection and selective focusing on two scatterers", J. Acoustical Society of America, **99**, 2067 (1996).
7. P. Stoica, R. Moses, *Introduction to Spectral Analysis*, Prentice Hall, New jersey (1997).

Analytical cumulant solution of the vector radiative transfer equation investigates backscattering of circularly polarized light from turbid media

Wei Cai, Xiaohui Ni, S. K. Gayen, and R. R. Alfano

Institute for Ultrafast Spectroscopy and Lasers, Department of Physics, The City College of City University of New York, New York, New York 10031, USA

(Received 6 April 2006; published 8 November 2006)

The backscattering of circularly polarized light pulses from an infinite uniform scattering medium is studied as a function of helicity of the incident light and size of scatterers in the medium. The approach considers a polarized short pulse of light incident on the scattering medium, and uses an analytical cumulant solution of the vector radiative transfer equation with the phase matrix obtained from the Mie theory to calculate the temporal profile of scattered polarized photons for any position and any angle of detection. The general expression for the scattered photon distribution function is an expansion in spatial cumulants up to an arbitrary high order. Truncating the expansion at the second-order cumulant, a Gaussian analytical approximate expression for the temporal profile of scattered polarized photons is obtained, whose average center position and half width are always exact. The components of scattered light copolarized and cross polarized with that of the incident light can be calculated and used for determining the degree of polarization of the scattered light. The results show that circularly polarized light of the same helicity dominates the backscattered signal when scatterer size is larger than the wavelength of light. For the scatterers smaller than the wavelength, the light of opposite helicity makes the dominant contribution to the backscattered signal. The theoretical estimates are in good agreement with our experimental results.

I. INTRODUCTION

The recent increased interest in the study [1–12] of polarized light propagation through turbid media derives from a variety of practical applications. Polarized light multiple scattered from a turbid medium carries information about the medium interior [13] such as, particle size and concentration, size distribution, and refractive index variation, which can be useful for biomedical imaging [13–15], endoscopic evaluation of biological tissues [16], investigation of biological cell differentiation [17,18], flow cytometry [18,19], lidar-based remote sensing of the atmospheric cloud, aerosol fog and smog [20,21], and imaging of targets in shallow coastal water [22]. Polarization-sensitive imaging has been demonstrated to enhance image contrast of targets embedded in turbid media [14,23].

In particular, it has been observed that for circularly polarized light, randomization of its polarization requires more scattering events than the randomization of its direction [23–27,6,9]. An important consequence of this "polarization memory" [25] is higher resolution and contrast of transillumination images recorded with copolarized light than those recorded with unpolarized or cross-polarized light. Another interesting feature is the dependence of the intensity of the backscattered copolarized and cross-polarized light on the size of the scatterers in the medium [23]. The backscattered light is dominated by light of helicity opposite to that of the incident light if the size of the scatterers is smaller than the wavelength of light. The light of the same helicity dominates when scatterers are larger than the light wavelength. These results have important consequences in the design considerations of imaging systems using backscattered light such as, endoscopic systems. All these developments make it impera-

tive that theoretical formalisms be developed to provide a quantitative explanation of the experimental results, and guidance for the design of imaging systems using polarized light.

Theoretical studies of polarized light propagation through a scattering medium commonly starts with the vector radiative transfer equation (VRTE) [1], and because of the inherent complexity of the problem, a limited number of studies are available to date. A majority of these studies focused on developing numerical solutions of the VRTE. Ishimaru and co-workers first investigated the propagation of continuous wave (CW), polarized wave normally incident on a medium with discrete scatterers using discrete ordinate methods to solve VRTE [2,3]. More recently, they extended the formalism to numerically solve the time-dependent VRTE to account for the propagation of polarized pulses [4]. Kim and Moscoso studied the propagation of a linearly polarized or circularly polarized continuous plane wave normally incident on a plane-parallel medium containing a random distribution of dielectric spheres, and numerically solved the one-dimensional VRTE using a Chebyshev spectral method [5]. The approach was subsequently modified to study the backscattering of circularly polarized plane-wave pulses [6]. Vallion *et al.* [7] used a vector Monte Carlo method to study polarized light transport through a semitransparent medium filled with scattering particles. Jiang *et al.* [8] developed a multilayer radiative transfer model that takes into account the state of polarization using the doubling-adding method for passive atmospheric remote sensing applications. More recently, Sakami and Dogariu [9] investigated the propagation of a polarized plane-wave pulse incident at any angle in a random medium using the discrete-ordinates method to

solve the VRTE, and used an angular analysis to obtain details of the polarization flip of circular polarized light. The problem of light scattering and radiative transfer in scattering media and its application to geophysical optics, image transfer, remote sensing, and inverse problems are discussed in the monograph by Kokhanovsky [10].

In this paper, we use the analytical solution of the time-dependent VRTE to compute backscattering of circularly polarized light in an infinite uniform scattering medium. It builds on the analytical cumulant approach for solving the time-dependent radiative transfer equation in an infinite uniform medium that we developed [28–30]. In this approach an arbitrary phase function, as long as it is a function of scattering angle, can be treated. We have derived the exact expression of spatial cumulants of photon distribution at any angle and any time, up to an arbitrary high order. The exact first spatial cumulant represents the center of the distribution and the exact second spatial cumulant represents the width of the distribution. The method of the analytical cumulant solution for the scalar radiative transfer equation can be extended to the vector (polarized) case [31]. In the analytical solution of VRTE, a transform to the circular representation from the Stokes representation of polarization is introduced, and the generalized spherical functions are used for angular expansion, instead of the standard spherical functions for solving the scalar radiative transfer equation. The expressions for the exact first and second spatial cumulants of polarized components as functions of angle **s** and time t is derived. Then, intensity of the polarized light is presented by a Gaussian spatial distribution. We apply this method to calculate the backscattering of circular polarized light in a scattering medium. The results show that circularly polarized light of the same helicity dominates the backscattered signal when scatterer size is larger than the wavelength of light. For the scatterers smaller than the wavelength, light of opposite helicity makes the dominant contribution to the backscattered signal. The theoretical conclusion is in good agreement with our experimental results [23].

The paper is organized as follows. In Sec. II we review the analytical solution of VRTE. In Sec. III, the numerical results are presented and are compared with experiments. Section IV is devoted to discussion and conclusion.

II. THEORETICAL FORMALISM

A. Polarized components of light

In the Stokes polarization representation [32] (SP), the polarized light is described by $\mathbf{I}^{SP}=[I,Q,U,V]$. The polarized components of distribution we will study are the parallel component $I_{\parallel}=(I+Q)/2$, the perpendicular component $I_{\perp}=(I-Q)/2$, the right-circular component $I_R=(I+V)/2$, and the left-circular component $I_L=(I-V)/2$, since these quantities are positive definite, and are experimentally measurable.

The vector radiative transfer equation for the polarized photon distribution function $\mathbf{I}(\mathbf{r},\mathbf{s},t)$ in an infinite uniform medium, illuminated by a point light source providing short pulse, $\mathbf{I}^{(0)}\delta(\mathbf{r}-\mathbf{r}_0)\delta(\mathbf{s}-\mathbf{s}_0)\delta(t-0)$ is given by [33]

$$\partial\mathbf{I}(\mathbf{r},\mathbf{s},t)/\partial t + c\mathbf{s}\cdot\nabla_{\mathbf{r}}\mathbf{I}(\mathbf{r},\mathbf{s},t) + \mu_a\mathbf{I}(\mathbf{r},\mathbf{s},t)$$
$$= \mu_s\int\mathbf{P}(\mathbf{s},\mathbf{s}')[\mathbf{I}(\mathbf{r},\mathbf{s}',t)-\mathbf{I}(\mathbf{r},\mathbf{s},t)]d\mathbf{s}'$$
$$+ \mathbf{I}^{(0)}\delta(\mathbf{r}-\mathbf{r}_0)\delta(\mathbf{s}-\mathbf{s}_0)\delta(t-0), \tag{1}$$

where vector $\mathbf{I}(\mathbf{r},\mathbf{s},t)$ has four polarization components, c is the light speed in the medium, μ_s is the scattering rate, μ_a is the absorption rate, and $\mathbf{P}(\mathbf{s},\mathbf{s}')$ is the 4×4 phase matrix. A meridian plane parallel to the z axis and the light direction **s**, is used as a plane of reference for the description of the polarization state. In SP the components Q,U vary with the rotation of the reference plane around the light propagation direction. With a rotation of reference plane through an angle $\alpha\geq0$ (in the counterclockwise direction, when looking in the direction of propagation) $\mathbf{I}^{SP}$ varies as $(\mathbf{I}')^{SP}=\mathbf{L}(\alpha)\mathbf{I}^{SP}$, where $\mathbf{L}(\alpha)$ is given by

$$\mathbf{L}(\alpha)=\begin{bmatrix} 1 & 0 & 0 & 0 \\ 0 & \cos2\alpha & \sin2\alpha & 0 \\ 0 & -\sin2\alpha & \cos2\alpha & 0 \\ 0 & 0 & 0 & 1 \end{bmatrix}. \tag{2}$$

When light propagates along the z direction, Q,U vary with the change of the azimuthal angle ϕ.

The phase matrix in the fixed coordinates is given by:

$$\mathbf{P}(\mathbf{s},\mathbf{s}') = \mathbf{L}(\pi-\chi)\mathbf{P}(\cos\Theta)\mathbf{L}(-\chi'), \tag{3}$$

where Θ is the angle between light rays before and after scattering in the scattering plane, and the matrices $\mathbf{L}(-\chi')$ and $\mathbf{L}(\pi-\chi)$ are those required to rotate meridian planes before and after scattering onto a local scattering plane. The intrinsic property of a scattering mechanism is described by the 4×4 scattering function $\mathbf{P}(\cos\Theta)$, which is assumed to depend only on $\cos\Theta=\mathbf{s}\cdot\mathbf{s}'$. It is convenient to use a representation of the polarized light in which $\mathbf{L}(\alpha)$ is diagonal, rather than Eq. (2). A circular polarization representation (CP), first proposed by Kuščer and Ribarič [34] and presented by Hovenier and van der Mee [35], is $\mathbf{I}^{CP}=[I_2,I_0,I_{-0},I_{-2}]$, where $I_0=(I+V)/2$, $I_{-0}=(I-V)/2$, $I_2=(Q+iU)/2$, and $I_{-2}=(Q-iU)/2$, or $\mathbf{I}^{CP}=\mathbf{T}\mathbf{I}^{SP}$, with

$$\mathbf{T}=\frac{1}{2}\begin{bmatrix} 0 & 1 & i & 0 \\ 1 & 0 & 0 & 1 \\ 1 & 0 & 0 & -1 \\ 0 & 1 & -i & 0 \end{bmatrix} \text{ and } \mathbf{T}^{-1}=\begin{bmatrix} 0 & 1 & 1 & 0 \\ 1 & 0 & 0 & 1 \\ -i & 0 & 0 & i \\ 0 & 1 & -1 & 0 \end{bmatrix}. \tag{4}$$

In CP a rotation of the reference plane through an angle α around the light direction causes I_m^{CP} to be multiplied by $\exp(-im\alpha)$, $m=2,0,0,-2$. Notice that I_0 and I_{-0} actually have the same rotational property. For the phase matrix, transform between two representations is $\mathbf{P}^{CP}=\mathbf{T}\mathbf{P}^{SP}\mathbf{T}^{-1}$.

In CP it is convenient to expand the phase matrix $\mathbf{P}^{CP}$ using the generalized spherical functions (GSF). The generalized spherical functions $P_{mn}^l(\beta)$ are related to the $d_{mn}^l(\beta)$

in the angular momentum theory [36] by $P_{m,n}^l(\beta)$ $=(i)^{m-n}d_{mn}^l(\beta)$. In the Appendix, the expressions for $d_{mn}^l(\beta)$ are presented.

B. Phase matrix using Mie theory

Elements of the CP phase matrix in the scattering plane, $P_{mn}^{CP}(\cos\Theta)$ can be expanded by GSF;

$$P_{mn}^{CP}(\cos\Theta) = \frac{1}{4\pi}\sum_l \rho_{mn}^l P_{m,n}^l(\cos\Theta), \qquad (5)$$

with $m,n=2,0,-0,-2$, and $l \geq \max(|m|,|n|)$. The coefficients ρ_{mn}^l provide a description of the scattering mechanism. In most useful cases, the coefficients ρ_{mn}^l have properties: (i) $\rho_{mm}^l = \rho_{m-m}^l$ are real; (ii) $\rho_{mn}^l = \rho_{nm}^l = \rho_{-m-n}^l$; (iii) $\rho_{20}^l = [\rho_{2-0}^l]^*$ (* means complex conjugate). Therefore, for each $l \geq 2$, there are six independent real elements: ρ_{00}^l, ρ_{22}^l, ρ_{0-0}^l, ρ_{2-2}^l, $\mathrm{Re}[\rho_{20}^l]$, and $\mathrm{Im}[\rho_{20}^l]$. For $l=0,1$, only ρ_{00}^l and ρ_{0-0}^l are nonzero. These numerical coefficients can be calculated using the Mie theory for a spherical particle. We have $\rho_{00}^l = (\alpha_1^l + \alpha_4^l)/2$, $\rho_{0-0}^l = (\alpha_1^l - \alpha_4^l)/2$, $\rho_{22}^l = (\alpha_2^l + \alpha_3^l)/2$, $\rho_{2-2}^l = (\alpha_2^l - \alpha_3^l)/2$, $\mathrm{Re}[\rho_{20}^l] = \beta_1^l$, $\mathrm{Im}[\rho_{20}^l] = \beta_2^l$, where the coefficients $\alpha_{1,2,3,4}^l$ and $\beta_{1,2}^l$ are formulated in Eqs. (4.81)–(4.86) in Ref. [37].

C. Photon angular distribution F(s,s₀,t)

When we make a spherical harmonics expansion of Eq. (1), the difficulty is that the term $c\mathbf{s}\cdot\nabla_r\mathbf{I}(\mathbf{r},\mathbf{s},t)$ couples equations of different harmonics. We first study the photon distribution in the angular space in CP initially incident along $\mathbf{s}_0$,

$$\mathbf{F}(\mathbf{s},\mathbf{s}_0,t) = \int \mathbf{I}(\mathbf{r},\mathbf{s},t)d\mathbf{r}, \qquad (6)$$

where integration is over the whole space. Evaluation of the integral in Eq. (6) over Eq. (1) leads to

$$\partial\mathbf{F}(\mathbf{s},\mathbf{s}_0,t)/\partial t + \mu_a\mathbf{F}(\mathbf{s},\mathbf{s}_0,t)$$
$$+ \mu_s\left[\mathbf{F}(\mathbf{s},\mathbf{s}_0,t) - \int \mathbf{P}(\mathbf{s},\mathbf{s}')\mathbf{F}(\mathbf{s}',\mathbf{s}_0,t)d\mathbf{s}'\right]$$
$$= \mathbf{I}^{(0)}\delta(\mathbf{s}-\mathbf{s}_0)\delta(t-0). \qquad (7)$$

The gradient term disappears in Eq. (7) because of the Gauss-Stokes law. Hence, $\mathbf{F}(\mathbf{s},\mathbf{s}_0,t)$ can be exactly solved by expanding in GSF's. When $\mathbf{s}_0$ is set along the z direction, the initial polarization state is set as n_0, and the initial reference plane is set as the x-z plane, we have

$$F_{mn_0}(\mathbf{s},\mathbf{s}_0,t) = \sum_l \left[F_{mn_0}^l(t)P_{m,n_0}^l(\cos\theta)\right.$$
$$\left. - \delta_{m,n_0}\frac{2l+1}{4\pi}e^{-\mu_s t}P_{0,0}^l(\cos\theta)\right]$$
$$\times \exp(-in_0\phi)\exp(-\mu_a t), \qquad (8)$$

where $\mathbf{s}=(\theta,\phi)$, and $m,n_0=2,0,-0,-2$, $l \geq \max(|m|,|n_0|)$. The second term in Eq. (8) represents the ballistic (unscattered) component of photons. $F_{mn_0}^l(t)$ in Eq. (8) is the solution of the equation

$$dF_{mn_0}^l(t)/dt = \sum_n \Pi_{mn}^l F_{nn_0}^l(t), \qquad (9)$$

under the initial condition

$$F_{mn_0}^l(t=0) = \delta_{m,n_0}(2l+1)/4\pi, \qquad (10)$$

where $\Pi_{mn}^l = \mu_s[\delta_{m,n} - \rho_{mn}^l/(2l+1)]$. The solution $F_{mn_0}^l(t)$ has the following form:

$$F_{mn_0}^l(t) = \frac{2l+1}{4\pi}\sum_i [B_{mn_0}^l]_i \exp(-\lambda_i^l t), \qquad (11)$$

$i=1,2,3,4$ for $l \geq 2$, and $i=1,2$ for $l=1,2$. The eigenvalues λ_i^l for $l \geq 2$ is given by

$$\lambda_i^l = (1/2)\left\{(\Pi_{00}^l + \Pi_{22}^l \pm \Pi_{0-0}^l \pm \Pi_{2-2}^l)\right.$$
$$+ \left[(\Pi_{00}^l - \Pi_{22}^l \pm \Pi_{0-0}^l \mp \Pi_{2-2}^l)^2\right.$$
$$\left.\left. \pm 16\binom{\mathrm{Re}[\Pi_{20}^l]}{\mathrm{Im}[\Pi_{20}^l]}^2\right]^{1/2}\right\}, \qquad (12)$$

for $i=1,2$, and for $i=3,4$, the sign $+$ before the square brackets in Eq. (12) is replaced by $-$. For $l=0,1$ two eigenvalues are $\lambda_i^l = \Pi_{00}^l \pm \Pi_{0-0}^l$. The constant coefficients $[B_{mn_0}^l]_i$ can be determined using linear algebra under the initial condition Eq. (10) [31].

In SP the angular distribution component of $I_m = [I,Q,U,V]$, with the initial polarized state $\mathbf{I}^{SP(0)}$, is obtained by

$$F_m^{SP}(\mathbf{s},\mathbf{s}_0,t) = [\mathbf{T}^{-1}\mathbf{F}(\mathbf{s},\mathbf{s}_0,t)\mathbf{T}\mathbf{I}^{SP(0)}]_m. \qquad (13)$$

The angular distribution for the parallel polarized component is given by $F_\parallel(\mathbf{s},\mathbf{s}_0,t) = [F_I^{SP}(\mathbf{s},\mathbf{s}_0,t) + F_Q^{SP}(\mathbf{s},\mathbf{s}_0,t)]/2$. Similarly, we have $F_\perp = (F_I^{SP} - F_Q^{SP})/2$, $F_R = (F_I^{SP} + F_V^{SP})/2$, and $F_L = (F_I^{SP} - F_V^{SP})/2$.

D. The cumulant expansion

The polarized photon distribution $I_m(\mathbf{r},\mathbf{s},t)$ in an infinite uniform medium can be written as [31]

$$I_m(\mathbf{r},\mathbf{s},t) = \left\langle \delta\left(\mathbf{r} - c\int_0^t \mathbf{s}(t')dt'\right)\delta[\mathbf{s}(t)-\mathbf{s}]\right\rangle_m, \qquad (14)$$

where $\langle\cdots\rangle$ means the ensemble average in the angular space. We perform a Fourier transform of the first δ function, then make a cumulant expansion, and obtain

$$I_m(\mathbf{r},\mathbf{s},t) = F_m(\mathbf{s},\mathbf{s}_0,t) \frac{1}{(2\pi)^3} \int d\mathbf{q} \exp\left\{i\mathbf{q}\cdot\mathbf{r}\right.$$

$$+ \sum_{k=1}^{\infty} \frac{(-ic)^k}{k!} \sum_{j_k} \cdots \sum_{j_1} q_{j_k} \cdots q_{j_1}$$

$$\times \left[\left\langle \int_0^t dt_k \cdots \int_0^t dt_1 T[s_{j_k}(t_k) \cdots s_{j_1}(t_1)] \right\rangle_c \right]_m \right\}, \tag{15}$$

where T denotes time-ordered multiplication [38], and the subscript-index c denotes cumulant. The cumulants are related to the moments. For an arbitrary random variable A, we have $\langle A \rangle_c = \langle A \rangle$, $\langle A^2 \rangle_c = \langle A^2 \rangle - \langle A \rangle\langle A \rangle$, and so on. The corresponding moment can be estimated using a standard time-dependent Green's-function approach, which is given by

$$\left[\left\langle \int_0^t dt_k \cdots \int_0^t dt_1 T[s_{j_k}(t_k) \cdots s_{j_1}(t_1)] \right\rangle\right]_m$$

$$= \frac{1}{F_m(\mathbf{s},\mathbf{s}_0,t)} \left\{\left[\left[\int_0^t dt_k \int_0^{t_k} dt_{k-1} \cdots \int_0^{t_2} dt_1 \int d\mathbf{s}^{(k)}\right.\right.\right.$$

$$\times \int d\mathbf{s}^{(k-1)} \cdots \int d\mathbf{s}^{(1)} \mathbf{F}(\mathbf{s},\mathbf{s}^{(k)},t-t_k)s_{j_k}^{(k)}$$

$$\times \mathbf{F}(\mathbf{s}^{(k)},\mathbf{s}^{(k-1)},t_k-t_{k-1})s_{j_{k-1}}^{(k-1)} \cdots \mathbf{F}(\mathbf{s}^{(2)},\mathbf{s}^{(1)},t_2-t_1)s_{j_1}^{(1)}$$

$$\left.\left.\times \mathbf{F}(\mathbf{s}^{(1)},\mathbf{s}_0,t_1-0)\mathbf{I}^{(0)}\right]_m + (\text{perm})\right\}, \tag{16}$$

where the abbreviation "perm" means all $k! - 1$ terms obtained by permutation of $\{j_i\}$, $i=1,\ldots,k$ from the first term, and $\mathbf{F}(\mathbf{s}^{(i)},\mathbf{s}^{(i-1)},t_i-t_{i-1})$ is the exact solution given by Eq. (8) in Sec. II C. If we cut off the summation in Eq. (15) at $k=2$, the integration leads to a Gaussian spatial distribution characterized by the first and second cumulants.

1. First cumulant (center of the spatial distribution)

In CP it is convenient to set $\mathbf{s}$ in a spherical harmonic basis,

$$\mathbf{s} = [s_1,s_0,s_{-1}] = [-2^{-1/2}\sin\theta e^{+i\phi}, \cos\theta, +2^{-1/2}\sin\theta e^{-i\phi}], \tag{17}$$

which is related to Cartesian component basis $\alpha=x,y,z$ by $s_\alpha = \sum U_{\alpha j}s_j$, $j=1,0,-1$ with

$$U = 2^{-1/2}\begin{bmatrix} -1 & 0 & 1 \\ i & 0 & i \\ 0 & 2^{1/2} & 0 \end{bmatrix}. \tag{18}$$

Using the recurrence relation and the orthogonality relation of GSF, the unnormalized first moment in CP, when $\mathbf{s}_0$ is along the z direction, is obtained;

$$\langle \mathbf{R}_j \rangle_{mn_0} = c\int_0^t dt' \int d\mathbf{s}' \sum_n F_{mn}(\mathbf{s},\mathbf{s}',t-t')s_j' F_{nn_0}(\mathbf{s}',\mathbf{s}_0,t')$$

$$= c\sum_l \left\{ P_{m,n_0-j}^l(\cos\theta)e^{-i(n_0-j)\phi}\gamma_j \sum_n \sum_h \frac{2(l-h)+1}{4\pi}\right.$$

$$\times D_{m,n,n_0}^{l,h}(t)\langle l-h,1,n,0|l,n\rangle\langle l-h,1,n_0,-j|l,n_0-j\rangle$$

$$\left. - \delta_{j,0}\delta_{m,n_0}\frac{2l+1}{4\pi}te^{-\mu_s t}P_{0,0}^l(\cos\theta)e^{-in_0\phi}\right\}, \tag{19}$$

with $\gamma_{\pm 1} = \mp i$, $\gamma_0 = 1$, $\langle l_1,l_2,m_1,m_2|L,M\rangle$ is Clebsch-Gordan coefficients in angular momentum theory [36], presented in the Appendix, and

$$D_{m,n,n_0}^{l,h}(t) = \sum_{i,j} [B_{mn}^l]_i [B_{nn_0}^{l-h}]_j \left(\frac{\exp(-\lambda_j^{l-h}t) - \exp(-\lambda_i^l t)}{\lambda_i^l - \lambda_j^{l-h}}\right)$$

$$\times \exp(-\mu_a t), \tag{20}$$

where $i,j=1,2,3,4$ for $l \geq 2$, and $i,j=1,2$ for $l=1,2$.

In SP the component of the unnormalized first moment of $I_m = [I,Q,U,V]$, with the initial polarized state $\mathbf{I}^{SP(0)}$, and $\alpha = x,y,z$, is obtained by

$$\langle \mathbf{R}_\alpha \rangle_m^{SP} = \sum_j U_{\alpha j}[\mathbf{T}^{-1}\langle \mathbf{R}_j \rangle \mathbf{T} \mathbf{I}^{SP(0)}]_m. \tag{21}$$

The center of photon distribution for the linearly polarized components is obtained by

$$R_{p,\alpha}^c(\mathbf{s},t) = \frac{[\langle \mathbf{R}_\alpha \rangle_I^{SP} \pm \langle \mathbf{R}_\alpha \rangle_Q^{SP}]}{2F_p(\mathbf{s},\mathbf{s}_0,t)}, \tag{22}$$

where the $+$ sign holds for the $p=\parallel$ component, and the $-$ sign holds for the $p=\perp$ component. The center of photon distribution for the circularly polarized components is obtained by

$$R_{c,\alpha}^c(\mathbf{s},t) = \frac{[\langle \mathbf{R}_\alpha \rangle_I^{SP} \pm \langle \mathbf{R}_\alpha \rangle_V^{SP}]}{2F_c(\mathbf{s},\mathbf{s}_0,t)}, \tag{23}$$

where the $+$ sign holds for the $c=R$ component, and the $-$ sign holds for the $c=L$ component.

2. Second cumulant (width of the spatial distribution)

Similarly, we can obtain the expression for the unnormalized second moment in CP,

$$\langle \mathbf{R}_{j_2} \mathbf{R}_{j_1} \rangle_{mn_0} = c^2 \sum_l \left\{ P_{m,n_0-j_1-j_2}^l (\cos\theta) e^{-i(n_0-j_1-j_2)\phi} \gamma_{j_2} \gamma_{j_1} \sum_{n_2} \sum_{n_1} \sum_{h_2} \sum_{h_1} \frac{2(l-h_2-h_1)+1}{4\pi} \right.$$

$$\times E_{m,n_2,n_1,n_0}^{l,h_2,h_1}(t) \langle l-h_2,1,n_2,0|l,n_2 \rangle \langle l-h_2,1,n_0-j_1,-j_2|l,n_0-j_1-j_2 \rangle \langle l-h_2-h_1,1,n_1,0|l-h_2,n_1 \rangle$$

$$\left. \times \langle l-h_2-h_1,1,n_0,-j_1|l-h_2,n_0-j_1 \rangle - \delta_{j_2,0}\delta_{j_1,0}\delta_{m,n_0} \frac{2l+1}{4\pi} \frac{t^2}{2} e^{-\mu_s t} P_{0,0}^l(\cos\theta) e^{-in_0\phi} \right\}, \tag{24}$$

with

$$E_{m,n_2,n_1,n_0}^{l,h_2,h_1}(t) = \sum_{i,j,f} [B_{mn_2}^l]_i [B_{n_2n_1}^{l-h_2}]_j [B_{n_1n_0}^{l-h_2-h_1}]_f \exp(-\mu_a t)$$

$$\times \left(\frac{\exp(-\lambda_f^{l-h_2-h_1}t) - \exp(-\lambda_i^l t)}{(\lambda_j^{l-h_2} - \lambda_f^{l-h_2-h_1})(\lambda_i^l - \lambda_f^{l-h_2-h_1})} \right.$$

$$\left. - \frac{\exp(-\lambda_j^{l-h_2}t) - \exp(-\lambda_i^l t)}{(\lambda_j^{l-h_2} - \lambda_f^{l-h_2-h_1})(\lambda_i^l - \lambda_j^{l-h_2})} \right), \tag{25}$$

where $i,j,f = 1,2,3,4$ for $l \geq 2$, and $i,j,f = 1,2$ for $l = 1,2$.

In SP the component of the unnormalized second moment of $I_m = [I,Q,U,V]$, with the initial polarized state $\mathbf{I}^{SP(0)}$, is obtained by

$$\langle \mathbf{R}_\alpha \mathbf{R}_\beta \rangle_m^{SP} = \sum_{j_1} \sum_{j_2} \frac{1}{2} (U_{\alpha j_1} U_{\beta j_2} + U_{\alpha j_2} U_{\beta j_1})$$

$$\times [\mathbf{T}^{-1} \langle \mathbf{R}_{j_2} \mathbf{R}_{j_1} \rangle \mathbf{T} \mathbf{I}^{SP(0)}]_m. \tag{26}$$

The square of the width of the photon distribution for the linearly polarized component is determined by

$$D_{p,\alpha\beta}(\mathbf{s},t) = \frac{[\langle \mathbf{R}_\alpha \mathbf{R}_\beta \rangle_I^{SP} \pm \langle \mathbf{R}_\alpha \mathbf{R}_\beta \rangle_Q^{SP}]}{2F_\parallel(\mathbf{s},\mathbf{s}_0,t)} - \frac{1}{2} R_{p,\alpha}^c R_{p,\beta}^c, \tag{27}$$

where the $+$ sign holds for the $p=\parallel$ component, and the $-$ sign holds for the $p=\perp$ component. The square of the width of photon distribution for the circularly polarized components is obtained by

$$D_{c,\alpha\beta}(\mathbf{s},t) = \frac{[\langle \mathbf{R}_\alpha \mathbf{R}_\beta \rangle_I^{SP} \pm \langle \mathbf{R}_\alpha \mathbf{R}_\beta \rangle_V^{SP}]}{2F_c(\mathbf{s},\mathbf{s}_0,t)} - \frac{1}{2} R_{c,\alpha}^c R_{c,\beta}^c, \tag{28}$$

where the $+$ sign holds for the $c=R$ component, and the $-$ sign holds for the $c=L$ component.

F. Gaussian distribution of the polarized light

Polarized photon intensity $I_\nu(\mathbf{r},\mathbf{s},t)$, $\nu=\parallel,\perp,R,L$, is expressed by an approximate Gaussian distribution,

$$I_\nu(\mathbf{r},\mathbf{s},t) = \frac{F_\nu(\mathbf{s},\mathbf{s}_0,t)}{(4\pi)^{3/2}} \frac{1}{[\det D_\nu]^{1/2}} \exp\left\{ \sum_{\alpha\beta} -\frac{1}{4} [(D_\nu)^{-1}]_{\alpha\beta} \right.$$

$$\left. \times (r_\alpha - R_{\nu,\alpha}^c)(r_\beta - R_{\nu,\beta}^c) \right\}. \tag{29}$$

The ballistic component has been subtracted in the expressions for the angular distribution Eq. (8), for the first cumulant Eq. (19), and for the second cumulant, Eq. (24). This subtraction ensures that the summation over l converges even at very early times, as discussed in Sec. III of Ref. [30].

In the case of the transmission of light, the formalism produces the correct first and second cumulants, but the Gaussian-shaped distribution obtained for early times violates causality, as manifested by the photons at the front edge of the distribution traveling faster than the speed of light in free space. We have introduced an approach to reshape the distribution in Ref. [30], which maintains the correct center position and width of spread of the distribution, and satisfies the causality condition. This technique can be extended to include polarization, combining the formula for the calculation of cumulants of polarized components, in the study of transmission of linear and circular polarized light.

III. RESULT

A. Theoretical result

We now use the formalism developed in Sec. II to study backscattering of circularly polarized light in a scattering medium. A right circularly polarized beam of light with initial Stokes parameters $I=[1,0,0,1]$ and wavelength $\lambda = 610$ nm is assumed to be injected into an infinite medium comprised of polystyrene spheres (with refractive index $m = 1.59$) suspended in water (with refractive index $m_0 = 1.33$). The absorption coefficient of light in the medium is assumed to be zero. The light is incident along the z axis from the origin $(x,y,z) = (0,0,0)$. The backscattered light is received by a detector located at $(x_d,0,0)$. Figure 1 shows the computed time-resolved profiles of circularly polarized backscattered light as a function of time t (in a unit of l_{tr}/c), collected at direction $\theta=180°$ and position $x_d=0.5l_{tr}$, where l_{tr} is the transport mean free path, for polystyrene spheres of diameter (a) $d=0.10$ μm, (b) $d=0.213$ μm, (c) $d=0.855$ μm, and (d) $d=8.0$ μm. A remarkable feature is that the backscattered signal is dominated by the left circular polarized (LCP) light if the size of scatterers is small compared to the wavelength of light, as shown in Figs. 1(a) and 1(b), but it is dominated by the right circular polarized (RCP) light if the size of scatterers is large, as displayed in Figs. 1(c) and 1(d). Figure 2 shows how the peak intensity of RCP light and LCP light vary with the size of scatterers.
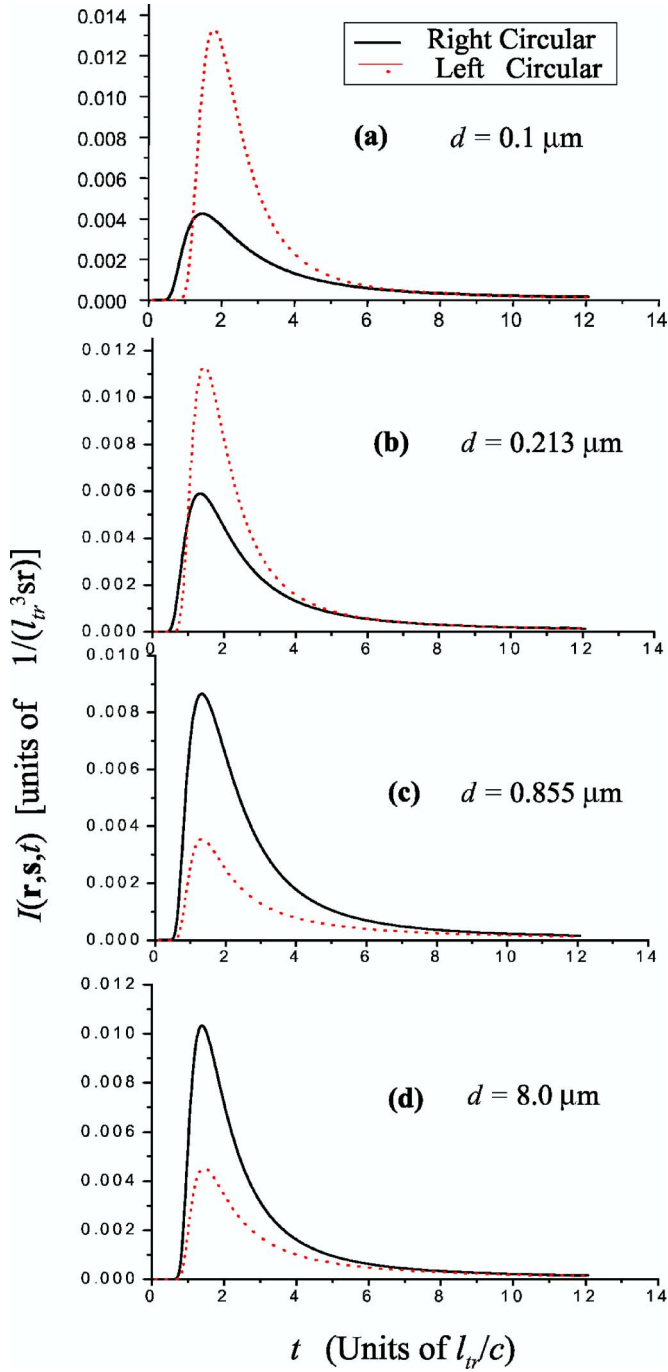
FIG. 1. (Color online) Time-resolved profiles of RCP (solid curve) and LCP (dotted curve) backscattered light intensity as functions of time t (in the unit of l_{tr}/c), received at angle $\theta=180°$ and detector position $x_d=0.5l_{tr}$, where l_{tr} is the transport mean free path, for different diameters of scatterers: (a) $d=0.10\ \mu$m, (b) $d=0.213\ \mu$m, (c) $d=0.855\ \mu$m, and (d) $d=8.0\ \mu$m. The initial Stokes parameters $\mathbf{I}=[1,0,0,1]$ represent a RCP light beam incident along the z direction, and the wavelength $\lambda=610$ nm.

We explain this phenomenon by considering the effect of Mie single scattering together with the effect of multiple scattering. The Mie formula indicates that when $m/m_0 =1.19$, for small particles the Stokes V component is negative for θ larger than 90°, which means that the helicity of
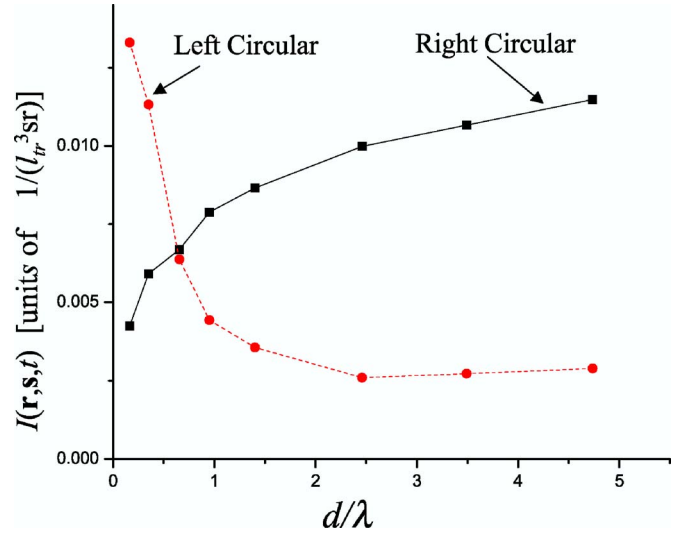
FIG. 2. (Color online) The peak intensity of the time-resolved profile of RCP and LCP backscattered light as functions of d/λ, at angle $\theta=180°$ and detector position $x_d=0.5l_{tr}$. The incident beam is RCP.

light singly backscattered from a small particle will flip. As the particle size increases, the helicity of the near-backward scattered light computed using Mie formula becomes oscillating, and the region of negative V squeezes to a range near $\theta=180°$. For near-forward scattering, the value of V is positive, hence, the helicity does not flip. For large particles the anisotropy factor g is large, and the probability of near-forward scattering is high. For large particles compared to λ, backscattering results from the accumulated effect of many small-angle (near-forward) scattering events, each of which changes the direction only slightly. These small-angle scattering events do not change the helicity of circularly polarized light. Hence, the backscattered light is dominated by the component that maintains the original helicity. When particles are small, however, the events with large-angle scattering play a more important role. The backscattered light is dominated by the component with the flipped helicity.

In view of the above explanation, it is expected that circularly polarized light with reversed helicity dominates only when the detector is located close to the source. When the distance between the source and the detector becomes large, more backscattered photons come from the accumulation of many small-angle scattering events, and those retain the original helicity. Figure 3 shows the computed time-resolved profiles at different source-detector distances: (a) $x_d=0.1l_{tr}$, (b) $x_d=0.2l_{tr}$, (c) $x_d=1.0l_{tr}$ for a fixed-particle diameter, $d =0.7\ \mu$m, and detection angle $\theta=180°$. We see that the dominant component changes from LCP to RCP as the source-detector distance increases. Figure 4 shows the back-scattered time profiles for different detection angles: (a) $\cos\theta=-1$, (b) $\cos\theta=-0.9$, (c) $\cos\theta=-0.8$, for particle diameter $d=0.855\ \mu$m and the source-detector distance $x_d=1.0l_{tr}$. While total intensity increases with a decrease of angle θ, the RCP component remains dominant, which indicates that the helicity of backscattered light is not sensitive to the angle.
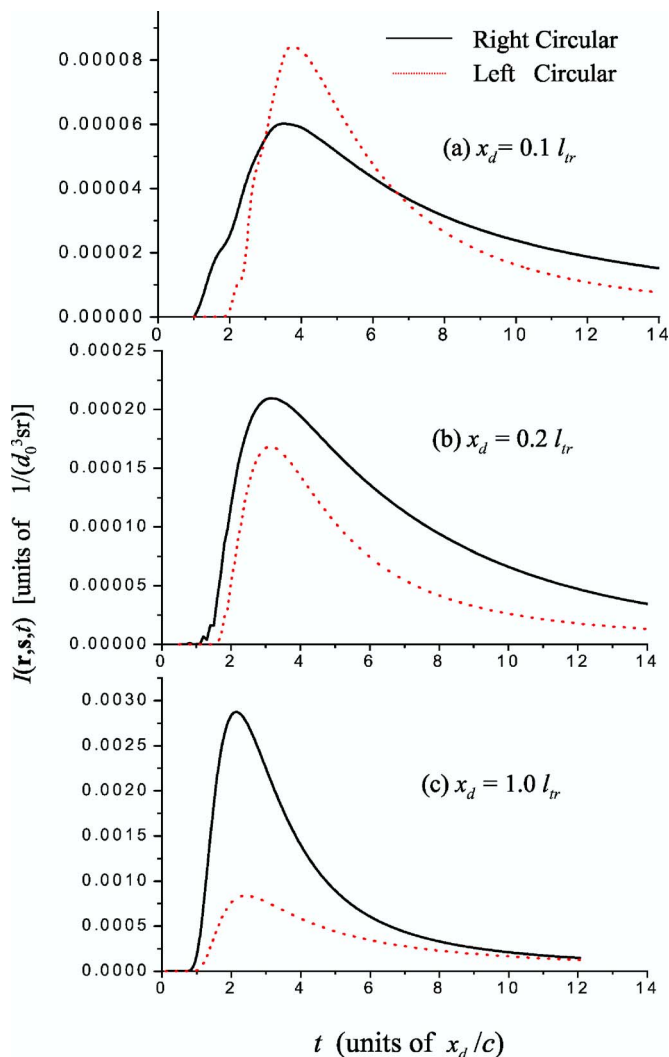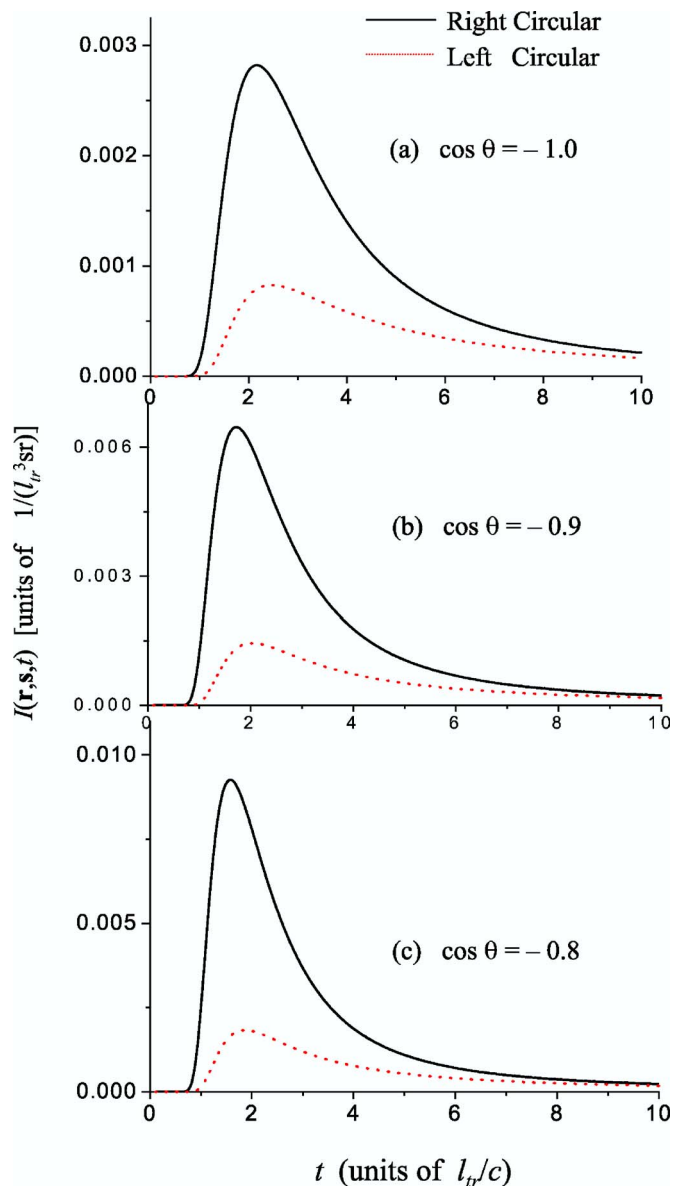
FIG. 3. (Color online) Time-resolved profiles of RCP (solid curve) and LCP (dotted curve) backscattered light as functions of time t, at different source-detector distances: (a) $x_d=0.1l_{tr}$, (b) $x_d=0.2l_{tr}$, (c) $x_d=1.0l_{tr}$, for particle diameter $d=0.7$ μm, the detection angle $\theta=180°$, and the wavelength $\lambda=610$ nm. The incident beam is RCP.

B. Comparison with experiments

We compare the above theoretical result with that of our experiments [23]. The setup for the time-resolved backscattering experiment is schematically shown in Fig. 5. The sample comprises polystyrene spheres suspended in deionized water in a $6\times6\times10$ cm³ glass cell. Ultrashort light pulses of 100 fs duration are generated at a repetition rate of 82 MHZ with wavelength $\lambda=610$ mn by a colliding pulse mode-locked dye laser. A quarter-wave plate is used to obtain RCP light. Time-resolved circularly polarized backscattered light is monitored by a 2 ps resolution streak camera.

Figure 6 shows the time-resolved profiles of backscattered light measured separately, with (a) small particles $d=0.213$ μm ($g=0.389$), scattering coefficients $\mu_s/c=0.61$ cm⁻¹ ($l_{tr}=2.68$ cm), and (b) large particles $d=8.0$ μm ($g=0.911$), scattering coefficients

FIG. 4. (Color online) Time-resolved profiles of RCP (solid curve) and LCP (dotted curve) backscattered light as functions of time t, at different angles: (a) $\cos\theta=-1$, (b) $\cos\theta=-0.9$, (c) $\cos\theta=-0.8$, for the particle's diameter $d=0.855$ μm, the detector position $x_d=1.0l_{tr}$, and the wavelength $\lambda=610$ nm. The incident beam is RCP.

$\mu_s/c=0.61$ cm⁻¹ ($l_{tr}=18.42$ cm). The detected backscattered light is dominated by the LCP (dotted curve) for small particles in case (a), but it is dominated by the RCP (solid curve) for large particles in case (b), even though the average x_d/l_{tr} for case (b) is much smaller than that for case (a). Figure 7 shows a comparison of normalized circularly polarized intensity of theoretical and experimental results for the case of $d=8.0$ μm ($d/\lambda=13.11$). Considering the differences between the theoretical parameters and the experimental setup (not an infinite medium, uncertainty in source-detector distance) theoretical predictions are in reasonable agreement with the experimental result.
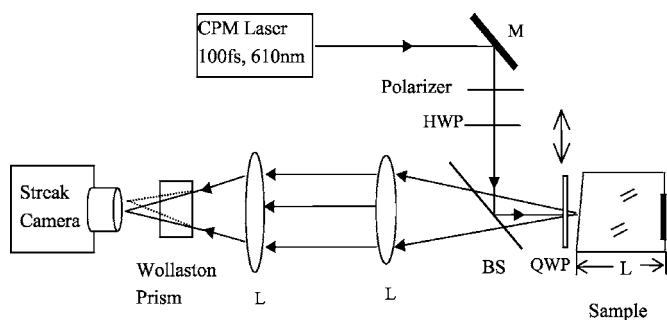
FIG. 5. Schematic diagram of the experimental setup for the time-resolved polarized backscattering measurement (BS=beam splitter, L=lens, M=mirror).

IV. DISCUSSION

A detailed theoretical formalism for the calculation of the distribution of polarized light intensity scattered from an infinite uniform turbid medium has been presented. The formalism is based on an analytical cumulant solution of the vector radiative transfer equation for an arbitrary phase matrix. It is then specialized for a phase matrix obtained from the Mie theory since many practical applications deal with Mie-scattering cases. The scattered polarized photon distri-
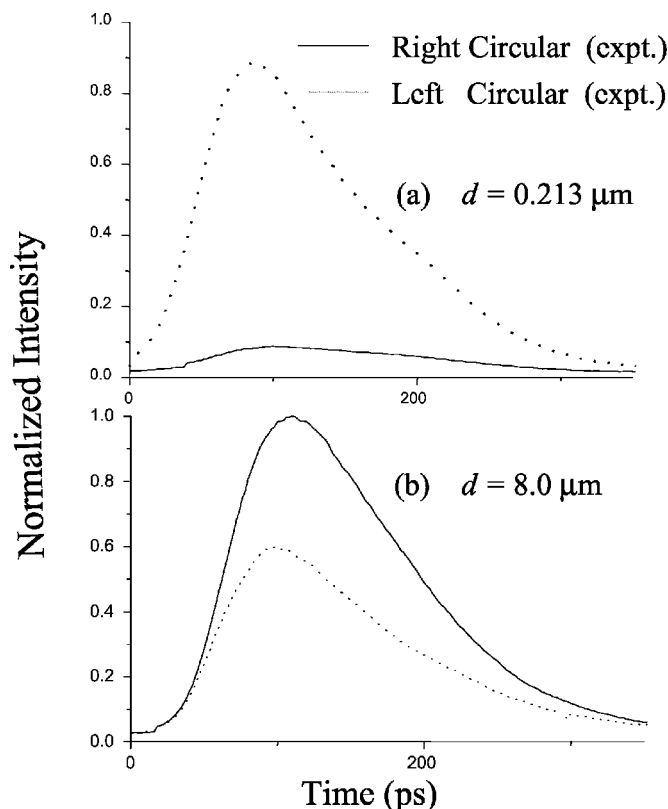
FIG. 6. The experimental time-resolved profiles of RCP (solid curve) and LCP (dotted curve) backscattered light as functions of time t for (a) small particles $d=0.213$ μm ($g=0.389$), the scattering coefficients $\mu_s/c=0.61$ cm^{-1} ($l_{tr}=2.68$ cm), (b) large particles $d=8.0$ μm ($g=0.911$), $\mu_s/c=0.61$ cm^{-1} ($l_{tr}=18.42$ cm). The incident beam is RCP.
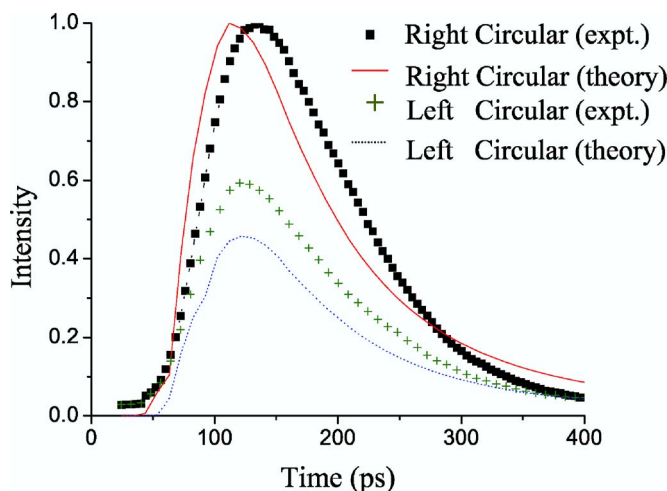
FIG. 7. (Color online) Comparison of theoretical and experimental results of normalized circular polarized light intensity for the medium with a particle diameter $d=8.0$ μm and wavelength $\lambda=610$ nm. The incident beam is RCP.

bution depends on the size of the scatterers, the distance between the light source and the detector, as well as, on the detection angle.

The advantage of the analytical cumulant solution is that it enables the fast and accurate calculation of the temporal profile of scattered polarized photon distribution. The use of Stoke's representation allows the investigation of light of any polarization state, including linear polarization and circular polarization, which are commonly used in practical applications. We have used a collimated ultrashort input pulse in our formalism, which represents the experimental conditions using picosecond and femtosecond lasers more closely than the plane wave cases used by earlier works [1–6,8,9]. In our formalism, the linear polarization case is handled by setting the initial Stokes vector as [1, 1, 0, 0]. Our initial results for linear polarization are in good agreement with earlier results [4,5].

In this paper, the focus has been on the calculation of circularly polarized light intensity in the backscattering geometry. The formalism enables the calculation of the intensity distribution of multiple backscattered light components that are copolarized and cross polarized with the incident beam for different angles of detection and for different source-detector positions. It is applicable for the analysis of three-dimensional spatially resolved measurements of characteristics of scattering media, such as satellite-based lidar measurements of clouds and aerosols. The approaches using a plane-wave incident beam calculate the backscattered photon flux at the plane of incidence ($z=0$ plane), and simplify the three-dimensional probing problem as a one-dimensional problem [2–6,8,9]. The approaches using Monte Carlo simulation can also handle three-dimensional spatially resolved measurements, but require a long computation time [7,39,40].

Once the copolarized and cross-polarized scattered intensity distributions are calculated, parameters, such as the degree of polarization and image contrast can be readily calculated to take advantage of the polarization memory effect

[25]. One of the results of this work elucidates the dependence of the relative intensities of the backscattered copolarized and cross-polarized light on the size of the scatterers in the turbid medium. We find that when the incident light is right circularly polarized, the backscattered signal is dominated by LCP light if the size of scatterers is smaller than the wavelength of light, but it is dominated by RCP light if the scatterer size is larger than the wavelength of light. The conclusion is in good agreement with our experimental results [23]. The dependence of the helicity of circularly polarized backscattered light on the scatterer size, and the polarization memory effect have been investigated by other authors [6,9,25–27,41]. Mackintosh *et al.* [25] experimentally demonstrated the polarization memory effect for spherical particles suspended and undergoing Brownian motion in a liquid by fitting a simple diffusion-based model to account for temporal correlations of the intensity fluctuations for different polarization channels. The theoretical estimation of backscattering of the circular polarized light using the numerical solution of the VRTE has been performed by Kim and Moscoso [6], as well as Sakami and Dogariu [9], which has been mentioned earlier in the Introduction. Phillips *et al.* [41] used an electric-field Monte Carlo method to study the backscattering of circularly polarized beams normally incident on a half space of scattering particles and found that the backscattered light of the same helicity formed a ring centered on the point of incidence. A Monte Carlo approach has been used by other researchers as well [7,39,40]. Xu and Alfano [27] used a random-walk approach to analytically estimate the characteristic depolarization length, which is obtained as an average over the entire detection solid angle. All these approaches converge on the general result that the circularly polarized light of the same helicity dominates backscattering when the scatterer size is larger than the light wavelength, as does the formalism presented in this paper and experimental results [23]. The salient feature of this work is that it provides an analytical approach for the calculation of polarized scattered light intensity, an experimentally measurable quantity, as a function of time, detection angle, and source-detector separation.

The dependence of the polarized backscattered light on the size of the scatterers in the medium has many potential applications, including biomedical imaging [13–15], flow cytometry [18,19], investigation of biological cell differentiation [17,18], subsurface imaging of cracks and corrosion below paint layers [42,43], lidar-based remote sensing of investigation of cloud and aerosol distribution in atmosphere [20,21], and the imaging of targets in turbid water [22].

Biomedical and biophysical applications represent an increasingly important area of application of polarized light scattering. As early as 1976, polarized light scattering was identified as a "new biophysical tool" [6]. The scatterers in biological materials include cells, cell nuclei, mitochondria that are in the Mie scattering domain (typical size varies from $5-20$ μm as compared to the wavelength of light in the visible to NIR of $0.5-1.5$ μm). Polarization effects in scattered light have been used to study bacterial suspensions in water [16,19], distinguish between a number of leukocyte types in flow cytometry [44,18], cell differentiation [17], and polynucleosome superstructures [45]. It has recently been shown experimentally that backscattered light may be analyzed to obtain information about the size distribution of the cell nuclei [15,46], which in turn could be useful for cancer detection as the cell nucleus size, shape, and distribution changes with cancer progression. In biomedical imaging applications polarization effects in scattering have been shown to be useful in examining skin [47], and subsurface structures in the prostate and other tissues [48].

Another important area of application of polarized light scattering is the remote sensing of the atmosphere and earth. Radar technology, the workhorse for remote sensing of the earth and the atmosphere, makes use of radio waves and its depolarization to obtain information about remote targets and ground flora [49]. While single-scattering approximation of radio waves is reasonable for radar applications [1], for probing of dense cloud, fog, and aerosols in the atmosphere, multiple scattering of light needs to be considered, which the formalism developed in this article does. Different scatterers in the atmosphere have varied size distributions [1,50], such as cloud and fog droplets (radii generally <100 μm, mean radii typically $2.5-5$ μm), aerosols (typically <1 μm), and hydrometeors (typically 1 μm or higher). Lidar-based investigation of cloud, aerosols, and other atmospheric scatterers employ visible and near-infrared light (typically 532 nm and 1064 nm) [20,51]. Scatterer size to wavelength ratio the dictates the use of Mie theory for the study of light scattering by clouds and aerosols. In the CALIPSO (Cloud-Aerosol Lidar and Infrared Pathfinder Satellite Observations) mission of NASA [51] one of the tasks involves probing with linearly polarized 532 nm and 1064 nm nanosecond duration pulses and the analysis of the temporal profiles of backscattered light for assessing the vertical distribution of clouds and aerosols in the atmosphere. Pal and Carswell [21] have observed spatial variations in the polarization properties of multiple-scattered light backscattered from clouds. Clearly these types of experimental data and those obtained by extending measurements to even shorter pulses and circularly polarized beams are fertile grounds for the application of the formalism presented in this paper.

APPENDIX: CLEBSCH-GORDAN COEFFICIENTS AND *d*-FUNCTION

For the convenience of the reader, we list the formula of angular momentum we used in this paper.

The following formula for Clebsch-Goldan coefficients $\langle l-h,1,m,-j|l,m-j\rangle$ are useful for our calculation,

$$\langle l-h,1,m,-j|l,m-j\rangle = \begin{Bmatrix} \left[\dfrac{(l-m)(l-m+1)}{2l(2l-1)}\right]^{1/2} & \left[\dfrac{(l+m)(l-m+1)}{2l(l+1)}\right]^{1/2} & \left[\dfrac{(l+m)(l+m+1)}{(2l+2)(2l+3)}\right]^{1/2} \\[12pt] \left[\dfrac{(l-m)(l+m)}{l(2l-1)}\right]^{1/2} & \dfrac{m}{[l(l+1)]^{1/2}} & -\left[\dfrac{(l+m+1)(l-m+1)}{(l+1)(2l+3)}\right]^{1/2} \\[12pt] \left[\dfrac{(l+m)(l+m+1)}{2l(2l-1)}\right]^{1/2} & -\left[\dfrac{(l-m)(l+m+1)}{2l(l+1)}\right]^{1/2} & \left[\dfrac{(l-m)(l-m+1)}{(2l+2)(2l+3)}\right]^{1/2} \end{Bmatrix}, \quad (30)$$

where the row index (from above) $j = 1, 0, -1$ and the column index (from left) $h = 1, 0, -1$.

For obtaining $d_{mn}^l(x)$, the following recurrence relation is used:

$$d_{mn}^l(x) = \frac{1}{(l-1)[(l^2-m^2)(l^2-n^2)]^{1/2}}$$
$$\times \{(2l-1)[l(l-1)x - mn]d_{mn}^{l-1}(x)$$
$$- l\{[(l-1)^2 - m^2][(l-1)^2 - n^2]\}^{1/2}d_{mn}^{l-2}(x)\},$$
$$(31)$$

for $l > \max(|m|, |n|)$, with

$$d_{mn}^{\max(|m|,|n|)}(x) = \frac{1}{2^{\max(|m|,|n|)}}\left[\frac{[2\max(|m|,|n|)]!}{(|m-n|)!(|m+n|)!}\right]^{1/2}$$
$$\times (1-x)^{|m-n|/2}(1+x)^{|m+n|/2}, \quad (32)$$

and $d_{mn}^l(x) = 0$ for $l < \max(|m|, |n|)$. For $m=0$, $n=0$ we have $d_{00}^0(x) = 1$, $d_{00}^1(x) = x$, and

$$ld_{00}^l(x) = (2l-1)xd_{00}^{l-1}(x) - (l-1)d_{00}^{l-2}(x). \quad (33)$$

[1] A. Ishimaru, *Wave Propagation and Scattering in Random Media* (Institute of Electrical and Electronic Engineers, New York, 1997).
[2] R. L. T. Cheung and A. Ishimaru, Appl. Opt. **21**, 3792 (1982).
[3] Q. Ma, A. Ishimaru, and Y. Kuga, Radio Sci. **25**, 419 (1990).
[4] A. Ishimaru, S. Jaruwatanadilok, and Y. Kuga, Appl. Opt. **40**, 5495 (2001).
[5] A. D. Kim and M. Moscoso, Phys. Rev. E **64**, 026612 (2001); SIAM J. Comput. **23**, 2075 (2002).
[6] A. D. Kim and M. Moscoso, Opt. Lett. **27**, 1589 (2002).
[7] R. Vaillon, B. T. Wong, and M. P. Mengüc, J. Quant. Spectrosc. Radiat. Transf. **84**, 383 (2004).
[8] Y. Jiang, Y. L. Yung, S. P. Sander, and L. D. Travis, J. Quant. Spectrosc. Radiat. Transf. **84**, 169 (2004).
[9] M. Sakami and A. Dogariu, J. Opt. Soc. Am. A **23**, 664 (2006).
[10] A. A. Kokhanovsky, *Light Scattering Media Optics: Problems and Solutions*, 3rd ed. (Springer and Praxis Publishing, Chichester, 2004).
[11] D. Bicout, C. Brosseau, A. S. Martinez, and J. M. Scdhmitt, Phys. Rev. E **49**, 1767 (1994).
[12] R. Carminati, R. Elaloufi, and J. J. Greffet, Phys. Rev. Lett. **92**, 213903 (2004).
[13] A. H. Hielscher, J. R. Mourant, and I. Bigio, Appl. Opt. **36**, 125 (1997).
[14] S. G. Demos and R. R. Alfano, Appl. Opt. **36**, 150 (1997).
[15] V. Backman, R. Gurjar, K. Badizadegan, I. Itzkan, R. R. Dasari, L. T. Perelman, and M. S. Feld, IEEE J. Sel. Top. Quantum Electron. **5**, 1019 (1999).
[16] W. S. Bickel, J. F. Davidson, D. R. Huffman, and R. Kilkson, Proc. Natl. Acad. Sci. U.S.A. **73**, 486 (1976).
[17] W. S. Bickel and M. E. Stafford, J. Biol. Phys. **9**, 53 (1981).
[18] B. G. deGrooth, L. W. M. M. Terstappen, G. J. Puppels, and J. Greve, Cytometry **8**, 539 (1987).
[19] B. V. Bronk, W. P. van de Merwe, and M. Stanley, Cytometry **13**, 155 (1992).
[20] D. M. Winker, W. H. Hunt, and C. A. Hostetler, *Proceedings of Laser Radar Techniques for Atmospheric Sensing*, edited by U. N. Singh [Proceedings of SPIE **5575**, 8 (2004)].
[21] S. R. Pal and A. I. Carswell, Appl. Opt. **24**, 3464 (1985).
[22] G. W. Kattawar and M. J. Rakovic, Appl. Opt. **38**, 6431 (1999).
[23] X. Ni and R. R. Alfano, Opt. Lett. **29**, 2773 (2004).
[24] G. D. Lewis, D. L. Jordan, and P. J. Roberts, Appl. Opt. **38**, 3937 (1999).
[25] F. C. MacKintosh, J. X. Zhu, D. J. Pine, and D. A. Weitz, Phys. Rev. B **40**, 9342 (1989).
[26] F. C. MacKintosh and S. John, Phys. Rev. B **40**, 2383 (1989).
[27] M. Xu and R. R. Alfano, Phys. Rev. Lett. **95**, 213901 (2005); Phys. Rev. E **72**, 065601 (2005).
[28] W. Cai, M. Lax, and R. R. Alfano, Phys. Rev. E **61**, 3871 (2000).
[29] W. Cai, M. Lax, and R. R. Alfano, J. Phys. Chem. B **104**, 3996 (2000).
[30] W. Cai, M. Xu, and R. R. Alfano, Phys. Rev. E **71**, 041202 (2005).
[31] W. Cai, M. Lax, and R. R. Alfano, Phys. Rev. E **63**, 016606 (2000).
[32] M. Born and E. Wolf, *Principles of Optics*, 7th ed. (Cambridge University Press, Cambridge, England, 2002).

[33] S. Chandrasekhar, *Radiative Transfer* (Clarendon, Oxford, 1950).

[34] I. Kuščer and M. Ribarič, Opt. Acta **6**, 42 (1959).

[35] J. W. Hovenier and C. V. M. van der Mee, Astron. Astrophys. **128**, 1 (1983).

[36] B. M. Brink and G. M. Satchler, *Angular Momentum* (Clarendon Press, Oxford, 1962).

[37] M. I. Mishchenko, L. D. Travis, and A. A. Lacis, *Scattering, Absorption, and Emission of Light by Small Particles* (Cambridge University Press, Cambridge, 2002).

[38] R. P. Feyman, Phys. Rev. **84**, 108 (1951).

[39] M. J. Rakovic, G. W. Kattawar, M. Mehrubeoglu, B. D. Cameron, L. V. Wang, S. Rastegar, and G. L. Cote, Appl. Opt. **38**, 3399 (1999).

[40] S. Bartel and A. H. Hielscher, Appl. Opt. **39**, 1580 (2000).

[41] K. G. Phillips, M. Xu, S. K. Gayen, and R. R. Alfano, Opt. Express **13**, 7954 (2005).

[42] J. H. Ali, W. B. Wang, P. P. Ho, and R. R. Alfano, Opt. Lett. **25**, 1303 (2000).

[43] J. H. Ali, W. B. Wang, R. R. Alfano, and M. K. Kassir, Theor. Appl. Fract. Mech. **41**, 1 (2000).

[44] G. C. Salzman, S. B. Singham, R. G. Johnston, and C. F. Bohren, in *Flow Cytometry and Sorting*, 2nd ed. (Wiley-Liss, New York, 1990).

[45] S. Zeitz, A. Belmont, and Nicolini, Cell Biophys. **5**, 163 (1983).

[46] L. T. Perelman, V. Backman, M. Wallace, G. Zonois, R. Manoharan, A. Nusrat, S. Shields, M. Seiler, T. Hamano, I. Itzkan, J. van Dam, J. M. Crawford, and M. S. Feld, Phys. Rev. Lett. **80**, 627 (1998).

[47] R. R. Anderson, Arch. Dermatol. **127**, 1000 (1991).

[48] W. B. Wang, J. H. Ali, R. R. Alfano, J. H. Vitenson, and J. M. Lombardo, IEEE J. Sel. Top. Quantum Electron. **9**, 228 (2003).

[49] M. I. Skolnik, *Introduction to Radar Systems* (McGraw-Hill, New York, 1962).

[50] V. E. Zuev, A. A. Zemlyanov, Y. D. Kopytin, and A. V. Kuzikovskii, *High-Power Laser Radiation in Atmospheric Aerosols* (D. Reidel Publishing, Dordrecht, 1984).

[51] D. M. Winker, J. R. Pelon, and M. P. McCormick, *Proceedings of the Conference of Lidar Remote Sensing for Industry and Environment Monitoring III*, edited by U. N. Singh, T. Itabe, and Z. Liu [Proceedings of SPIE **4893**, 1 (2003)].

Determination of light absorption, scattering and anisotropy factor of a highly scattering medium using backscattered circularly polarized light

M. Xu[a], M. Alrubaiee[b], S. K. Gayen[b] and R. R. Alfano[b]

[a]Department of Physics, Fairfield University, Connecticut, CT 06824
[b]Institute for Ultrafast Spectroscopy and Lasers and Department of Physics,
The City College and Graduate Center of City University of New York, New York, NY 10031
Email: mxu@mail.fairfield.edu

ABSTRACT

The absorption coefficient, the scattering coefficient and the anisotropy factor of a highly scattering medium are determined using the diffuse reflectance of an obliquely incident beam of circularly polarized light. This approach determines both the anisotropy factor and the cutoff size parameter for the fractal continuous scattering medium such as biological tissue and tissue phantoms from depolarization of the backscattered light.

Keywords: absorption, scattering, anisotropy factor, backscattering, depolarization, circular polarization, tissue, turbid medium

1. INTRODUCTION

The estimation of the optical properties (absorption coefficient μ_a and scattering coefficient μ_s) and the anisotropy factor (g) of a turbid medium is an important problem in atmospheric, biomedical and hydrologic optics. Light diffuses in a highly scattering medium, whose behavior essentially depends on the reduced scattering coefficient $\mu'_s = \mu_s(1 - g)$. The diffusion of light remains almost the same when varying μ_s and g yet keeping μ'_s unchanged. This explains why μ_a and μ'_s, instead of μ_a, μ_s and g, are commonly used in optical imaging. Light absorption and scattering coefficients depend on the optical properties of constituent particles and their concentration. The g-factor measures how much forward peaked is the angular distribution of light when it is scattered once by a particle in the medium, and is independent of the concentration of the scatterers. The value of the g-factor correlates strongly with the size of the scatterer. Determination of the g-factor then provides a direct probe of the size of scatterer, which constitutes one useful fingerprint in discriminating normal and diseased tissues.[1, 2]

One way to estimate the g-factor is to use an iterative method that consists of repeatedly solving the corresponding direct radiative transfer problem by, for example, Monte Carlo simulations, with updated optical properties until the irradiance matches the measured values.[3] Explicit analytical equations have also been developed (analytic inverse radiative transfer method) for determining the optical properties in the simplest problems.[4] In both approaches, the type of the phase function of light scattering by the medium is usually assumed known and the Henyey-Greenstein phase function[5] has been commonly used.

In this paper, we report on a scheme of detecting light absorption coefficient, scattering coefficient and the g-factor simultaneously from measurement of the circularly polarized backscattered light at different positions along a line. Light is obliquely incident on the surface of the medium with an incidence angle $\sim$ 70 degree. Both co-polarized and cross-polarized backscattered light are measured. The difference of the backscattered co-polarized and cross-polarized light intensities is used to find the g-factor of the medium. Experimental demonstrations of this approach to obtain the three parameters (absorption coefficient, scattering coefficient and the g-factor) of tissue phantoms are presented.
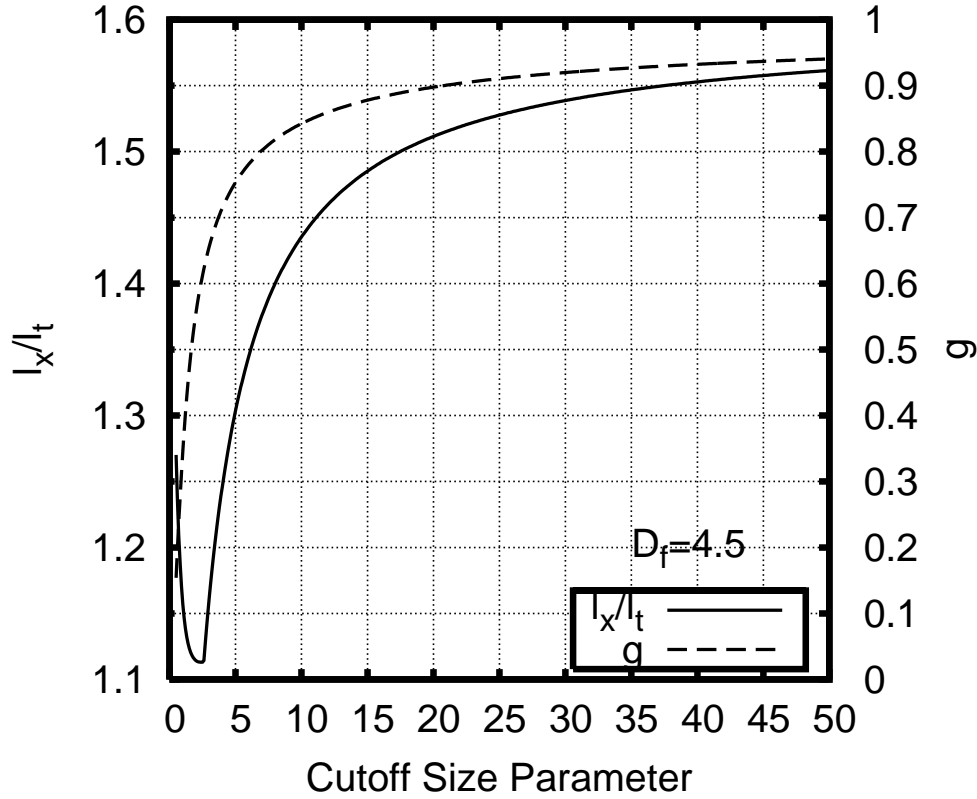
Figure 1. The ratio of the uncoiling length over the transport mean free path l_x/l_t and the anisotropy factor g of soft tissue of a fractal dimension 4.5 and of varying cutoff size parameter $X = 2\pi n l_{\max}/\lambda$.

2. THEORETICAL FORMALISM AND EXPERIMENTAL METHOD

Light propagation in a turbid medium can be described by radiative transfer theory. Diffusion approximation to radiative transfer theory is a valid model for light propagation if the medium is highly scattering and optically thick. For a polarized incident beam, light propagation in the medium accompanies its depolarization. The characteristic lengths governing light depolarization in turbid media have been obtained earlier. [6, 7] The depolarization of circularly polarized light is found to be determined by the uncoiling length l_x, the distance over which the degree of circular polarization of the beam drops by $1/e$. The uncoiling length for a turbid medium is given by [7]

$$l_x \equiv \mu_s^{-1} / \ln \frac{1}{\lambda_x} \tag{1}$$

where $\lambda_x = \max(\Lambda_0, \Lambda_1)$, $\Lambda_0 = \frac{1}{2\gamma} \int_{-1}^{1} \Re\left[S_1^* S_2\right] d\mu$, $\Lambda_1 = \frac{1}{2\gamma} \int_{-1}^{1} \Re\left[S_1^* S_2\right] \mu d\mu$, $\gamma = \frac{1}{4} \int_{-1}^{1} (|S_1|^2 + |S_2|^2) d\mu$, $\mu \equiv \cos\theta$, and $S_{1,2}(\theta)$ is the amplitude scattering function with θ the scattering angle. [8]

Light scattering by biological tissue and cells can be described by the fractal continuous random medium model. [1, 2] In this model, tissue light scattering is determined by two morphological parameters: the fractal dimension D_f and the cutoff correlation length $l_{\max}$. The parameter D_f reveals the weight of small vs large scattering centers in the sample and $l_{\max}$ measures the maximum size of scattering centers. Light depolarization characteristic lengths, including the uncoiling length l_x, in biological tissue and tissue phantoms have been investigated. [9] Fig. (1) displays the ratio l_x/l_t and the g-factor versus the cutoff size parameter $X = 2\pi n l_{\max}/\lambda$ for a fractal continuous random medium with $D_f = 4.5$ where n is the refractive index of the medium and λ is the wavelength of the incident beam in vacuum. This figure suggests that the anisotropy factor g (and $l_{\max}$) can be determined if the fractal dimension D_f and the uncoiling length l_x can be found in addition to the transport mean free path l_t.
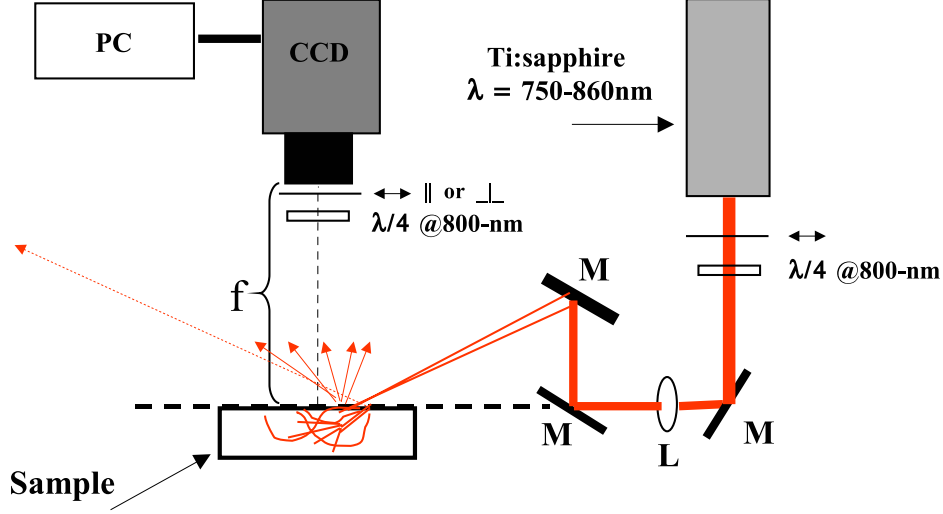
Figure 2. Schematic diagram of the experimental setup. M stands for mirror, L lens, and f is the focal length of the CCD camera. The $\lambda/4$ wave plates and polarizers are used to generate a circularly polarized beam and to detect co- or cross-polarized light at the wavelength of 800nm.

Our procedure for the determination of μ_a, μ_s and g is as follows. First μ_a and μ'_s are determined from the diffuse reflectance of the sample for an obliquely incident beam at various wavelengths centering at λ. Second, the fractal dimension D_f is determined from $\mu'_s(\lambda) \propto \lambda^{3-D_f}$. Third, the uncoiling length l_x is found from the depolarized diffuse reflectance of a circularly polarized incident beam. And finally, the anisotropy factor g is obtained by the ratio of l_x/l_t (see Fig. 1). The first two steps can be combined to retrieve μ_a, μ'_s and D_f simultaneously from fitting to the diffuse reflectance data at all wavelengths together assuming the power law for $\mu'_s(\lambda)$ is strictly satisfied.

For an obliquely incident pencil beam at the origin on the surface $z = 0$ of the sample and propagating in the direction $(\sin\alpha, 0, -\cos\alpha)$ where α is the angle of incidence, the initial ballistic motion of the beam within the medium is in the direction $(\sin\beta, 0, -\cos\beta)$ where $n\sin\beta = \sin\alpha$. The diffuse reflectance at the position $(x, y, 0)$ on the surface is given by[10]

$$R(x,y) = \frac{l_t\cos\beta}{4\pi\rho_1^3}(1 + \mu_{\text{eff}}\rho_1)\exp(-\mu_{\text{eff}}\rho_1) + \frac{l_t\cos\beta + 2z_e}{4\pi\rho_2^3}(1 + \mu_{\text{eff}}\rho_2)\exp(-\mu_{\text{eff}}\rho_2), \quad (2)$$

where $\mu_{\text{eff}} = \sqrt{3\mu_a/l_t}$, $\rho_1 = \sqrt{(x - l_t\sin\beta)^2 + y^2 + l_t^2\cos^2\beta}$, and $\rho_2 = \sqrt{(x - l_t\sin\beta)^2 + y^2 + (2z_e + l_t\cos\beta)^2}$. The parameter z_e is the extrapolation length, dependent on the refractive index mismatch at the interface.[11] Eq. (2) is used to fit the measured diffuse reflectance along a line in the x direction on the surface to obtain μ_a and l_t.

For an incident circularly polarized beam, light depolarization presents one extra channel that light leaves the co-polarized state to the cross-polarized state. Denote the co-polarized and cross-polarized backscattered light intensity for an incident circularly polarized light as $I_\pm$, respectively. The depolarized diffuse reflectance is proportional to $\Delta I = I_+ - I_-$ and can be modelled by the same expression (2) with the only modification of $\mu_a \to \mu'_a = \mu_a + l_x^{-1}$. The same technique hence can be used to fit for l_x in the region far away from the incidence point where the diffusion model is valid.

The experimental setup is shown in Fig. 2. The light source is a Ti:sapphire laser (Spectra-Physics Tsunami) tunable over the 750–860nm spectral range. The laser was operated in CW mode by turning off the acousto-optic modulator and had a spectral FWHM (full width at half maximum) bandwidth less than 1nm. The beam passes through a converging lens (focal length 40cm) and focused on the surface of the sample after elevated using a periscope mirror configuration. The incidence angle is set to be $\alpha = 72.4°$. The refractive index of the diluted Intralipid-10% suspension is $n = 1.334$ and the extrapolation length is computed to be $z_e = 1.69l_t$.[11] Backscattered light in the direction normal to the surface of the sample is recorded by a CCD camera for the wavelengths from 760nm to 860nm with a step of 10nm.
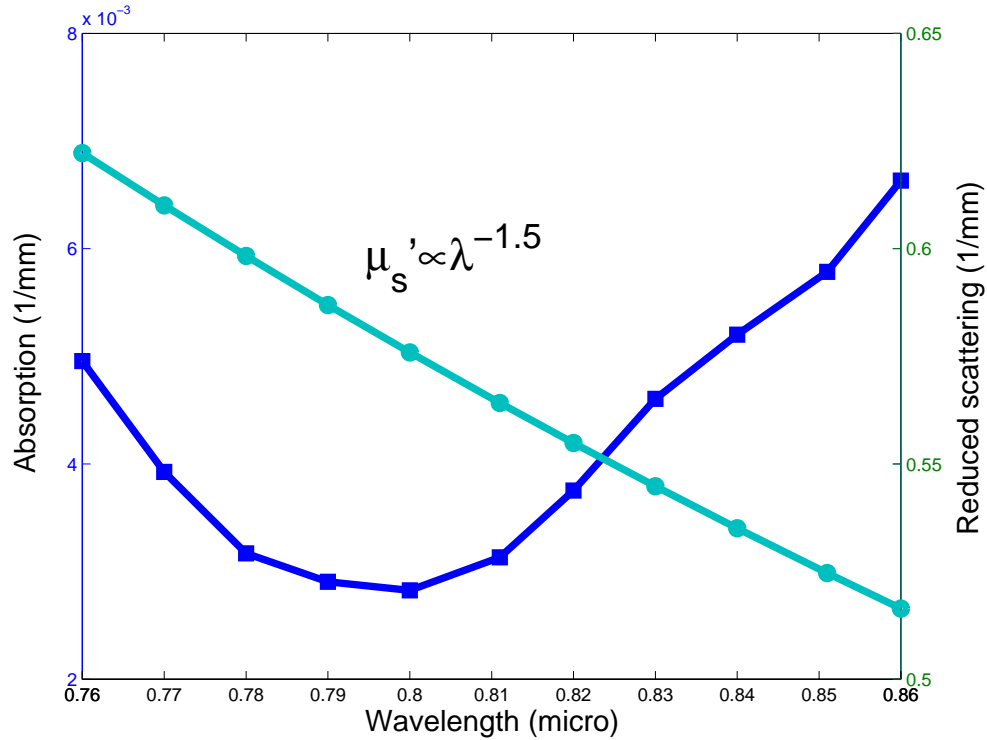
Figure 3. The wavelength dependence of the absorption and the reduced scattering coefficients of the Intralipid-10% suspension.

3. RESULT

Fig. 3 displays the wavelength dependence of μ_a and μ'_s from fitting the total diffuse reflectance where light is collected regardless of its polarization. The absorption spectrum follows essentially that of water. The wavelength dependence of the reduced scattering coefficient follows $\mu'_s \propto \lambda^{-1.5}$. The fractal dimension of the Intralipid-10% suspension is then 4.5. It should be noted this experimental value of D_f is a bit larger than the value ($D_f = 4.2$) obtained[2] from the Mie scattering computation based on the particle size distribution of the Intralipid-10% suspension measured by Staveren *et. al.*[12]

The depolarized diffuse reflectance is then measured at the wavelength of 800nm at which the absorption coefficient and the transport mean free path have been found to be $\mu_a = 0.003$mm^{-1}and $l_t = 1.77$mm, respectively, from Fig. (3). Fig. 4 displays the total backscattered light $I = I_+ + I_-$ and the depolarized backscattered light $\Delta I = I_+ - I_-$. Nearby the origin, the intensity of the cross-polarized light is stronger than that of the co-polarized light and $\Delta I < 0$. In the far zone (the region far away from the origin), the intensity of the co-polarized light is stronger than that of the cross-polarized light and $\Delta I > 0$. Fitting of the depolarized diffuse reflectance $\propto \Delta I$ along a horizontal line $3l_t$ away from the incidence point inside the far zone yields the effective absorption $\mu'_a = 0.47$mm^{-1}. The uncoiling length is then 2.13mm and the ratio $l_x/l_t = 1.20$.

From the analysis of the depolarization property of the fractal continuous medium of $D_f = 4.5$ (see Fig. 1), both the g-factor and the cut-off size parameter are now obtained. We find $g = 0.68$ at the cutoff size parameter 3.4 with $l_{\max} = 0.32\mu m$. The values of the g-factor and the cutoff size of scatterers were reported to be 0.64 at 800nm and 0.34μm in Staveren *et. al.*[12] Their agreement demonstrates the effectiveness of our proposed method.

4. DISCUSSION AND CONCLUSION

For a range of values of l_x/l_t in Fig. 1, there may be two sets of the g-factor and the cutoff size parameter giving the same ratio l_x/l_t. It does not pose any difficulty. The left branch of the l_x/l_t curve when the cutoff size parameter curve is less than 2.6 corresponds to $I_+ < I_-$ and its right branch corresponds to $I_+ > I_-$ far away from the incidence point.[7] The
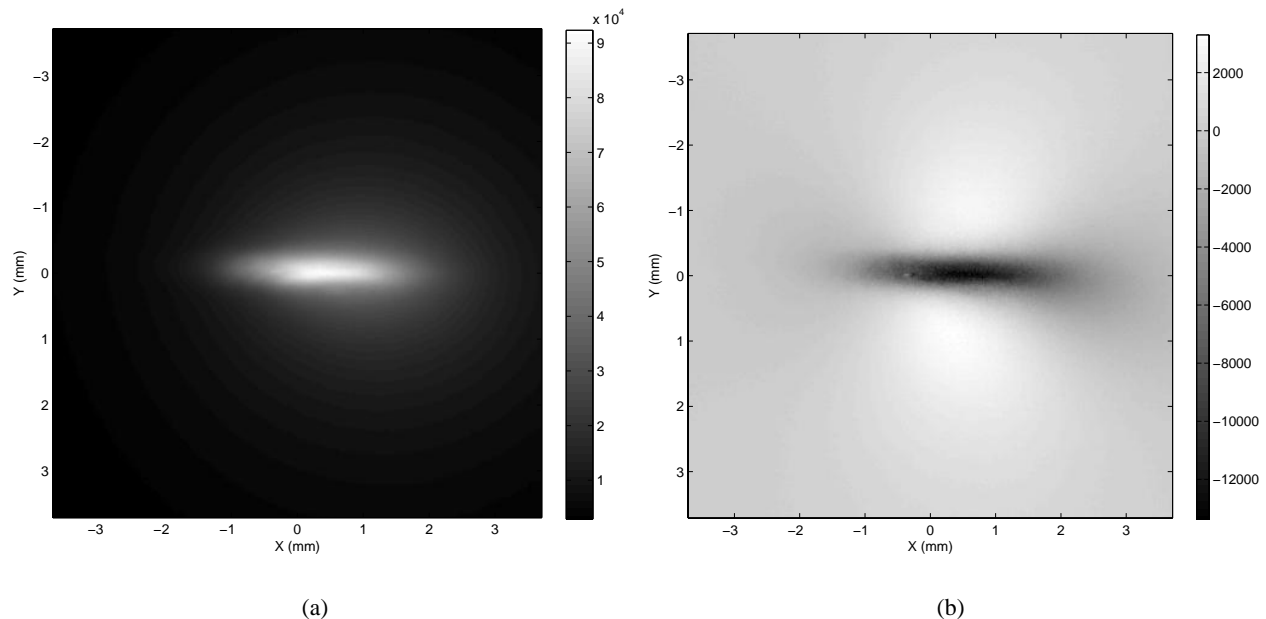
Figure 4. The intensities of backscattered light (a) the total intensity $I_+ + I_-$ and (b) the depolarized intensity $I_+ - I_-$. The circularly polarized light is incident on the origin and with an incident angle of $72.4°$. The CCD camera measures $I_\pm$ directly.

experiment shows that $I_+ > I_-$ in the far zone (see Fig. 4b) and the right branch of the l_x/l_t curve should be used in our data analysis.

The absorption coefficient, the scattering coefficient and the anisotropy factor of a highly scattering medium are determined using the diffuse reflectance of an obliquely incident circularly polarized light. This approach obtains simply both the anisotropy factor and the cutoff size parameter for the fractal continuous scattering medium from circular depolarization of the backscattered light.

REFERENCES

1. M. Xu and R. R. Alfano, "Fractal mechanisms of light scattering in biological tissue and cells," *Opt. Lett.* **30**, pp. 3051–3053, 2005.
2. M. Xu, M. Alrubaiee, and R. R. Alfano, "Fractal mechanism of light scattering for tissue optical biopsy," in *Optical Biopsy VI*, *Proceedings of SPIE* **6091**, 2006.
3. N. Joshi, C. Donner, and H. W. Jensen, "Noninvasive measurement of scattering anisotropy in turbid materials by nonnormal incident illumination," *Opt. Lett.* **31**, pp. 936–938, 2006.
4. N. J. McCormick, "Analytic inverse radiative transfer equations for atmospheric and hydrologic optics," *J. Opt. Soc. Am. A* **21**, pp. 1009–1017, June 2004.
5. L. G. Henyey and J. L. Greenstein, "Diffuse radiation in the galaxy," *Astrophys. J.* **93**, pp. 70–83, 1941.
6. M. Xu and R. R. Alfano, "Random walk of polarized light in turbid media," *Phys. Rev. Lett.* **95**, p. 213905, 2005.
7. M. Xu and R. R. Alfano, "Circular polarization memory of light," *Phys. Rev. E* **72**, p. 065601(R), 2005.
8. H. C. van de Hulst, *Light Scattering by Small Particles*, Dover, New York, 1981.
9. M. Xu and R. R. Alfano, "Light depolarization by tissue and phantoms," in *Optical Interactions with Tissue and Cells XVII*, *Proceedings of SPIE* **6084**, 2006.

10. G. Marquez and L. V. Wang, "White light oblique incidence reflectometer for measuring absorption and reduced scattering spectra of tissue-like turbid media," *Opt. Express* **1**, pp. 454–460, 1997.

11. J. X. Zhu, D. J. Pine, and D. A. Weitz, "Internal reflection of diffusive light in random media," *Phys. Rev. A* **44**, pp. 3948–3959, 1991.

12. H. J. van Staveren, C. J. M. Moes, J. van Marle, S. A. Prahl, and M. J. C. van GemertJ, "Light scattering in Intralipid-10% in the wavelength range of 400-1100nm," *Appl. Opt.* **30**(31), pp. 4507–4514, 1991.

Optical Diffuse Imaging of an *Ex Vivo* Model Cancerous Human Breast Using Independent Component Analysis

Min Xu, Mohammad Alrubaiee, S. K. Gayen, and R. R. Alfano, *Fellow, IEEE*

Abstract—Optical imaging using independent component analysis (OPTICA) has been used for detection, 3-D localization, and cross-section imaging of a tumor inside a model human breast composed of *ex vivo* human breast tissues. OPTICA uses a multisource target illumination and multidetector signal acquisition scheme to obtain multiple spatial and angular views of the sample for target localization. Independent component analysis of the perturbations in the spatial light intensity distribution measured on the sample boundary sorts out the signal originating from individual targets. A back-projection technique estimates the cross-section of each target. The approach correctly provided the positions of a tumor located at the mid-plane and two glandular structures located at different positions within the 33-mm-thick model breast. The reconstructed cross-section images are in good agreement with known dimensions of the structures, and pathological findings.

Index Terms—Breast cancer, diffuse optical imaging, independent component analysis, near infrared (NIR) imaging, optical mammography, optical imaging using independent component analysis (OPTICA).

I. INTRODUCTION

NEAR-INFRARED (NIR) diffuse optical tomography (DOT) is an emerging technology for functional characterization of biological tissues, and has been actively investigated to image lesions in human body organs, such as human breast [1]–[3], brain [4]–[7], and joints [8], [9]. A state-of-the-art DOT illuminates the sample (consisting of targets embedded in a turbid medium) with NIR light, measures the emergent light on the boundary of the turbid medium, and uses an iterative image reconstruction method for repeatedly solving the forward model of light propagation in the medium with an updated estimation of its optical properties to match the detected light intensities.

M. Xu is with the Department of Physics, Fairfield University, Connecticut, CT 06824 USA (e-mail: mxu@mail.fairfield.edu).

M. Alrubaiee is with the Department of Physics, City College and the Graduate Center, City University of New York, New York, NY 10031 USA (e-mail: malrub@sci.ccny.cuny.edu).

S. K. Gayen and R. R. Alfano are with the Institute for Ultrafast Spectroscopy and Lasers, City College and the Graduate Center, City University of New York, New York, NY 10031 USA (e-mail: gayan@sci.ccny.cuny.edu; ralfano@sci.ccny.cuny.edu).

This problem of imaging targets in a turbid medium is an ill-posed inverse problem, and *a priori* knowledge about the optical properties of the medium need to be used to obtain a unique solution at a cost of reduced resolution [10]–[13]. Various prior information such as anatomical structures obtained from X-ray or magnetic resonance imaging (MRI) and the absorption spectra of chromophores have been used to improve the imaging quality of the DOT [14]–[16]. The iterative image reconstruction is computation time intensive and reconstruction in 2-D planar sections instead of a 3-D volume is commonly practiced. Noniterative approaches have also been pursued [17]–[19]. Irrespective of these developments, reconstruction of images with adequate spatial resolution and accurate localization and characterization of the targets remain a formidable task.

We have developed an alternative approach for optical imaging using independent component analysis (OPTICA) [18], [20] that uses a multisource sample illumination and multidetector signal acquisition scheme to generate an extensive data set providing a variety of spatial and angular views of the medium. The signals from individual targets within the interrogated medium are then sorted out by using independent component analysis (ICA) based on their statistical independence. ICA is a statistical technique from information theory that is able to recover independent signals from their measured mixtures [21], [22]. ICA has been successfully applied in many biomedical applications, such as electroencephalogram (EEG) [23] and functional magnetic resonance imaging (fMRI) [24], and has been shown to be effective in separating signals from different brain activity centers. In DOT, excess light absorption or scattering by the individual targets embedded in the medium serve as the source of independent signals whose weighted mixture is recorded by a detector on the boundary of the medium. Since an independent component originating from any particular target relates directly to how light propagates from the source to the target and from the target to the detector, the recovered independent components can serve as the starting point for 3-D localization and optical characterization of individual targets in the medium. Such a staged procedure has been shown to significantly improve the sensitivity to small/weak absorptive, scattering and/or fluorescent targets, and can achieve a 3-D localization of the targets with remarkable accuracy and resolution [18], [25], [26].

The independent component is proportional to the strength of the target (the product of the difference in the absorption/scattering coefficient between the target and the background, and the volume of the target) and the convolution of the light propagators from the source to the target and from the

target to the detector. The two light propagators can be deconvoluted in the Fourier space. A 2-D cross-section image of the target is obtained by back projecting the independent component onto the transversal plane at the axial location of the target. Every independent component retrieved by ICA represents the signal from only one target with localization determined from earlier stage of analysis. So, a back projection formalism with little or no regularization can be applied to obtain a cross-section image of the target with improved spatial resolution than what is feasible in a conventional DOT.

We have previously tested the efficacy of OPTICA on samples consisting of absorbing or scattering targets within tissue phantoms and fluorescent targets in *ex vivo* tissue [18], [25], [26]. In this paper, we use OPTICA to investigate a tumor and other structures embedded in a "realistic" model breast assembled using *ex vivo* human breast tissues, as a prelude to *in vivo* breast imaging. The remainder of the paper is organized as follows. Section II presents the theoretical formalism of OPTICA and the back-projection approach for obtaining the cross-section image of a target. Section III describes the experimental arrangement, method, and parameters. Experimental results appear in Section IV. The implications are discussed in Section V.

II. THEORETICAL FORMALISM OF OPTICAL IMAGING USING INDEPENDENT COMPONENT ANALYSIS

The presence of targets (optical inhomogeneities) inside a turbid medium perturbs the spatial intensity distribution of light emergent from the medium under illumination by a probing beam. When illuminated by a point source of unit power, the change in the light intensity distribution on the boundary of the specimen due to absorptive and scattering targets can be written as [27], [28]

$$-\Delta I(\mathbf{r}_d, \mathbf{r}_s) = \int d^3\mathbf{r} \, \delta\mu_a(\mathbf{r}) \, cG(\mathbf{r}_d, \mathbf{r}) \, G(\mathbf{r}, \mathbf{r}_s)$$
$$+ \int d^3\mathbf{r} \, \delta D(\mathbf{r}) \, c\nabla_{\mathbf{r}} \, G(\mathbf{r}_d, \mathbf{r})\nabla_{\mathbf{r}} G(\mathbf{r}, \mathbf{r}_s) \quad (1)$$

in the first-order Born approximation assuming that light diffuses inside the medium [29]. Here, $\mathbf{r}_s$ and $\mathbf{r}_d$ are the positions of the source and the detector on the boundary, $\delta\mu_a(\mathbf{r}) = \mu_a(\mathbf{r}) - \mu_{a_0}$ and $\delta D(\mathbf{r}) = D(\mathbf{r}) - D_0$ are the differences in absorption coefficient and diffusion coefficient, respectively, between the target at $\mathbf{r}$ and the background medium, c is the speed of light in the medium, and $G(\mathbf{r}, \mathbf{r}')$ is the Green's function describing light propagation from $\mathbf{r}'$ to $\mathbf{r}$ inside the medium of absorption coefficient μ_{a_0} and diffusion coefficient D_0.

OPTICA assumes each inhomogeneity within the turbid medium to be a virtual source and expresses the change of the light intensity on the boundary of the specimen as

$$-\Delta I(\mathbf{r}_d, \mathbf{r}_s) = \sum_j a_j(\mathbf{r}_d) \, s_j(\mathbf{r}_s) \quad (2)$$

where $s_j(\mathbf{r}_s)$ represents the jth target illuminated by the incident wave at $\mathbf{r}_s$ and $a_j(\mathbf{r}_d)$ is the weighting matrix describing the propagation of light from the jth inhomogeneity to the detector at $\mathbf{r}_d$. Each absorptive inhomogeneity contributes one term in

(2), and each scattering inhomogeneity contributes three terms in (2) [18]. The detected change of the light intensity $-\Delta I$ is, hence, a linear mixture of signals where a_j and s_j can now be interpreted as the jth weighting matrix and virtual source, respectively. Owing to the statistical independence between these virtual sources, independent component analysis of $-\Delta I$ will yield a list of independent components and recover both a_j and s_j. Here, a_j and s_j are the independent intensity distribution on the detector and source planes, respectively, for the jth target. The number of the leading independent components gives the number of objects. The location of the jth target is obtained from the analysis of the retrieved independent component (s_j and a_j) that relates directly to the source-to-object and object-to-detector Green's functions $G(\mathbf{r}_j, \mathbf{r}_s)$ and $G(\mathbf{r}_d, \mathbf{r}_j)$ and the optical property of the target where $\mathbf{r}_j$ is the position of the jth object [18], [20], [25], [26].

For the slab geometry investigated here, there are three virtual sources of specific patterns (one centrosymmetric and two dumbbell-shaped) associated with each scattering inhomogeneity, whereas only one centrosymmetric virtual source is associated with each absorptive inhomogeneity. Among the three virtual sources associated with a scattering inhomogeneity, the centrosymmetric virtual source is the strongest and more amenable to detection in a thick turbid medium [25]. The centrosymmetric virtual source and the corresponding weighting matrix are $s_j \propto G(\mathbf{r}_j, \mathbf{r}_s)$ and $a_j \propto G(\mathbf{r}_d, \mathbf{r}_j)$, and $s_j \propto \partial G/\partial z(\mathbf{r}_j, \mathbf{r}_s)$ and $a_j \propto \partial G/\partial z(\mathbf{r}_d, \mathbf{r}_j)$, respectively, for absorptive and scattering inhomogeneities. A simple least square fitting of the centrosymmetric component, such as

$$\min_{\mathbf{r}_j, \alpha_j, \beta_j} \left\{ \sum_{\mathbf{r}_s} \left[\alpha_j^{-1} s_j(\mathbf{r}_s) - G(\mathbf{r}_j, \mathbf{r}_s) \right]^2 \right.$$
$$\left. + \sum_{\mathbf{r}_d} \left[\beta_j^{-1} a_j(\mathbf{r}_d) - G(\mathbf{r}_d, \mathbf{r}_j) \right]^2 \right\} \quad (3)$$

for the absorptive object, can be used to yield the 3-D location $\mathbf{r}_j$ and the strength $\alpha_j \beta_j$ of the target. When *a priori* knowledge about the property of the target is not available, (3) can still be used to estimate the 3-D location of the target regardless of the absorption or scattering property of the target. This is due to the fact that $\partial G/\partial z(\mathbf{r}_j, \mathbf{r}_s) \simeq -\kappa G(\mathbf{r}_j, \mathbf{r}_s)$ and $\partial G/\partial z(\mathbf{r}_d, \mathbf{r}_j) \simeq -\kappa G(\mathbf{r}_d, \mathbf{r}_j)$, where $\kappa = \sqrt{(\mu_{a_0} - i\omega/c)/D_0}$ is chosen to have a nonnegative real part with ω the modulation frequency of the incident wave.

The signal from the jth target is simply given by $-\Delta I_j = a_j(\mathbf{r}_d)s_j(\mathbf{r}_s)$. On the other hand, the centrosymmetric signal of the jth target can be approximated as a double convolution

$$-\Delta I_j(\mathbf{r}_d, \mathbf{r}_s) = \int G(\boldsymbol{\rho}_d - \boldsymbol{\rho}, z_d, z_j) \, X_j(\boldsymbol{\rho}) \, G(\boldsymbol{\rho} - \boldsymbol{\rho}_s, z_j, z_s) d\boldsymbol{\rho}$$
$$(4)$$

where the integration is over the $z = z_j$ plane, X_j represents the target, and $\boldsymbol{\rho}_d$ and $\boldsymbol{\rho}_s$ are the lateral coordinates of the detector and the source, respectively. The cross-section image of the jth target X_j is a 2-D distribution of the absorption/scattering coefficient of the target on the $z = z_j$ plane. In the Fourier space,
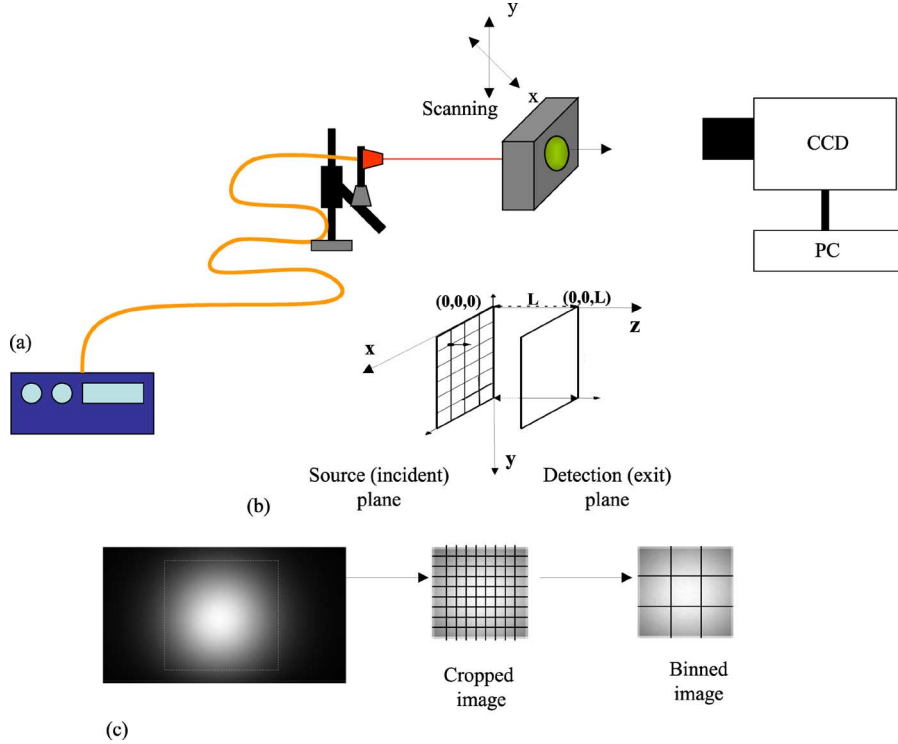
Fig. 1. (a) Schematic diagram of the experimental arrangement. CCD, charge coupled device; PC, personal computer. (b) Expanded view of the sample input (source) plane and exit (detection) plane showing the grid points in the x–y plane. (c) Typical raw CCD image of the detection plane, and how it is cropped and binned for analysis.

the target function X_j can be obtained from (4) as

$$X_j(\mathbf{q}) = -\frac{\Delta I_j(\mathbf{q} - \mathbf{q}_s, \mathbf{q}_s)}{G(\mathbf{q} - \mathbf{q}_s, z_d, z_j)G^*(\mathbf{q}_s, z_j, z_s)} \quad (5)$$

where $\mathbf{q}$ and $\mathbf{q}_s$ are the spatial frequency on the lateral plane and "$*$" denotes complex conjugate. We choose $\mathbf{q}_s = 0$ in the evaluation of the target function (5) since sources are usually much sparser than detectors in our setup where a charge-coupled device (CCD) camera is used to detect the emergent light intensity on the surface of the medium. The inverse Fourier transforms of $X_j(\mathbf{q})$ yields the high-resolution cross-section image of the jth target due to the high density of detecting pixels of the CCD. The size of the target is estimated by the full-width at half-maximum (FWHM) of the cross-section image X_j.

To sum up, OPTICA first detects and retrieves independent components corresponding to each target embedded inside a turbid medium, then obtains the 3-D location and strength of the target from these independent components, further reconstructs the cross-section image of the target on the transversal plane where the target locates, and finally, the size and the optical property of the target are estimated.

III. EXPERIMENT

The experimental arrangement for detection and localization of the tumor in the *ex vivo* model breast sample is shown in Fig. 1(a). The model breast was a 70 mm $\times$ 55 mm $\times$ 33 mm slab composed of excised female human breast tissues provided to us by National Disease Research Interchange under an Inter-

nal Review Board approval at the City College of New York. The model breast was assembled using two pieces of *ex vivo* human breast tissues. The larger piece was normal tissue that included mainly adipose tissue and streaks of fibroglandular tissues. The existence of the fibroglandular tissues was not known prior to making the measurements.

The second piece was mainly a tumor (infiltrating ductal carcinoma) with a small amount of normal tissues in the margins with an overall approximate dimension of 8 mm $\times$ 5 mm $\times$ 3 mm. An incision was made in the mid-plane (along the z-axis, which was the shorter dimension of the tissue) of the normal piece, and some amount of the normal tissue was removed from the central region making a small pouch. The tumor piece was then inserted into the pouch, and the incision was closed by moderate compression of the composite consisting of the normal tissue and the tumor along xyz-directions. The breast tissue slab was contained inside a transparent plastic box. One of the sides of the box could be moved to uniformly compress the tissue along the z-axis and hold it in position. The resulting specimen, a 70 mm $\times$ 55 mm $\times$ 33 mm slab, was treated as one entity in the subsequent imaging experiment. The position of the tumor within the slab was known since it was placed in the position as discussed earlier. One of the tests of the efficacy of this imaging approach was to see how well the known position is assessed.

A 200 μm optical fiber delivered a 784 nm, 300 mW continuous-wave beam from a diode laser for sample illumination. The beam was collimated to a 1 mm spot onto the entrance face (henceforth referred to as the "source plane")

of the slab sample. Multiple source illumination was realized in practice by step scanning the slab sample across the laser beam in an xy array of grid points using a computer-controlled translation stage. The xy array was 22×16 with a step size of 2.0 mm. The signal from the opposite face of the sample (henceforth referred to as the "detection plane") was collected by a camera lens and projected onto the sensing element of a cooled 16 b, 1024×1024 pixel CCD camera. Although the scanned area is 42 mm × 30 mm on the source plane, the imaged area of the detection plane was much larger, covering the entire 70 mm × 55 mm transverse area of the model breast. Each illuminated pixel of the CCD camera could be regarded as a detector. For illumination of every scanned point on the source plane, the CCD camera recorded the diffusely transmitted 2-D intensity pattern on the detection plane. Each image acquisition took 100 ms, and one stepping of the translational stage took 1 s. A total of 352 images were completed within 7 min. The OPTICA reconstruction and cross-section imaging is expected to be completed within 2 min once fully automated.

IV. RESULTS

A typical 2-D raw image of transmitted light intensity distribution on the detector plane for illumination at a typical scanning position is shown in Fig. 1(c). The average of all the 22×16 images was used to obtain the optical property of the slab of breast tissue. The radial profile of the intensity of the transmitted light on the average image was fitted to that predicted by a diffusion model of light propagation inside a slab. The transport mean free path was assumed to be 1 mm, the value for a typical human breast tissue at 785 nm. The reduced scattering coefficient was then 1 mm^{-1}. From the decay of the radial profile of the intensity of the transmitted light, the average absorption coefficient of the entire model breast is found to be $\mu_a = 0.0039$ mm^{-1}. Each raw image is first cropped to retain the region within the window of 50.4 mm × 51.3 mm (out of a total 70 mm × 55 mm transverse area of the model breast) over which image reconstruction would be performed. The size of 1 pixel in the raw image is 187 μm × 187 μm. The raw images are binned by merging 5×5 pixels into one to enhance the SNR, resulting in a total of 352 images of 54×55 pixels each. All the binned images corresponding to illumination of the grid points in sequence were then stacked, and used as input for independent component analysis.

The independent light intensity distributions obtained by OPTICA is displayed in Fig. 2(a). The 3-D location of the targets were obtained from least squares fitting using (3). The fittings of the independent light intensities over lines passing through the maximum value and along the horizontal direction are displayed in Fig. 2(b). The tumor C is found at 14.8 mm from the detection plane and centered at (33.3, 21.5, 18.2) mm. In addition, two glandular sites were identified. The first glandular site A is found to be located at 2.5 mm from the detection plane and centered at (11.2, 22.4, 30.5) mm; the second glandular site B is at 14.6 mm from the detection plane and centered at (21.5, 37.3, 18.4) mm. Comparison of known and 3-D positions obtained from OPTICA for the cancer site and two glandular sites is given in Table I.

The cross-section image of the tumor obtained from a 2-D inverse Fourier transform of (5) is shown in Fig. 3 (left pane). The right pane of Fig. 3 displays the intensity profiles of the cross-section image along the x- and y-directions denoted by the white dashed lines. The FWHM values of the intensity profiles yield estimates of the lateral dimensions of the tumor to be 10.3 mm × 7.4 mm, while the known dimensions are 8 mm × 5 mm. Histological micrograph of the suspect site confirmed tumor. Similar back-projection cross-sectional images and histological micrographs were obtained (not shown here) for the glandular tissues as well and their transverse sizes were estimated from OPTICA. The existence, location, and size of the glandular tissues were not known *a priori*. The glandular structure A near surface is estimated to be 2.7 and 1.6 mm in size along the x- and y-directions from the cross-section image, respectively. The size of the glandular structure B at the midplane is 8.7 and 9.2 mm in size along the x- and y-directions, respectively.

Low regularization was used in generating the cross-section images in Fig. 3 to achieve maximal spatial resolution. The artifacts in the cross-section images can be suppressed with a higher regularization at a cost of lower spatial resolution. Since the target has been localized in the earlier stage of analysis, the target will not be confused with artifacts in the cross-section images and low regularization is beneficial here.

The investigated *ex vivo* breast sample contained minimal amount of blood, and hence, the reconstructed images are for the scattering property of the sample. The change of the reduced scattering coefficient μ_s' for the targets can further be estimated from the reconstructed independent components for the sites A, B and C. The value of $\delta\mu_s'$ is given by the ratio of the strength of the target and its volume. The sites A and B have lower scattering while the site C has enhanced scattering compared to the background (mainly adipose tissue). The values of $\delta\mu_s'$ are ~0.2 and ~-0.4 mm^{-1} for the tumor and glandular tissues, respectively. Subsequent pathological analysis confirmed the site C as infiltrating ductal carcinoma, and identified the other two structures as glandular breast tissues.

V. DISCUSSION

The results of the experiments clearly demonstrate that OPTICA can locate the tumor inside the model breast with high accuracy. As can be seen from Table I, the lateral positions of the tumor agree within 0.5 mm, while the axial position agree within ~1 mm of the known values. Similar high accuracy in the respective positions of the two pieces of glandular tissues is observed as well. The accuracy of the lateral positions does not depend significantly on the depth of the targets, while that of the axial position shows a weak dependence. For the target located close to the detection plane (glandular site A at a distance of 2.5 mm from the detection plane), the axial position is determined exactly, while for targets in the midplane that are much more challenging to locate, the accuracy is within 1 mm. Given
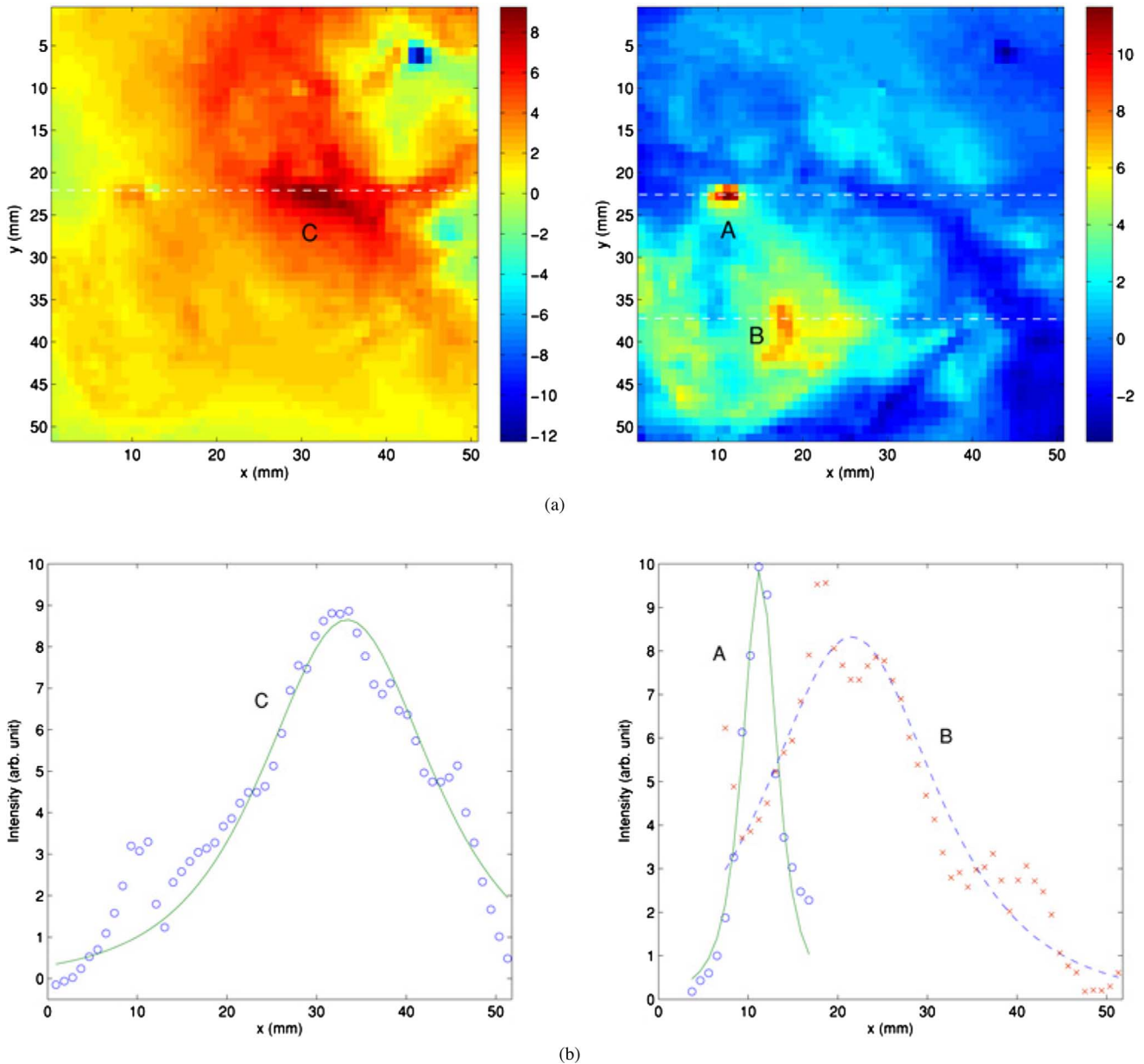
(a)

(b)

Fig. 2. (a) Independent intensity distribution on the detector plane ($z = 33$ mm) obtained by OPTICA for the tumor C (left pane) and the glandular structures A and B (right pane). (b) Corresponding bottom panes show the Green's function fits (solid lines) to the horizontal spatial profile (denoted by circles and crosses) through the center of the intensity distributions along the dashed lines.

TABLE I
COMPARISON OF KNOWN AND OPTICA ESTIMATED TARGET LOCATIONS

Target	Known Position (x, y, z) (mm)	OPTICA Estimated Position (x, y, z) (mm)
Cancer Site (C)	(33,21,16.9)	(33.3,21.5,18.2)
Glandular Site (A)	(11,22,30.5)	(11.2,22.4,30.5)
Glandular Site (B)	(21,37,17)	(21.5,37.3,18.4)

that light propagation is highly diffusive in breast tissues, this level of accuracy is quite significant.

The back-projection formalism estimates the FWHM values of the lateral dimension of the tumor to be 10.3 and 7.4 mm in size along the x- and y-directions, respectively, whereas the known dimension is 8 mm $\times$ 5 mm. This result is expected due

to diffusion of light in the tissue, and is in line with the results that we obtained in our earlier OPTICA studies [26].

Another important finding was that OPTICA predicted different scattering properties for the adipose tissue (medium), the tumor, and the glandular tissues. The glandular tissues were found to be less scattering than the adipose tissues at the wavelength of interrogation, i.e., 784 nm. The tumor was found to be more scattering. These observations are consistent with the known literature values of scattering properties of different types of tissues [30].

The nature of the inhomogeneity (either absorptive or scattering or mixed) can be discerned by OPTICA with continuous-wave measurement when the SNR is high [20], [25]. When the SNR is not favorable, the recovered independent component
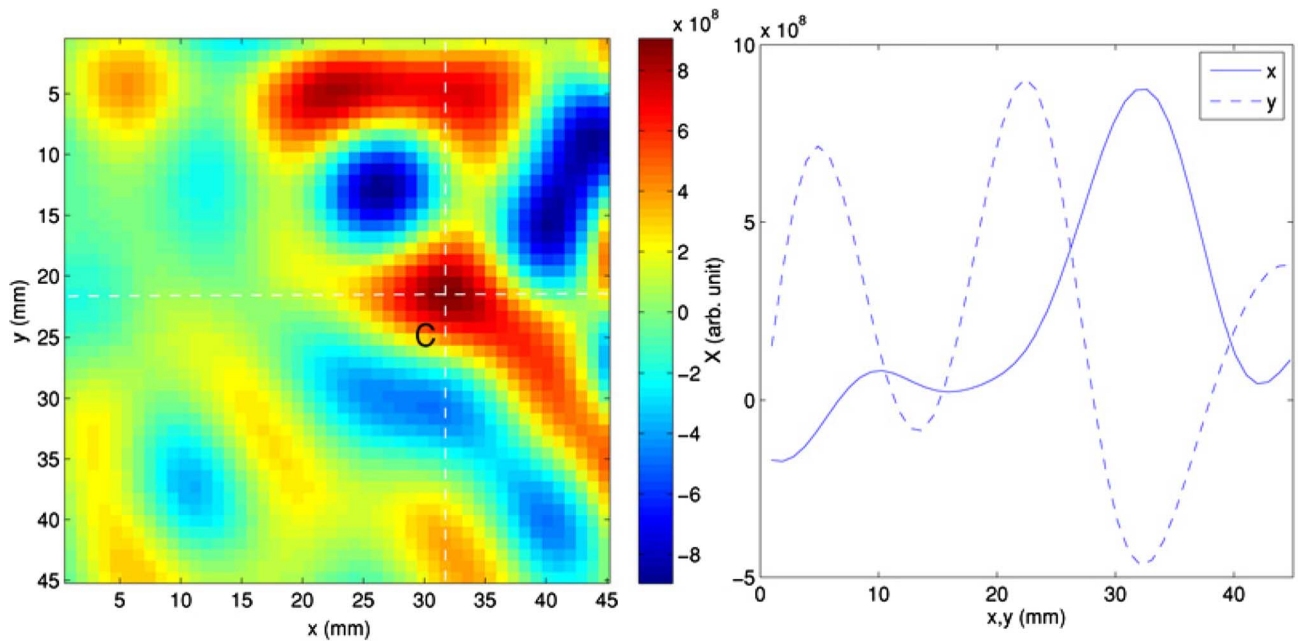
Fig. 3.   Cross-section image of the tumor at the $z = 18.2$ mm plane formed by back-projection (left pane). Right pane: Spatial profiles of the cross-section image along the x- and y-directions shown by the white dashed lines (right pane). The FWHM of the cancer site is 10.3 and 7.4 mm along the x- and y-directions, respectively.

will be due to both absorption and scattering perturbations at the site of the inhomogeneity. The strength of the target will be proportional to $\delta\mu_a + \kappa^2\delta D = \delta\mu_a + (\mu_{a_0} - i\omega/c)\delta D/D_0$, which provides a way to discriminate between absorption and scattering if measurements of multiple modulation frequencies ω are available. The capability of OPTICA for separating absorption from scattering inhomogeneities can be significantly improved with a time-domain or frequency-domain measurement. Another enabling factor will be carrying out multispectral OPTICA studies for potential diagnostic information.

OPTICA can be used for fluorescent targets as well [26]. The same experimental arrangement may be used, except for the introduction of filters to block the excitation beam and to transmit the fluorescence light. What is even more interesting is that, a beam-splitter and two detectors combination with appropriate filters may be used to simultaneously pursue absorption/scattering OPTICA and fluorescence OPTICA studies of biological samples for obtaining coregistered information from dual probes.

OPTICA is suited to detect small objects. Given its ability to identify low-contrast small objects, the approach is expected to be especially useful for the detection of breast and prostate tumors at their early stages of growth.

REFERENCES

[1] B. Chance, S. Nioka, J. Zhang, E. F. Conant, E. Hwang, S. Briest, S. G. Orel, M. D. Schnall, and B. J. Czerniecki, "Breast cancer detection based on incremental biochemical and physiological properties of breast cancers: A six-year, two-site study," *Acad. Radiol.*, vol. 12, pp. 925–933, Aug. 2005.
[2] R. Choe, A. Corlu, K. Lee, T. Durduran, S. D. Konecky, M. Grosicka-Koptyra, S. R. Arridge, B. J. Czerniecki, D. L. Fraker, A. DeMichele, B. Chance, M. A. Rosen, and A. G. Yodh, "Diffuse optical tomography of breast cancer during neoadjuvant chemotherapy: A case study with comparison to MRI," *Med. Phys.*, vol. 32, pp. 1128–1139, Apr. 2005.
[3] B. Brooksby, B. W. Pogue, S. Jiang, H. Dehghani, S. Srinivasan, C. Kogel, T. D. Tosteson, J. Weaver, S. P. Poplack, and K. D. Paulsen, "Imaging breast adipose and fibroglandular tissue molecular signatures by using hybrid MRI-guided near-infrared spectral tomography.," *Proc. Natl. Acad. Sci. USA*, vol. 103, pp. 8828–8833, Jun. 2006.
[4] J. C. Hebden, A. Gibson, T. Austin, R. M. Yusof, N. Everdell, D. T. Delpy, S. R. Arridge, J. H. Meek, and J. S. Wyatt, "Imaging changes in blood volume and oxygenation in the newborn infant brain using three-dimensional optical tomography," *Phys. Med. Biol.*, vol. 49, pp. 1117–1130, Apr. 2004.
[5] T. Durduran, G. Yu, M. G. Burnett, J. A. Detre, J. H. Greenberg, J. Wang, C. Zhou, and A. G. Yodh, "Diffuse optical measurement of blood flow, blood oxygenation, and metabolism in a human brain during sensorimotor cortex activation," *Opt. Lett.*, vol. 29, pp. 1766–1768, Aug. 2004.
[6] M. A. Franceschini, D. K. Joseph, T. J. Huppert, S. G. Diamond, and D. A. Boas, "Diffuse optical imaging of the whole head," *J. Biomed. Opt.*, vol. 11, no. 5, pp. 054007-1–054007-10, 2006.
[7] A. P. Gibson, T. Austin, N. L. Everdell, M. Schweiger, S. R. Arridge, J. H. Meek, J. S. Wyatt, D. T. Delpy, and J. C. Hebden, "Three-dimensional whole-head optical tomography of passive motor evoked responses in the neonate.," *Neuroimage*, vol. 30, pp. 521–528, Apr. 2006.
[8] Y. Xu, N. Iftimia, H. Jiang, L. L. Key, and M. B. Bolster, "Three-dimensional diffuse optical tomography of bones and joints," *J. Biomed. Opt.*, vol. 7, pp. 88–92, 2002.
[9] A. H. Hielscher, "Optical tomographic imaging of small animals," *Curr. Opin. Biotechnol.*, vol. 16, pp. 79–88, Feb. 2005.
[10] A. N. Tikhonov and A. V. Groncharsky Eds., *Ill-Posed Problems in the Natural Sciences.*   Moscow, Russia: MIR, 1987.
[11] S. R. Arridge, "Optical tomography in medical imaging," *Inverse Prob.*, vol. 15, pp. R41–R93, 1999.
[12] X. Intes and B. Chance, "Non-pet functional imaging techniques: Optical," *Radiol. Clin. North Amer.*, vol. 43, no. 1, pp. 221–234, Jan. 2005.
[13] A. P. Gibson, J. C. Hebden, and S. R. Arridge, "Recent advances in diffuse optical imaging," *Phys. Med. Biol.*, vol. 50, pp. R1–R43, Feb. 2005.

[14] V. Ntziachristos, A. G. Yodh, M. D. Schnall, and B. Chance, "MRI-guided diffuse optical spectroscopy of malignant and benign breast lesions," *Neoplasia*, vol. 4, no. 4, pp. 347–354, 2002.

[15] A. Corlu, T. Durduran, R. Choe, M. Schweiger, E. M. C. Hillman, S. R. Arridge, and A. G. Yodh, "Uniqueness and wavelength optimization in continuous-wave multispectral diffuse optical tomography," *Opt. Lett.*, vol. 28, pp. 2339–2341, Dec. 2003.

[16] S. Srinivasan, B. W. Pogue, B. Brooksby, S. Jiang, H. Dehghani, C. Kogel, W. A. Wells, S. P. Poplack, and K. D. Paulsen, "Near-infrared characterization of breast tumors in vivo using spectrally-constrained reconstruction," *Technol. Cancer Res. Treat.*, vol. 4, pp. 513–526, Oct. 2005.

[17] W. Cai, S. K. Gayen, M. Xu, M. Zevallos, M. Alrubaiee, M. Lax, and R. R. Alfano, "Optical tomographic image reconstruction from ultrafast time-sliced transmission measurements," *Appl. Opt.*, vol. 38, no. 19, pp. 4237–4246, 1999.

[18] M. Xu, M. Alrubaiee, S. K. Gayen, and R. R. Alfano, "Three-dimensional localization and optical imaging of objects in turbid media using independent component analysis," *Appl. Opt.*, vol. 44, pp. 1889–1897, 2005.

[19] Z.-M. Wang, G. Y. Panasyuk, V. A. Markel, and J. C. Schotland, "Experimental demonstration of an analytic method for image reconstruction in optical diffusion tomography with large data sets," *Opt. Lett.*, vol. 30, pp. 3338–3340, Dec. 2005.

[20] M. Xu, M. Alrubaiee, S. K. Gayen, and R. R. Alfano, "Optical imaging of turbid media using independent component analysis: Theory and simulation," *J. Biomed. Opt.*, vol. 10, pp. 051705-1–051705-12, 2005.

[21] P. Comon, "Independent component analysis—A new concept?," *Signal Process.*, vol. 36, pp. 287–314, 1994.

[22] A. J. Bell, "Information theory, independent component analysis, and applications," in *Unsupervised Adaptive Filtering*, vol. I, S. Haykin, Ed. New York: Wiley, 2000, pp. 237–264.

[23] R. Vigário, J. Särelä, V. Jousmäki, M. Hämäläinen, and E. Oja, "Independent component approach to the analysis of EEG and MEG recordings," *IEEE Trans. Biomed. Eng.*, vol. 47, no. 5, pp. 589–593, May 2000.

[24] B. B. Biswal and J. L. Ulmer, "Blind source separation of multiple signal sources of f MRI data sets using independent component analysis," *J. Comput. Assist. Tomogr.*, vol. 23, no. 2, pp. 265–271, 1999.

[25] M. Alrubaiee, M. Xu, S. K. Gayen, and R. R. Alfano, "Tomographic imaging of scattering objects in tissue-like turbid media using independent component analysis," *Appl. Phys. Lett.*, vol. 87, pp. 191112-1–191112-3, 2005.

[26] M. Alrubaiee, M. Xu, S. K. Gayen, and R. R. Alfano, "Localization and cross-section reconstruction of fluorescent targets in *ex vivo* breast tissue using independent component analysis," *Appl. Phys. Lett.*, vol. 89, pp. 133902-1–133902-3, 2006.

[27] M. A. O'Leary, D. A. Boas, B. Chance, and A. G. Yodh, "Experimental images of heterogeneous turbid media by frequency-domain diffusing-photon tomography," *Opt. Lett.*, vol. 20, pp. 426–428, 1995.

[28] M. Xu, M. Lax, and R. R. Alfano, "Time-resolved Fourier optical diffuse tomography," *J. Opt. Soc. Amer. A*, vol. 18, no. 7, pp. 1535–1542, 2001.

[29] P. M. Morse and H. Feshbach, *Methods of Theoretical Physics*, vol. I/II. New York: McGraw-Hill, 1953.

[30] M. Alrubaiee, S. K. Gayen, R. Alfano, and J. A. Koutcher, "Spectral and temporal near-infrared imaging of *ex vivo* cancerous and normal human breast tissues," *Tech. Cancer Res. Treat.*, vol. 4, pp. 457–469, 2005.

Min Xu received the B.S. and M.S. degrees from Fudan University, Shangai, China, in 1992 and 1995, respectively, and the Ph.D. degree from the City University of New York, New York, in 2001, all in physics.

He is currently an Assistant Professor in the Department of Physics, Fairfield University, Connecticut. His recent work in biomedical optics has been on modeling light scattering by cells and human tissues, and developing optical spectroscopic and tomographic methods for cancer detection. He is the author or coauthor of more than 35 peer-reviewed papers published in various international journals and also the coauthor of the book *Random Processes in Physics and Finance* (Oxford University Press, 2006). His current research interests include wave scattering and propagation in random media and coherent phenomenon, radiative transfer of polarized light, random processes and Monte Carlo methods, biomedical optics, and inverse problems in applied physics and engineering.

Mohammad Alrubaiee received the B.Sc. degree in electric engineering and the M.Sc. degree in physics from the City College, City University of New York, in 1993 and 1999, respectively, and the Ph.D. degree in physics from the Graduate Center of the City University of New York, in 2007.

He is currently a Research Associate at the Institute for Ultrafast Spectroscopy and Laser, City College, City University of New York. His current research interests include time-resolved and optical spectroscopic imaging of biomedical media and optical tomography. He is the author or coauthor of more than 12 articles published in various refereed journals.

S. K. Gayen received the B.Sc. (Hons.) and M.Sc. degrees from the University of Dacca, Dacca, Bangladesh, in 1975 and 1977, respectively, and the Ph.D. from the University of Connecticut, Storrs, in 1984.

He is currently a Professor of physics at the City College and the Graduate Center of the City University of New York, New York. His current research interests include optical biomedical imaging, imaging of targets in turbid media, tunable solid-state lasers, spectroscopy of impurity ions in solids, nonlinear optics, ultrafast laser spectroscopy, and optical spectroscopy and microscopy of nanocomposites.

Dr. Gayen is a member of the American Physical Society and the Optical Society of America.

R. R. Alfano (M'87–SM'89–F'01) received the B.S. and M.S. degrees from Fairleigh Dickinson University, Hackensack, NJ, in 1963 and 1964, respectively, and the Ph.D. degree from New York University, in 1972, all in physics.

He is currently a Distinguished Professor of science and engineering at the City College and the Graduate Center of the City University of New York, New York. He is also the Director of the Institute for Ultrafast Spectroscopy and Lasers and the DoD Center for Nanoscale Photonic Emitters and Sensors at the City College. His current research interests include optical biomedical imaging, photon propagation through turbid media, ultrafast laser science and technology, ultrafast supercontinuum generation, tunable solid-state lasers, nonlinear optics, laser-induced shock waves, terahertz spectroscopy, as well as dynamical processes in semiconductors, dielectric crystals, molecular systems, polymers, and biological systems. He is the author or coauthor of more than 650 papers published in various international journals, edited four books and several conference proceedings, and organized several major conferences. He is the holder of 101 patents.

Dr. Alfano is a Fellow of the American Physical Society, IEEE and the Optical Society of America.

Detection of a target in a highly scattering turbid medium using near-infrared center of intensity time gated imaging

Yimin Wang, S. K. Gayen, M. Alrubaiee, and R. R. Alfano

Institute for Ultrafast Spectroscopy and Lasers, Department of Physics,

The City College of New York, New York, 10031

Abstract

A near-infrared optical imaging approach for locating a target embedded in a turbid medium is introduced. The target localization is based on an analysis of the spatial variation of the transmitted light intensity distribution for illumination at different positions on the sample boundary. The approach is used to detect and generate a two-dimensional image of an absorbing target embedded inside a model scattering medium of thickness 50 times the transport mean free path of the medium, as well as, a piece of porcine liver embedded in porcine tissue.

Key words:

Optical imaging, time-resolved imaging, turbid medium, near-infrared imaging

Optical detection of a target embedded in a highly-scattering turbid medium is a challenging problem with diverse potential applications, such as, imaging of a tumor in human breast, mines in shallow coastal water, and airborne surveillance through cloud or fog cover. Light multiple scattered by the intervening medium encroaches into the region of geometrical shadow, and obscures the direct transillumination image of the target. A variety of time-resolved, frequency-domain, and continuous wave methods for direct imaging and inverse reconstruction of images has evolved over the years.[1-8] Most of these approaches are difficult to implement because those require complex experimental arrangements, sophisticated analytical schemes and time-intensive numerical algorithms for generation of images.

In this article, we introduce a transillumination imaging approach for prompt target detection. The approach is based on the premise that a target (that is, an optical inhomogeneity) within the turbid medium alters the propagation of light through the medium. Consequently, the spatial distribution of the output light intensity (SDOLI) is different with an embedded target than that without it.

The SDOLI depends on where and how the turbid medium is illuminated, as illustrated schematically in Fig. 1. In the slab geometry of Fig.1, a narrow beam of light is incident on the source plane ($z = 0$ plane). A fraction of the beam propagates diffusely in the z-direction, and emerges through the opposite side, i.e., the detection plane ($z = d$ plane). The SDOLI at the detection plane is a two-dimensional (2-D) intensity distribution that can be measured by a charge coupled device (CCD) camera. The black ellipse represents a target in the medium, and the gray spot at the detection plane is the shadow of the target. For a uniform scattering medium without the target, the intensity distribution of the diffused light inside the medium is symmetric about the incident direction, as shown by the solid curve of intensity distribution in Fig. 1. When

there is a target with optical properties different than that of the turbid medium, as shown by the black ellipse, the transmitted light intensity distribution will be altered because of scattering and/or absorption by the target. Consequently, the spatial distribution of the light intensity at the detection plane will be distorted and different with an embedded target than that without it, as shown schematically by the dashed curve. It is possible to locate the target within the turbid medium through an analysis of this intensity variation. The analysis starts with a calculation of the center of the SDOLI at the detection plane given by

$$M = \frac{\int_{x_1}^{x_2} Ixdx}{\int_{x_1}^{x_2} Idx},$$ (1)

where I is the light intensity recorded by a CCD camera and x is the position. For a uniform medium illuminated by a point source, the transmitted intensity distribution centers on the incident direction. When the target is located to the right side of the incident beam line, as shown in Fig. 1, it will introduce a shadow at the right part of the output beam and lead to a decrease and distortion in the output intensity distribution. This results in the movement of the intensity peak of the output beam to the left direction. Consequently, the center of intensity distribution M will show a left (negative) movement. When the target is to the left of the incident beam, it will introduce a shadow at the left side of the output beam and M will show a right (positive) movement. When the object is on the incident beam path, the center of intensity of the output beam profile would be same as that without target inside, but the peak intensity would be reduced.

The experimental arrangement for realizing the approach in practice is shown in Fig. 2. The scattering medium was a suspension of Intralipid-10% in water, with an estimated reduced

scattering coefficient, $\mu_s' \sim 1.168$ mm^{-1} (transport length 0.86 mm) and an absorption coefficient of 0.0021 mm^{-1} at 800 nm.[9] The Intralipid-10% suspension was held in a 240 mm x 160 mm x 65 mm rectangular glass container. A 10 mm x 10 mm x 3 mm neutral density filter (absorption coefficient 0.23 mm^{-1} at 800 nm) was placed inside the medium as the target.

The scattering medium was illuminated by 800 nm, 200 ps, 1 kHz repetition rate pulses from a Ti:sapphire laser and regenerative amplifier system. The amplified pulses were not compressed. The average beam power was 150 mW and the beam spot size was approximately 2 mm. The laser beam was incident along the z-axis into one of the 240 mm x 160 mm flat faces of the container. The 2-D intensity distribution of light emergent from the opposite end face of the cell was recorded by an ultrafast gated intensified camera system (UGICS). The UGICS provides an electronic time gate whose full width at half maximum (FWHM) duration can be set as short as 80 ps. The gate position could be varied over a 20 ns range with a minimum step size of 25 ps. The sample cell was mounted on a translation stage for lateral scanning. The input beam and the UGICS were not scanned. An 80 mm linear region of the sample was scanned in 4 mm steps providing 21 data points.

Fig. 3 (a) shows the temporal profile of the tramsmitted pulse without the target inside the medium. The 80 ps time gate was centered at a time that corresponded to the peak position of the transmitted pulse profile indicated by an arrow on the profile. Two-dimensional images were recorded at each scanning position, a typical image being shown in Fig. 3(b). Fig. 3(c) shows the horizontal intensity profiles obtained by integrating a 3-pixel wide area around the white dashed line shown in Fig. 3(b). The solid line in Fig. 3(c) is a spatial profile without the target inside the medium, while the dotted line is the corresponding profile when the target was on the incident

beam path. The solid (dashed) line in Fig. 3(d) presents the spatial profile when the target was to the right (left) of the incident beam path.

For a quantitative evaluation of this intensity distortion, the spatial intensity profiles were obtained for all 21 scanning positions, and the corresponding centers of the intensity distributions, M_i were calculated using Eq. (1). The average of the 21 profiles was then obtained, and its center of intensity was calculated and taken to be the reference, M_0. The differences, $\Delta M_i = M_i - M_0$, were obtained and plotted as a function of scanning position as shown by the squares in Fig. 4. ΔM is negative in the left side of this center-of-intensity curve (CIC), passes through a minimum, reaches zero, rises to a positive maximum and tends towards zero further out to the right. The curve has inversion symmetry about the zero position. The zero point shows the position of the embedded target. When the scanning beam is far away from the object, ΔM is close to zero. The dashed curve in Fig. 4 shows the first derivative of the center of intensity $Q=d(\Delta M)/dx$, which peaks at the target position.

These results show that as the distance between the input beam and target increases, ΔM changes quickly at first. The maximum value of Q occurs at the position when the scanning beam passes through the target. After reaching the optimal value, ΔM changes slowly towards zero. When the target is far away from the input beam, its influence is small, and the intensity distribution does not change. The FWHM of Q vs. scan position curve in Fig. 4 is approximately 12.6 mm, which is close to the real width of the target, 10mm.

The potential of this approach for optical biomedical imaging was next explored. The target was a 5 mm x 5 mm x 5 mm piece of porcine liver placed inside a 150 mm x 90 mm x 50 mm slab of porcine tissue held in a rectangular plastic cell. The center of the target was at a distance of 25 mm from both the entrance and the exit faces of the porcine tissue. A 100 mm x

60 mm inner region of the sample was scanned across the incident laser beam. The sample cell was scanned with a step size of 4 mm along the *x* direction (100 mm segment). The cell was then stepped by 3 mm along the *y* direction, and the *x*-scan was repeated. The scanning pattern continued until the entire region was scanned. Time-gated 2-D images were recorded for each scanning position. CIC curves were generated for every scan along the *x* direction, and the value of *Q* was estimated for each scanning position. Plotting of *Q* vs. scan position (*x, y*) generated a 2-*D* gray-scale pseudo-color image as shown in Fig. 5(a). The dark area with high *Q* value represents the porcine liver specimen that absorbed 800-nm light more strongly that the porcine muscle tissue. Fig. 5(b) shows a spatial profile of the image was obtained by integrating a 3-pixel wide area around the white dashed line in Fig. 5(a) The FWHM of the profile is 10 mm, which is larger than the target width of 5 mm, but comparable to the resolution that other optical imaging methods obtain.[5]

In summary, a method based on analysis of the transmitted light intensity distribution has been introduced for obtaining lateral position and 2-D images of an absorbing target in a highly scattering turbid medium including biological tissues.

References

1. J. C. Hebden, S. R. Arridge, and D. T. Delpy, "Optical imaging in medicine: I experimental techniques," Phys. Med. Biol. **42**, 825-840, (1997).

2. R. R. Alfano, X. Liang, L. Wang, and P. P. Ho, "Time resolved imaging of translucent droplets in highly scattering turbid media," Science **264**, 1913-1915 (1994).

3. L. Wang, P.P. Ho, C. Liu, G. Zhang, R. R. Alfano, "Ballistic 2-D imaging through scattering walls using an ultrafast optical kerr gate," Science **253**, 769-771, (1991).

4. O'Leary M. A., Boas, D.A., Chance, B., and Yodh, A. G. Experimental images of heterogeneous turbid media by frequency-domain diffusing-photon tomography. *Opt. Lett. 20,* 426-428 (1995).

5. Arridge, S. R.. Optical tomography in medical imaging. *Inverse Probl.* **15***,* R41–R93 (1999).

6. W. Cai, S. K. Gayen, M. Xu, M. Zevallos, M. Al., M. Lax, and R. R. Alfano, "Optical tomography image reconstruction from ultrafast time sliced transmission measurements," Appl. Opt. **38**, 4237-4246, (1999).

7. D. Grosenick, H. Wabnitz, H. H. Rinneberg, K. T. Moesta, and P.M. Schlag," Development of a time-domain optical mammography and first *in vivo* applications," Appl. Opt. **38**, 2927-2943, (1999).

8. H. Dehghani, B. W. Pogue, S. P. Poplack, and K. D. Paulsen, "Multiwavelength three-dimensional near-infrared tomography of the breast: initial simulation, phantom, and clinical results," Appl. Opt., **42**, 135-145, (2003)

9. H. J. van Staveren, C. J. M. Moes, J. van Merle, S. A. Prahl, and M. J. C. van Gemert, "Light scattering in Intralipid-10% in the wavelength range of 400-1100 nm," Appl. Opt. **30**, 4507-4514 (1991).

Figure Captions

Fig. 1. A schematic diagram of the diffuse light transmission through a turbid medium showing the target and the "shadow." The inset at the top shows intensity spatial intensity distribution without the target (solid curve) and with the target (dashed curve).

Fig. 2. A schematic diagram of the experimental arrangement (Key: PS = pulse stretcher, RGA= regenerative amplifier, UGICS = ultrafast gated intensified camera system)

Fig. 3. (a) Temporal profile of the transmitted pulse. The arrow indicates the gate position. (b) A typical time-gated image (2-D intensity distribution) of the output plane. (c) Spatial intensity profile without the target (solid line), and with the target (dotted line). (d) Similar spatial profiles as in (c), except the solid (dotted) curve corresponds to the target being located to the right (left) of the incident beam line. The arrows C, C_L, and C_R represent the peak intensity positions in the corresponding spatial profiles.

Fig. 4. Variation of the center of intensity distribution (ΔM) and its first derivative Q as a function of the scan position

Fig. 5. (a) Two-dimensional image of a 5 mm x 5 mm x 5 mm piece of porcine liver embedded inside a slab of porcine tissue; (b) horizontal spatial profile of the image.
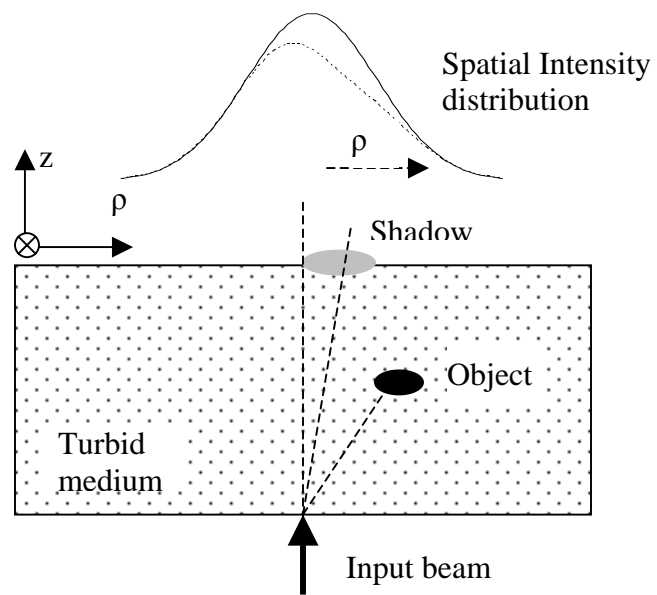
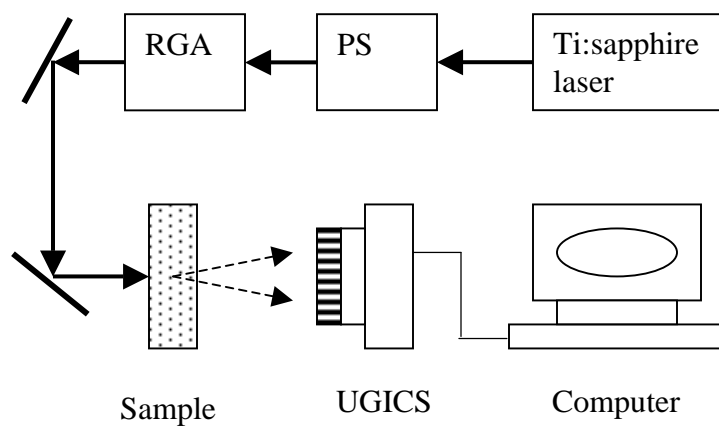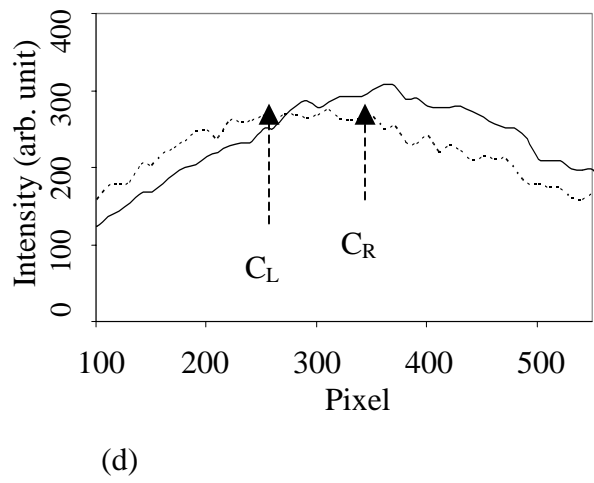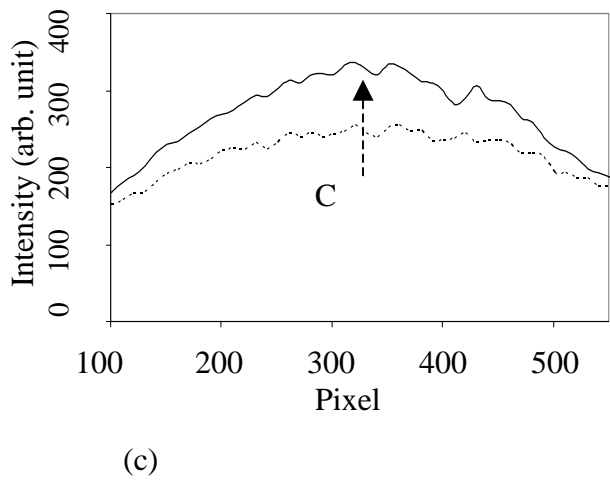Spatial Intensity distribution

ρ

z

ρ

Shadow

Object

Turbid medium

Input beam

Fig. 1

| RGA | PS | Ti:sapphire laser |

Sample   UGICS   Computer

Fig. 2

(a)

(b)

(c)

(d)

Fig. 3

Fig. 4

(a)

Porcine tissue

Porcine liver

(b)

10mm

Fig. 5